THESIS

APPLICATION OF MODEL REDUCTION TOOLS IN ANALYSIS OF WIND-

INDUCED PRESSURES ON LOW-RISE BUILDINGS

Submitted by

Chieh-hsun Wu

Department of Civil and Environmental Engineering

In partial fulfillment of the requirements

For the Degree of Master of Science

Colorado State University

Fort Collins, Colorado

Summer 2012

Master's Committee:

    Advisor: Bogusz Bienkiewicz

    Marvin E Criswell
    Hiroshi Sakurai

ABSTRACT

APPLICATION OF MODEL REDUCTION TOOLS IN ANALYSIS OF WIND-
INDUCED PRESSURES ON LOW-RISE BUILDINGS

Recent advances in laboratory and field measurement techniques and numerical simulations of wind-induced loading on buildings and structures made possible generation of large data sets, suitable for database-assisted wind-resistant design. In parallel, data reduction tools have been developed to aid storage, management and accessibility issues associated with large datasets/databases. In the presented research, application of such tools in analysis of stationary and non-stationary wind-induced pressures on a generic low-rise building is discussed. Both stationary and non-stationary cases are addressed.

In stationary analyses, Proper Orthogonal Decomposition (POD) and Method of Snapshot (SPOD) were used to identify the most energetic spatio-temporal structures of the pressures. Linear Stochastic Estimation (LSE) and Gappy POD (GPOD) were employed to generate the pressures at specified target locations via extrapolation of the pressures provided at chosen reference locations. Optimized reference positions were determined using algorithm-based and empirical approaches. In non-stationary analyses, Wavelet De-noising and Two-Stage-Moving-Averaging were applied to decompose the non-stationary pressure into time-varying mean, standard deviation and normalized fluctuation. The techniques developed for stationary pressures were adapted for non-stationary cases.

In analysis of the stationary data, the extrapolation techniques (GPOD and LSE) were found to reduce the data more efficiently than the modal reduction tools (POD and SPOD). In pressure extrapolation, LSE provided more accurate pressure predictions than GPOD. A hybrid approach combining the use of GPOD, with algorithm-based reference positions selection, and LSE extrapolation enabled the most efficient capturing of the primary and secondary spatio-temporal features of the pressure. This technique is recommended for analyses focused on development of reduced models of wind pressures induced on low-rise buildings.

In the non-stationary investigations, the hybrid GPOD-LSE technique, developed in analysis of the stationary pressures and modified for the non-stationary cases, led to accurate pressure predictions and model reductions. This methodology appears to be a suitable tool for similar analyses of non-stationary wind-induced pressures on low-rise buildings.

Follow-up investigations of stationary and non-stationary cases are recommended to assess potential for further optimization of the developed techniques and their application in analyses of wind-induced loading on other buildings and structures.

ACKNOWLEDGEMENTS

TABLE OF CONTENTS

LIST OF TABLES

LIST OF FIGURES

LIST OF SYMBOLS

Symbols

$a(t,n)$ n^{th} modal principal coordinate at time t

$[B]$ A matrix that stores the LSE i^{th} reference tap contribution constant for j^{th} target field in $B(i,j)$

$[B_0]$ A matrix saves LSE bias constants in a single-row matrix with element $B_0(j)$ representing j^{th} target field bias constant

$C_p(t,x)$ Pressure coefficients at location x and time t

$\overline{C_p}(x)$ Mean pressure coefficient at location x

$C'_p(t,x)$ Fluctuation pressure coefficient

f Gappy POD f matrix

$\varphi(t,n)$ SPOD temporal eigenvector, as function of time t and mode n

$\Phi(n,x)$ POD/SPOD basis eigenvector, as function of location x and mode n

$\kappa(M)$ Condition number of matrix M

λ_n n^{th} modal eigenvalue of POD spatial/SPOD temporal covariance matrix

$\mu_p(t,x)$ Time-varying mean at location x and time t

M Gappy POD M matrix

$R^s(x_i, x_j)$ Entry (x_i, x_j) in spatial covariance matrix R^s

$R^t(t_i, t_j)$ Entry (t_i, t_j) in temporal covariance matrix R^t

x_{ref} Reference tap location

$\sigma_p(t,x)$ Time-varying standard deviation at location x and time t

$z_p(t,x)$ Normalized fluctuation at location x and time t

Abbreviations

POD	Proper Orthogonal Decomposition
GPOD	Proper Orthogonal Decomposition on Gappy data
LSE	Linear Stochastic Estimation
SPOD	Snapshot Proper Orthogonal Decomposition

Operators

$\overline{C_p(x,t), C_p(x',t)}$	Covariance of $C_p(x,t)$ and $C_p(x',t)$ over total time duration $\boldsymbol{T}$
$(n,:)$	All entries of row n
$\widehat{\Box}$	Reconstructed/extrapolated data

Chapter 1   Introduction

As the technology of building surface pressure measurement improves, interest in database-assisted design (DAD) of structures under wind effect has been growing. The detailed pressure measurement data usually requires large computer memory and advanced database management. These disadvantages had been addressed in the past, and efforts have been expended to reduce the size of generated data. In wind engineering, some model reduction techniques have been employed in analysis of turbulent wind and wind-induced loadings on buildings and other structures.

Most of the wind engineering investigations of wind loading on buildings and structures are based on the model experiments conducted in wind tunnel laboratories. In typical settings, pressure time series measured on surfaces of building models are stationary, which means that the statistical parameters of the data do not vary over time. Most of the tools for data reduction have been developed for such (stationary) cases. However, buildings in the real world are not always exposed to stationary environments and a question arises about the applicability of the stationary tools for non-stationary situations, such as wind field and wind loading associated with wind downbursts or passage of gust fronts.

In this thesis, both stationary and non-stationary pressure time series are analyzed. For stationary cases, Proper Orthogonal Decomposition (POD), Method of Snapshot (SPOD), Gappy POD (GPOD) and Linear Stochastic Estimation (LSE) have been

selected as analysis tools. Overall, the involved reduction schemes use statistical relationships derived from high resolution pressure records, in search of the maximum reduction in the data sets, while still preserving the data fidelity at a level suitable for reliable practical analyses.

POD and SPOD belong to modal reduction category, as they are applied to decompose a given data set into several modal components, and the original system can be reduced and represented by the sum of a few dominant modes. Though it requires storing of principal coordinates, which are event and time dependent, such reductions have been shown in the literature to be reliable. LSE and GPOD belong to extrapolation tools, which generate the instantaneous target quantities – wind-induced pressures in the present case – by extrapolating the instantaneous quantities defined over reference fields. The statistical parameters required to be stored by extrapolation tools are time independent and the fidelity of the reduced models depends on the analyzed systems.

To reach efficient data reduction, extrapolation tools are typically employed. The fidelity of a reduced model was found to be dependent on the reference locations used in such extrapolations. Locations undergoing high energetic pressures, identified by using either POD or SPOD, were proposed for reference tap placements. However, there are questions regarding the best way to extrapolate pressures in applications employing the mentioned above techniques (POD, SPOD, GPOD and LSE). One of the goals of the current research was to compare the pros and cons of these techniques, and to establish an optimal approach for extrapolation of wind pressures induced on building surfaces.

Wavelet De-noising and Two-Stage-Moving-Averaging were applied to deal with non-stationary problems. Each decomposed non-stationary element – time-varying

mean, time-varying standard deviation and normalized fluctuation – were treated as stationary. The extrapolation methods developed for stationary problems were adapted to accommodate the non-stationary aspects. The reduced models were compared with their counterparts obtained using stationary assumptions to evaluate the effectiveness of the proposed non-stationary pressure extrapolations.

The thesis is organized as follows. The motivation and a brief overview of the presented research has been presented in Chapter 1. In Chapter 2, the review of background information on the employed techniques is provided. Chapter 3 discusses the analyses carried out in this research and the results. The conclusions drawn from the described research and recommendations for future investigations are presented in Chapter 4. Detailed mathematical derivations referred to in the main body of this thesis are presented in Appendix.

Chapter 2   Theoretical Background

2.1   Introduction

In this chapter, the theoretical background on the model reduction methods selected for the research described in this thesis is presented. The discussed methods are divided into two categories: (I) Methods for stationary cases; and (II) Methods for non-stationary cases. Category I includes: Proper Orthogonal Decomposition (POD), Method of Snapshot (SPOD), Gappy POD (GPOD) and Linear Stochastic Estimation (LSE). The first three methods can be classified as POD related. The LSE and GPOD are data extrapolating tools which can be used to calculate instantaneous quantities at specified (target) positions, using values defined at other (reference) positions. There is a relation between LSE and POD modal contents. As is shown in Chapter 3, reconstruction of POD results (e.g. principal coordinates) by applying LSE and Gappy POD allows for assessment of the accuracy of the two methods.

Methods suitable for analyses of non-stationary data - Category II methods – considered in this thesis include: Wavelet De-noising Technique (WDT); and Two-Stage Moving Averaging (TSMA). The analysis procedures proposed for non-stationary pressure extrapolations are described.

2.2 Proper Orthogonal Decomposition (POD)

The main objective of the Proper Orthogonal Decomposition (POD) technique is to establish a deterministic eigenvector function $\Phi(x)$ which is best correlated with all the elements of the ensemble of a random field (Bienkiewicz et al. (1993)). Given a random wind-induced pressure coefficient $C_p(t,x)$, the pressure fluctuation coefficient $C_p'(t,x)$ is calculated as follows:

$$C_p'(t,x) = C_p(t,x) - \bar{C}_p(x) \qquad \text{2.2-1}$$

where $\bar{C}_p(x)$ is the mean pressure coefficient at location x, averaged over time duration T. The maximum of the projection of $C_p'(t,x)$ on $\Phi(x)$ is sought. An integral form of this operation is as follows:

$$\int C_p'(t,x)\Phi(x)dx = \max \qquad \text{2.2-2}$$

Enforcement of this condition, in the mean-square sense, leads to an eigenvalue problem:

$$\left[R^s\right]\{\Phi\} = \lambda\{\Phi\} \qquad \text{2.2-3}$$

where $[R^s]$ is the zero-time-lag spatial covariance matrix,

$$R^s(x_i,x_j) = \frac{1}{T}\sum_{t=1}^{T} C_p'(t,x_i)C_p'(t,x_j) \qquad \text{2.2-4}$$

$\{\Phi\}$ is the eigenvector and λ is the eigenvalue. Typically the eigenvectors are normalized as follows:

$$\sqrt{\sum_x \Phi^2(n,x)} = 1 \qquad \text{2.2-5}$$

They are used as the POD basis functions in a series expansion of the pressure

$$C_p'(t,x) = \sum_n a(t,n)\Phi(n,x) \qquad \text{2.2-6}$$

where the principal coordinates are

$$a(t,n) = \frac{\sum\limits_{x} C'_p(t,x)\Phi(n,x)}{\sum\limits_{x} \Phi^2(n,x)}$$

2.2-7

It can be shown that the principal coordinates are independent

$$\frac{1}{T}\sum_{t=1}^{T} a(t,n)a(t,m) = \lambda_n \delta_{mn}$$

2.2-8

where δ_{mn} is Kronecker operator. The eigenvalue, λ_n, indicates energy of the system represented by the nth basis modal eigenvector (Sirovich (1987)). The ratio of ith mode cumulative energy to the total energy, E_i, can be calculated as follows:

$$E_i = \frac{\sum\limits_{n=1}^{i} \lambda_n}{\sum\limits_{n} \lambda_n}$$

2.2-9

2.3   Method of Snapshots (SPOD)

Method of Snapshots (SPOD) was introduced by Sirovich (1987) as a way to determine POD modes for larger spatial problems. In this section, only a brief description of the mathematical formulation of this method is given. The concept of this method is similar to that of the POD analysis except that SPOD starts with the temporal covariance of the random pressure field. First, the temporal "snapshots" of pressure $C_p(x,t)$ are recorded with uniform time step τ. The pressure mean and fluctuation are determined:

$$\overline{C}_p(x) = \frac{1}{T}\sum_{t=1}^{T} C_p(t,x)$$

2.3-1

$$C'_p(t,x) = C_p(t,x) - \overline{C}_p(x)$$

2.3-2

where T denotes the total number of snapshots, and $t = 1, 2, ..., T$ is a snapshot counter. The time step τ needs to be greater than the overall correlation time (Sirovich (1987)). The temporal covariance of the snapshots is:

$$R^t(i,j) = \frac{1}{T}\sum_{x=1}^{X} C_p^{'}(t_i, x)C_p^{'}(t_j, x)$$
2.3-3

where x denotes each tap location, X denotes total number of locations. $[R^t]$ is a temporal covariance matrix of dimension $(T \times T)$. The eigenvalues λ_n and the temporal eigenvectors $\varphi(t, n)$ are then calculated. The eigenvalues are exactly the same as those obtained from the spatial covariance matrix obtained using POD. Thus the energy content of each mode calculated from SPOD and POD is the same. The (POD-based) spatial eigenvectors are next calculated as the linear combinations of the temporal eigenvectors and the pressure snapshots:

$$\Phi(n,x) = \sum_{t=1}^{T} \varphi(t,n)C_p^{'}(t,x)$$
2.3-4

Finally the SPOD principal coordinates are obtained by substituting the calculated spatial eigenvectors $\Phi(n,x)$ in Eq. 2.2-7. It should be noted that the length of the spatial eigenvectors obtained from SPOD method is proportional to the relative energy content associated with a particular mode:

$$\frac{\sqrt{\sum_x \Phi^2(i,x)}}{\sum_n \sqrt{\sum_x \Phi^2(n,x)}} = \frac{\lambda_i}{\sum_n \lambda_n}$$
2.3-5

In contrast, the length of the eigenvectors calculated during POD is of unit length, see Eq. 2.2-5. The temporal covariance matrix involved in the SPOD analysis is usually of large size. Thus, solution of the eigenvalue problem associated with this matrix is computer-

time intense. In such cases, data analysis based on the POD technique is more convenient. Both the SPOD and POD have the ability to provide insights regarding the physical phenomena associated with the analyzed datasets, in our case – the wind induced external building pressures. The obtained eigenvalues and eigenvectors indicate, respectively, the overall and local spatial levels of contribution of each mode to the fluctuation levels of the analyzed dataset of the building pressures.

2.4   Gappy POD (GPOD)

2.4.1   Description of GPOD

Gappy POD (GPOD) is described in detail by Willcox (2006). A brief overview of this method is presented in this section. GPOD can be classified as an extrapolation tool which can be used to predict the instantaneous random field (wind-induced pressure in the present case) at target (desired) locations using instantaneous values acquired at reference (specified) locations. The statistical relationship between the values at target and reference locations is used in this extrapolation.

Assume that the POD-based spatial eigenvectors (determined either indirectly from SPOD or directly from POD) have been already obtained from analysis of the full dataset – wind-induced pressures at all pressure tap locations. If the pressure data acquired at some tap locations are discarded, the resulting data set is incomplete and the data (set/system) is denoted as "Gappy". Hereafter, the locations at which the data have been discarded are labeled as the target locations and the remaining locations (with the retained data) are called the reference locations. The main step in GPOD is the retrieval of the instantaneous POD/SPOD principal coordinates via the "Gappy" spatial eigenvectors and instantaneous pressures. The extrapolated instantaneous pressures on

target locations are subsequently obtained as the linear function of known basis eigenvector Φ and the reconstructed principal coordinates $\hat{a}$.

The formulation of GPOD to retrieve principal coordinates is presented in detail in Section A1 of the Appendix. The instantaneous pressure fluctuation at each of the reference taps $C_p'(t, x_{\text{ref}})$ can be approximated by using the POD reconstruction involving the POD (spatial) eigenvectors and principal coordinates (Eq. 2.2-6). By taking derivatives of squared error (discrepancy) between the original pressure and its approximation with respect to each modal principal coordinate on all reference locations and an instant t, the following result is obtained:

$$[M]\{\hat{a}\} = \{f\} \qquad\qquad 2.4\text{-}1$$

where

$$M(i, j) = \Phi(i, :_{\text{ref}})\Phi^{\text{T}}(j, :_{\text{ref}}) = \sum_{x_{\text{ref}}=1}^{X_{\text{ref}}}\Phi(i, x_{\text{ref}})\Phi(j, x_{\text{ref}}) \qquad\qquad 2.4\text{-}2$$

$$f(i) = \Phi(i, :_{\text{ref}})C_p'^{\text{T}}(t, :_{\text{ref}}) \qquad\qquad 2.4\text{-}3$$

$$\hat{a}(i) = \hat{a}(t, n = i) = \text{ optimized principal coordinate } i. \qquad\qquad 2.4\text{-}4$$

where $\Phi(i, :_{\text{ref}})\Phi^{\text{T}}(j, :_{\text{ref}})$ in Eq. 2.4-2 denotes the inner products of "Gappy" eigenvectors. The $\Phi(i, :_{\text{ref}})C_p'^{\text{T}}(t, :_{\text{ref}})$ in Eq. 2.4-3 denote the inner products of Gappy eigenvectors and Gappy pressure fluctuation evaluated at time t . Note that the problem domain in solving Eq. 2.4-1 is confined to time t and the reference spaces. $[M]$ is a function of locations, while $\{f\}$ is a function of both locations and time. The optimized principal coordinates $\{\hat{a}\}$ can be used in Eq. 2.2-6 to reconstruct the pressure at target locations:

$$\hat{C}_p(t, x_{t\arg et}) = \sum_n \hat{a}(t, n)\Phi(n, x_{t\arg et}) + \overline{C}_p(x_{t\arg et}) \qquad\qquad 2.4\text{-}5$$

Thus the extrapolation of the Gappy data set is completed. There is a limit in the Gappy reconstruction method. The total number of modal principal coordinates that are calculated cannot exceed the total number of the reference taps.

In GPOD, locations appropriate for the placement of reference taps were discussed by Willcox (2006). The accuracy of the reconstructed principal coordinates is found to be greatly affected by the orthogonality of the matrix $[M]$. If all tap locations are used, $[M]$ is the identity matrix and the principal coordinates can be reconstructed accurately. If only some reference taps are used, the Gappy inner products of eigenvectors form non-zero values in the off-diagonal entries of $[M]$ and the orthogonality is lost. Therefore, the principal coordinates cannot be reconstructed accurately in the Gappy situation. Overall, the reference locations should be selected so that the orthogonality is preserved in $[M]$ to the possible extent (i.e. the diagonal entries in $[M]$ are relatively large and off-diagonal entries in $[M]$ are relatively small).

To achieve the above goals, the condition number of $[M]$ needs to be minimized. The condition number of the square matrix $[M]$ is defined as the multiplication of the matrix norm of $[M]$ and the matrix norm of inversion of $[M]$.

$$\kappa(M) = \|M\|\|M^{-1}\|$$
$$\text{2.4-6}$$

where the matrix norm $\|M\|$ is the square root of largest eigenvalue of $[M][M^{-1}]$:

$$\|M\| = \sqrt{\lambda_{\max}(MM^{-1})}$$
$$\text{2.4-7}$$

A discussion of the condition number is described in the mathematics text (Kreyszig (1999)). An algorithm for selection of the reference taps is discussed next.

2.4.2 Algorithm for Reference Tap Selection

The algorithm proposed by Willcox (2006) for reference tap selection is as follows:

I. Selection of the first reference tap location: Consider the first N modes that capture a significant level of the system's energy, say 95%. Loop over all possible placement locations x and update the reference tap layout $:_{\text{ref}}^{(1)} = [x]$. Next, evaluate $\left[M_x^{(1)} \right]$ for all the possible locations:

$$M_x^{(1)}(i,j) = \Phi(i,:_{\text{ref}}^{(1)})\Phi^{\text{T}}(j,:_{\text{ref}}^{(1)}) \qquad i,j = 1,2,...,N \qquad \text{2.4-8}$$

Choose the first reference tap location r1 that maximizes the "modal variation", which is the summation of diagonal entries minus the summation of off-diagonal entries of $\left[M_x^{(1)} \right]$.

II. Selection of second reference tap location: With the first tap location set, loop over all possible remaining placement locations x $(x \neq \text{r1})$. For each location, update the reference tap layout $:_{\text{ref}}^{(2)} = [\text{r1} \ x]$, evaluate $\left[M_x^{(2)} \right]$:

$$M_x^{(2)}(i,j) = \Phi(i,:_{\text{ref}}^{(2)})\Phi^{\text{T}}(j,:_{\text{ref}}^{(2)}) \qquad i,j = 1,2 \qquad \text{2.4-9}$$

Evaluate the condition number of $\left[M_x^{(2)} \right]$ by using Eq. 2.4-6 and choose the second reference tap location r2 that minimizes $\kappa\left(M_x^{(2)} \right)$.

III. Repeat step II for all the remaining tap locations: With the defined $n-1$ taps, loop over all possible remaining placement locations x $(x \neq \text{r1}, \text{r2}, ..., \text{r}n-1)$. For   each   location,   update   the   reference   tap   layout

$: _{\text{ref}}^{(n)} = [\text{r1} \quad \text{r2} \quad ... \quad \text{r}n-1 \quad x]$, add the leading eigenvector $\Phi(n, :_{\text{ref}}^{(n)})$ and calculate $\left[M_x^{(n)} \right]$:

$$M^{(n)}_x(i,j) = \Phi(i, :_{\text{ref}}^{(n)})\Phi^{\text{T}}(j, :_{\text{ref}}^{(n)}) \qquad i,j = 1,2,...,n \qquad \text{2.4-10}$$

Evaluate the condition number of $\left[M_x^{(n)} \right]$ by using Eq. 2.4-6 and choose the nth reference tap location $\text{r}n$ that minimizes $\kappa\left(M_x^{(n)} \right)$.

2.5 Linear Stochastic Estimation (LSE)

2.5.1 LSE Method

The detailed derivation of LSE is reviewed by Chen et al. (2003). Only brief use of this technique is described in this section. LSE is based on the assumption that a random field can be considered as a linear combination of some other random variables which are known and correlated. Applying this to a surface pressure field, the pressure time series at a target tap location $\hat{C}_p(t, x_{\text{target}})$ can be estimated using pressure time series at other (denoted reference) tap locations, $C_p(t, x_{\text{ref}})$:

$$\hat{C}_p(t, x_{\text{target}}) = \sum_{x_{\text{ref}}=1}^{X_{\text{ref}}} b_{x_{\text{ref}}}(x_{\text{target}})C_p(t, x_{\text{ref}}) + b_0(x_{\text{target}}) \qquad \text{2.5-1}$$

The key step in LSE is the determination of the coefficients b's. By taking derivative of the mean square residual error (between the approximation and the original pressure) with respect to $b_{x_{\text{ref}}}(x_{\text{target}})$ and bias $b_0(x_{\text{target}})$, the equations for b's, involving spatial covariance of the random pressure are formulated.

In this thesis, the formulation is extended to more than one target and reference locations. The following equation governing the reference contribution constants is obtained:

$$[B] = [R^s]^{-1}[R_0^s]$$

2.5-2

where $[B]$ is a matrix that stores the ith reference tap contribution constant for j^{th} target field in $B(i,j)$, $[R^s]$ is the spatial covariance matrix with elements $R^s(i,j)$ representing covariance between pressure fluctuations at i^{th} and j^{th} reference spaces. $[R_0^s]$ is the spatial covariance matrix with elements $R_0^s(i,j)$ representing covariance between i^{th} reference space and j^{th} target field. For a case with total numbers X_{ref} and X_{target} of the reference and target locations, Eq. 2.5-2 is explicitly expressed below:

$$
\begin{bmatrix}
B(1_{ref}1_{target}) & B(1_{ref}2_{target}) & \cdots & B(1_{ref}X_{target}) \\
\vdots & B(i_{ref}j_{target}) & \ddots & \vdots \\
B(X_{ref}1_{target}) & & & B(X_{ref}X_{target})
\end{bmatrix} =
$$

$$
\begin{bmatrix}
\overline{\dot{C}_p(1_{ref})\dot{C}_p(1_{ref})} & \cdots & \overline{\dot{C}_p(1_{ref})\dot{C}_p(X_{ref})} \\
& \overline{\dot{C}_p(i_{ref})\dot{C}_p(j_{ref})} & \vdots \\
sym & & \overline{\dot{C}_p(X_{ref})\dot{C}_p(X_{ref})}
\end{bmatrix}^{-1}
\begin{bmatrix}
\overline{\dot{C}_p(1_{ref})\dot{C}_p(1_{target})} & \overline{\dot{C}_p(1_{ref})\dot{C}_p(2_{target})} & \cdots & \overline{\dot{C}_p(1_{ref})\dot{C}_p(X_{target})} \\
\vdots & \overline{\dot{C}_p(i_{ref})\dot{C}_p(j_{target})} & \ddots & \vdots \\
\overline{\dot{C}_p(X_{ref})\dot{C}_p(1_{target})} & & & \overline{\dot{C}_p(X_{ref})\dot{C}_p(X_{target})}
\end{bmatrix}
$$

2.5-3

After $[B]$ is computed, the target bias constants are obtained as follows:

$$[B_0] = \overline{C}_p(:_{t\,arg\,et}) - \overline{C}_p(:_{ref})[B]$$

2.5-4

where $[B_0]$ consists of elements $B_0(j)$ representing j^{th} target field bias constant. Finally the extrapolation equation for the target pressure field (2.5-1), for time t is computed:

$$\hat{C}_p(t, :_{\text{target}}) = C_p'(t, :_{\text{ref}})[B] + [B_0]$$ 2.5-5

where $\hat{C}_p(t, :_{\text{target}})$ denotes the instantaneous pressure at time t for j^{th} target location.

LSE has been proven to be a convenient statistical extrapolation tool, when used in basic research and engineering applications. It has been pointed out [10] that in implementations of this method, the reference fields should be selected with caution due to the fact that the mean square error of the linear estimate of $C_p(t, x_{\text{target}})$ is large when $C_p(t, x_{\text{target}})$ is uncorrelated with $C_p(t, x_{\text{ref}})$, e.g. when there is a large separation between x_{target} and x_{ref}.

2.5.2 Relation between LSE and POD

Consider pressure time series $C_p(t, x_1)$ and $C_p(t, x_2)$ at two locations x_1 and x_2. POD analysis had been applied to decompose these data into two modal contents:

$$\begin{bmatrix} C_p(t, x_1) \\ C_p(t, x_2) \end{bmatrix} = \begin{bmatrix} \Phi(n_1, x_1) & \Phi(n_2, x_1) \\ \Phi(n_1, x_2) & \Phi(n_2, x_2) \end{bmatrix} \begin{bmatrix} a(t, n_1) \\ a(t, n_2) \end{bmatrix} + \begin{bmatrix} \overline{C}_p(x_1) \\ \overline{C}_p(x_1) \end{bmatrix}$$

After subtracting the mean C_p from both sides, the above equations can be inverted to obtain the POD modal principal coordinates as linear functions of the instantaneous pressure. Therefore LSE technique can be applied to retrieve POD principal coordinates (Cohen et al. (2006)):

$$\hat{a}(t, n) = \sum_{x_{\text{ref}}=1}^{X_{\text{ref}}} d_{x_{\text{ref}}}(n) C_p(t, x_{\text{ref}}) + d_0(n)$$ 2.5-6

Eq. 2.5-6 is actually in the form of Eq. 2.5-1 with different target quantities $\hat{a}(t, n)$ and different linear constants d's.

The above reconstruction will be compared later with that using GPOD (Eq. 2.4-1). It should be noted that the better reconstructed $\hat{a}(t,n)$ can be anticipated if the reference pressures $C_p(t,x_{\text{ref}})$ are more correlated with modal principal coordinates $\hat{a}(t,n)$. The local maxima and minima of spatial eigenvectors indicate not only higher energy distribution but also higher correlation between pressures and principal coordinates. A heuristic approach proposed by Cohen et al. (2006) suggests that the reference taps should be placed at locations of the peaks of the spatial eigenvectors. Note that in Eq. 2.5-6 the total number of principal coordinates being reconstructed is not limited to the total number of reference taps. By combining all the reconstructed principal coordinates $\hat{a}(t,n)$ and the known basis eigenvectors $\Phi(n,x)$, the rounded pressure extrapolation (combination of Eq. 2.5-6 and 2.4-5) is equal to the direct pressure extrapolation (Eq. 2.5-1).

2.6 Tools for Analysis of Non-Stationary Wind-induced Pressures

2.6.1 Introduction

Applications of the techniques described in the previous section are limited to stationary data sets. However, non-stationary situations are what the real world provides. In such cases, the statistical properties vary with time. In analysis of wind loading, the time series of the wind pressure coefficients can be normalized using the time-varying mean and standard deviation:

$$z_p(t,x) = \frac{\left(C_p(t,x) - \mu_p(t,x)\right)}{\sigma_p(t,x)} \qquad \text{2.6-1}$$

where $\mu_p(t,x)$, $\sigma_p(t,x)$ and $z_p(t,x)$ respectively denote time-varying mean, standard deviation and the normalized fluctuation of the pressure coefficient.

In the following subsection, methods for obtaining the time-varying mean and standard deviation are presented. Once these non-stationary quantities are obtained, SPOD is applied to aid identification of the physical phenomena and schemes for reference locations selection.

2.6.2   Wavelet De-noising & Two Stage Moving Averaging

The non-stationary decomposition techniques discussed by Chen and Letchford (2005) are reviewed herein. Time-varying mean is obtained by applying Wavelet Shrinkage (Donoho et al. (1995)). The following standard nonparametric regression model involving an unknown regression function $\mu_p(t)$ is used (Donoho et al. (1995)):

$$C_p(t) = \mu_p(t) + \varepsilon(t) \qquad t = 1,...,T \qquad\qquad 2.6\text{-}2$$

where $C_p(t)$ is the observed non-stationary data, $\varepsilon(t)$ is an identically independently distributed (i.i.d.) Gaussian white noise and t denotes the time instant. The main objective is to find the unknown function $\mu_p(t)$ based on the noise-contaminated observation $C_p(t)$. To accomplish this task, a nonlinear wavelet method, termed wavelet shrinkage or thresholding (Chen and Letchford (2005), Donoho et al. (1995)), is employed. It consists of the following three steps: Decomposition, Determination of Threshold Detail Coefficients and Reconstruction (Chen and Letchford (2005), Misiti et al. (1996)).

Implementation of the wavelet shrinkage procedure requires selection of a type of wavelet and a wavelet decomposition level J. The Daubechies' wavelets of the 2 to 10 orders were found to be good choices (Chen and Letchford (2005)). The decomposition level J corresponds to the maximal window width 2^j. Selection of proper J is crucial.

The idea of one-level simple discrete wavelet decomposition (Misiti et al. (1996)) is illustrated in Figure 1. Wavelet transform technique filters the original non-stationary time series into its low-frequency and high-frequency components via low-pass and high pass filters, respectively. Similarly, a multilevel wavelet transform can be employed in the signal decomposition, as is illustrated in Figure 2. The signal de-noising is visualized in Figure 3. The Wavelet Tool Box (Misiti et al. (1996)) in MATLAB developed by The MathWorks Inc. and a MATLAB function proposed by Chen and Letchford (2005) was employed to implement de-noising using the wavelet shrinkage approach (see Section A2. in Appendix).

After the time-varying means are determined, the zero-mean non-stationary fluctuations are obtained by subtracting the time-varying mean from the original time-varying pressure. A two-stage-moving-averaging described by Nau et al. (1982) is employed on the zero-mean non-stationary fluctuations to calculate the time-varying standard deviations of the pressure. For the averaging, this method first sets a time window which is consistent with wavelet de-noising window width 2^j. Effectively, a weighting function (e.g. a half cosine wave) is applied before the variance of the zero-mean non-stationary fluctuation in the specified window centered on an instant t is calculated. The window is moved over the length of the time series of the zero-mean non-stationary fluctuation and the variance envelope is obtained. It has been addressed

by Nau et al. (1982) that the computed envelope is overly smooth and locally biased. In order to overcome this drawback, a method for "correcting" the single-stage weighted moving average has been proposed by multiplying the instantaneous variance by an instantaneous correcting factor. This factor is obtained by applying a moving averaging techinique on the ratio of the squared zero-mean non-stationary fluctuation and the instantaneous variance.

2.6.3   Modified Algorithm for Non-stationary Reference Tap Selection

The reference pressure taps are selected for the non-stationary data in a way similar to that used for stationary cases discussed earlier in this thesis. The SPOD eigenvectors $(\Phi^\mu,\ \Phi^\sigma, \text{and } \Phi^z)$ of each non-stationary element ($\mu_p(t,x)$, $\sigma_p(t,x)$ and $z_p(t,x)$) were utilized to find the reference taps. By treating each non-stationary element as an independent stationary event, the layout of reference taps can be defined. However, each non-stationary element may yield different layouts of reference taps (i.e. rμn $\neq$ rσn $\neq$ rzn). So modifications of tap selection algorithm described in Section 2.4.2 are sought to yield a reference tap layout optimized for the three non-stationary elements.

The first tap r1 is selected by considering the largest sum of modal variations of three non-stationary elements. However, eigenvectors of each non-stationary element may not be of the same level of magnitude and the direct sum of modal variations will be dominated by elements with larger eigenvector magnitude. In order to ensure each non-stationary element is equally weighted, the eigenvectors of each non-stationary element $(\Phi^\mu,\ \Phi^\sigma, \text{and } \Phi^z)$ are normalized by the length of its first mode. The steps involved in this procedure are listed below:

I. Normalize the eigenvectors of each non-stationary element by the length of its first mode.

II. For a candidate location x, utilize the normalized eigenvectors to evaluate the matrices $\left[M_x^{\mu(1)}\right]$, $\left[M_x^{\sigma(1)}\right]$ and $\left[M_x^{z(1)}\right]$. Calculate the modal variation of each non-stationary element and sum of the three modal variations.

III. Select the first reference tap $r1$ that corresponds to the largest sum.

For the selection of the remaining taps, a similar strategy to find a optimized location is to look at the smallest sum of condition numbers of each non-stationary element. However, the condition number reflects the global (modal) and local (energy) distribution (Eq. 2.3-5), and direct summation of condition numbers would be dominated by elements with lower system complexity. The taps identified during this selection could correspond to unimportant modes of lower complexity elements (e.g. time-vary mean and time-varying standard deviation). To overcome this limitation, a threshold mode numbers n_{th}^{μ} and n_{th}^{σ} for the time-varying mean and time-varying standard deviation, respectively, are defined based on the related level of cumulative energy, say 90%. When choosing the optimized tap rn, the condition number of time-varying mean was calculated from $\left[M_x^{\mu(n)}\right]$ of locked dimension $(n_{\text{th}}^{\mu} \times n_{\text{th}}^{\mu})$, with the total number of taps n exceeding the threshold mode number n_{th}^{μ}. The same scenario is applied for the time-varying standard deviation. The resulting modified algorithm for selecting rest reference taps is summarized below:

I. For choosing rn, where $n = 2, 3, \ldots$: Define the threshold mode number n_{th}^{μ} and n_{th}^{σ} that are associated with a level of cumulative energy, say 90%, for time-varying mean and time-varying standard deviation, respectively.

II. Set a candidate location x for rn in reference tap layout $:_{\text{ref}}^{(n)} = [\text{r1} \quad \text{r2} \quad ... \quad \text{r}n-1 \quad x]$.

III. Utilize the Gappy eigenvectors to form $\left[M_x^{\mu(n)}\right]$, $\left[M_x^{\sigma(n)}\right]$ and $\left[M_x^{z(n)}\right]$:

$$M_x^{\mu(n)}(i^\mu, j^\mu) = \Phi^\mu(i^\mu, :_{\text{ref}}^{(n)})\Phi^{\mu\text{T}}(i^\mu, :_{\text{ref}}^{(n)}) \qquad \text{2.6-3}$$

where $i^\mu, j^\mu = 1,2, ..., n$ if $(n \le n_{\text{th}}^\mu)$, or $i^\mu, j^\mu = 1,2, ..., n_{\text{th}}^\mu$ if $(n > n_{\text{th}}^\mu)$.

$$M_x^{\sigma(n)}(i^\sigma, j^\sigma) = \Phi^\sigma(i^\sigma, :_{\text{ref}}^{(n)})\Phi^{\sigma\text{T}}(i^\sigma, :_{\text{ref}}^{(n)}) \qquad \text{2.6-4}$$

where $i^\sigma, j^\sigma = 1,2, ..., n$ if $(n \le n_{\text{th}}^\sigma)$, or $i^\sigma, j^\sigma = 1,2, ..., n_{th}^\mu$ if $(n > n_{\text{th}}^\sigma)$.

$$M_x^{z(n)}(i^z, j^z) = \Phi^z(i^z, :_{\text{ref}}^{(n)})\Phi^{z\text{T}}(i^z, :_{\text{ref}}^{(n)}) \qquad \text{2.6-5}$$

where $i^z, j^z = 1,2, ..., n$ for all n.

IV. For a trial layout $:_{\text{ref}}^{(n)}$, calculate the summation of condition numbers:

$$\kappa\left(M_x^{(n)}\right) = \kappa\left(M_x^{\mu(n)}\right) + \kappa\left(M_x^{\sigma(n)}\right) + \kappa\left(M_x^{z(n)}\right) \qquad \text{2.6-6}$$

V. Loop over possible x and choose rn so that the $\kappa\left(M_x^{(n)}\right)$ in Eq. 2.6-6 is minimized. Return to Step II and proceed with the subsequent steps of the next reference tap selection.

2.6.4 Non-stationary Pressure Extrapolation

Once the reference taps are defined, extrapolation tools can be applied for data reduction. LSE method is applied in extrapolation since it leads to more accurate predictions (based on observations presented later in Section 3.4.2). By treating each non-stationary element as a stationary pressure time series, the linear coefficients $([B]^\mu, [B_0]^\mu, [B]^\sigma, [B_0]^\sigma, [B]^z, [B_0]^z)$ are first evaluated. Only the reference taps are retained in the pressure extrapolation phase. With the new non-stationary

pressures $C_p(t, x_{\text{ref}})$ measured at those reference taps, the non-stationary elements ($\mu_p(t, x_{\text{ref}}), \sigma_p(t, x_{\text{ref}})$ and $z_p(t, x_{\text{ref}})$) are decomposed and their target counterparts are extrapolated by using techniques discussed in Section 2.5.1:

$$\hat{\mu}_p(t, x_{\text{target}}) = \sum_{x_{\mathit{ref}}=\text{r}1}^{\text{rN}} b_{\text{ref}}^{\mu}(x_{\text{ref}})\mu_p(t, x_{\text{ref}}) + b_{\text{target}}^{\mu} \qquad \text{2.6-7}$$

$$\hat{\sigma}_p(t, x_{\text{target}}) = \sum_{x_{\mathit{ref}}=\text{r}1}^{\text{rN}} b_{\text{ref}}^{\sigma}(x_{\text{ref}})\sigma_p(t, x_{\text{ref}}) + b_{\text{target}}^{\sigma} \qquad \text{2.6-8}$$

$$\hat{z}_p(t, x_{\text{target}}) = \sum_{x_{\mathit{ref}}=\text{r}1}^{\text{rN}} b_{\text{ref}}^{z}(x_{\text{ref}})z_p(t, x_{\text{ref}}) + b_{\text{target}}^{z} \qquad \text{2.6-9}$$

Finally the non-stationary pressures $\hat{C}_p(t, x_{\text{target}})$ at target locations are determined:

$$\hat{C}_p(t, x_{\text{target}}) = \hat{z}_p(t, x_{\text{target}})\hat{\sigma}_p(t, x_{\text{target}}) + \hat{\mu}_p(t, x_{\text{target}}) \qquad \text{2.6-10}$$

The procedures discussed in Sections 2.6.1 through 2.6.4 and employed for the non-stationary extrapolation are summarized as two steps which are schematically shown in Figures 4 and 5. In the first step (Figure 4), the non-stationary pressures measured at all tap locations are decomposed into three non-stationary elements (Section 2.6.2). Each non-stationary element is treated as a stationary event and SPOD (Section 2.3), GPOD reference tap selection (Section 2.6.3) and LSE (Section 2.5.1) are applied. The linear coefficients ($[B]^{\mu}, [B_0]^{\mu}, [B]^{\sigma}, [B_0]^{\sigma}, [B]^{z}, [B_0]^{z}$) of three non-stationary elements are first evaluated and saved. On the second step (Figure 5), the new non-stationary pressures measured at those reference taps $C_p(t, x_{\text{ref}})$ are decomposed into three non-stationary elements ($\mu_p(t, x_{\text{ref}})$, $\sigma_p(t, x_{\text{ref}})$ and $z_p(t, x_{\text{ref}})$). The corresponding target quantities ($\hat{\mu}_p(t, x_{\text{target}})$, $\hat{\sigma}_p(t, x_{\text{target}})$ and $\hat{z}_p(t, x_{\text{target}})$) are extrapolated by using LSE with parameters obtained in the first step. Finally the non-stationary pressures

21

$\hat{C}_p(t, x_{\text{target}})$ at target locations are determined by combining the extrapolated three non-stationary elements.

Chapter 3   Experimental Setup, Data Analysis and Discussion

3.1   Chapter Overview

First, the experimental setup used to generate the wind pressure data is described. Next, implementation of the data analysis techniques discussed in Chapter 2 is illustrated. During the first phase of the data analysis, stationary cases were analyzed first. Subsequently, non-stationary wind pressure data were processed.

3.2   Experimental Setup

A generic low-rise industrial building with prototype planar dimensions of 200 ft. × 100 ft. and a building height of 40 ft. was selected. The wind-induced pressures on the external surface of the building were obtained during wind tunnel testing at the Wind Engineering and Fluids Laboratory (WEFL) at Colorado State University (CSU) as described by Endo (2011). The testing was performed at a geometrical scale of 1:150, using a building model furnished with 990 pressure taps. The geometry of the model and the tap locations are schematically shown in Figure 6.   It can be seen that the taps are uniformly distributed over the building surfaces.   As a result, approximately equal tributary areas are associated with each tap. Such a tap layout simplifies spatio-temporal analysis of the time series of the acquired pressures. The overall view of the building model installed in the wind tunnel test section is shown in Figure 7.

The structural frames of the building employed in analysis presented in this thesis are schematically displayed in Figure 8, where they are labeled as 1st row frame and 15th row frame. The pressure tap locations and numbering employed for these frames are indicated in Figure 9. Wind pressures induced at these locations (for the two frames) were employed in analysis. The wind directions considered were 0, 45 and 90 degrees, see Figure 8. The pressure time series were nearly simultaneously measured at all the 990 taps using the Electronically Scanned 1024-channel Pressure Measurement System developed at WEFL. The pressures were acquired at a sampling rate of 332 samples per second (332 Hz). Approximately 87-second long data records (29,000 data points per channel) were acquired. Pressure measurement system and the related instrumentation employed in the wind tunnel testing are described in detail by Endo (2011).

3.3 Data Analysis using POD and SPOD

In this section, the application of POD (introduced in Section 2.2) and snapshot POD (SPOD) (outlined in Section 2.3) is described. Time series of the wind pressures induced by 90° wind on the 15th row frame are considered. The eigenvalues, basis eigenvectors and principal coordinates obtained from POD and SPOD are compared. The effects of snapshot time ($\tau = 4$ and $\tau = 40$) on POD and SPOD eigenvalues and basis eigenvectors are investigated.

The eigenvalue problem implied by POD and SPOD is considered first. Both the methods result in the same modal eigenvalues λ_i. These values and the relative cumulative energy E_i are shown in Figure 10. It can be seen that the effects of the snapshot time τ are negligible. The eigenvalues and the cumulative energy information

can be used to assess the complexity of the analyzed system: the lower the number of the first modes that are needed to capture most of the system's energy, say 90%, the simpler the system is. It can be seen in Figure 10 that the first 8 modes contain 90% of the data set energy, while the first 11 and 18 modes contain respectively 95% and 99% of the energy.

All 27 modal basis eigenvectors Φ obtained from POD and SPOD (for snapshot time $\tau = 4$) are shown in Figure 11. As mentioned in Section 2.3, the POD basis eigenvectors are typically normalized so that the length of each of the vector is unity. On the other hand, the length of each modal SPOD basis eigenvector is proportional to relative energy (Eq. 2.3-5). Figure 12 shows the standard deviation of principal coordinates obtained using POD (left vertical axis) and SPOD (right vertical axis). As can be seen, the POD values decrease with the increasing mode index, while the SPOD values are mode independent. Moreover, the standard deviations of the SPOD principal coordinates are about 1/10 of those associated with the POD coordinates. Thus in POD analysis, the relative modal energy distribution is expressed by the principal coordinates, while the modal vectors have the same length. The opposite is true for the SPOD case. The (spatial) eigenvectors carry information regarding the modal energy distribution, while the energy levels exhibited by the principal coordinates are mode independent. In other words, the SPOD (spatial) eigenvectors reflect both global (modal) and local (spatial) energy distributions.

The POD and SPOD basis eigenvectors (or modal shapes) of the first three modes obtained for snapshot times $\tau = 4$ and $\tau = 40$ are shown in Figures 13 through 15. The first mode indicates the most energetic area in the region spanning from tap $x = 7$

through $x = 10$, which is the flow separation zone near the windward roof edge (eave). The second energetic area is located on the windward wall, especially near the roof edge. Larger values of the modes are observed for the SPOD modal shapes obtained using the data with shorter sampling times (more snapshot data, see Eq. 2.3-4). When the SPOD basis eigenvectors are normalized by their length, the shapes of the POD and SPOD modes are identical.

As mentioned in Section 2.3, the snapshot time τ needs to be larger than the correlation time. However, the increased snapshot duration leads to the results of lower fidelity, as shown in POD modal shapes in Figure 13 through 15. To ensure the fidelity of the analyses carried, while reasonably limiting the required computational time, $\tau = 4$ was chosen as the base data sample duration, in the analyses presented hereafter.

In analyses carried out for the 1st row frame, SPOD was applied for wind directions of 0°, 45° and 90°. For references in subsequence analyses, cumulative energy is displayed for these cases, in Figure 16. It can be seen that the 90° wind direction system needs first 9 modes to capture 90% of total energy while only the first 8 modes are needed for 0° wind direction. Thus it is the most complex systems among the wind direction cases considered for 1st row frame. The 45° wind system requires first 5 modes to capture 90% of total energy, indicating the system of intermediate complexity.

3.4 Application of Extrapolation Tools – GPOD and LSE

3.4.1 Reference Tap Selection

After SPOD analysis had been done, the required parameters are obtained for matrices $[M]$ and $\{f\}$ needed in Eq. 2.4-1 to calculate $\hat{a}(t, n)$. It should be noted that the

accuracy of the reconstructed principal coordinates $\hat{a}(t,n)$, is affected by the condition number $\kappa(M)$ of the matrix $[M]$. As discussed in Section 2.4, this factor is taken into account when a set of the reference taps is established. The algorithm described in Section 2.4.2 was first applied on 15th row frame, 90° wind direction. Subsequently, the cases of 1st row frame for three wind directions were considered. The layout of reference taps defined by GPOD algorithm is compared with the layout of the empirically selected taps.

Following the algorithm discussed in Section 2.4.2, the selection of the first reference tap is governed by maximization of modal variation, which is the difference between the sum of the diagonal elements and the sum of the off-diagonal elements of matrix $\left[M_x^{(1)}\right]$. For tap number x (x=1, 2, ..., 27) assumed as a candidate for the reference tap r1, the reference tap was updated in a single row matrix $:_{\text{ref}}^{(1)} = [x]$. The first eleven modes were found to contain 95% of the energy of the analyzed pressure field (see Figure 10). Therefore, $\left[M_x^{(1)}\right]$ comprising of first eleven modal eigenvectors was formulated and used. The entry (i,j) in matrix $\left[M_x^{(1)}\right]$, of dimension (11 x 11), was calculated using Eq. 2.4-8. The modal variation of $\left[M_x^{(1)}\right]$ is plotted in Figure 17 as a function of the candidate tap x. The maximum occurs at $x = 11$. Thus tap $x = 11$ was selected as the first reference tap, r1. It can be seen that r1 is located in the region of the high magnitude of the first SPOD eigenvector of the data, displayed in Figure 13.

The second reference point r2 was found as follows. The (2×2) modal matrix $\left[M_x^{(2)}\right]$ comprising of the first and the second modal eigenvectors ($i,j = 1,2$) was

evaluated by using Eq. 2.4-9 at the reference locations : $_{ref}^{(2)} = [\text{r1} \ x]$, where r1 was selected in the previous step and x (x=1, 2, ... 27, and $x \neq \text{r1}$) was a candidate for the reference point r2. The condition number of $\left[M_x^{(2)}\right]$ was calculated next and it is plotted in Figure 17 as a function of x. It can be seen that the smallest values of $\kappa\left(M_x^{(2)}\right)$ occur on the windward wall - taps $x = 1$ through $x = 6$. A representative location in this region, tap $x = 3$, was selected as the reference tap r2.

The third reference location r3 was determined in a similar manner. The already determined reference locations r1 and r2 and a candidate tap x (x=1, 2, ..., 27, and $x \neq \text{r1, r2}$) for r3 were used to calculate the matrix $\left[M_x^{(3)}\right]$. The matrix $\left[M_x^{(3)}\right]$ of dimensions (3 × 3), comprised of values of the first three modal eigenvectors ($i, j = 1, 2, 3$), was evaluated by using Eq. 2.4-10 at three locations : $_{ref}^{(3)} = [\text{r1 r2} \ x]$. The condition number of $\left[M_x^{(3)}\right]$ is displayed in Figure 17, as a function of candidate tap x. It can be seen that the minimum value occurs at $x = 7$. Thus tap $x = 7$ was selected as the reference tap r3. Note that r2 and r3 were located in regions of high magnitude of the 2nd and 3rd eigenvectors displayed in Figure 14 and 15, respectively. The subsequent reference locations were determined in a similar manner until the remaining reference taps (r4 ~ r27) were selected. Figure 18 shows the locations of the reference taps r1 through r8 , for the 90° wind, selected for 15th row frame. It can be seen that most of these taps are located in energetic regions of the wind-induced pressure – namely in the flow separation zone on the roof ($x = 7 \sim 12$). The locations of the first eight reference taps found for 1st row frame, and wind directions of 0°, 45° and 90°, are shown in Figure 19.

In addition to the above algorithm-based locations of the reference taps, eight approximately uniformly distributed taps, denoted herein as empirically selected locations, were chosen. The locations of these eight empirically selected reference taps are shown in Figure 20. They were used in comparative analyses carried out for 1st and 15th row frames. Taking into account fact that for most wind directions (i.e. 45° and 90°) the spatio-temporal structure of the pressure induced on the windward portion of the roof and windward wall is complex, the first reference tap r1 was empirically selected near the windward roof eave ($x = 8$) and the second reference tap r2 was chosen on the windward wall ($x = 6$). The subsequent reference six taps were approximately evenly distributed on the windward and leeward walls and on the roof portions of the frame.

3.4.2   Reconstruction of Principal Coordinates

In this section, reconstruction of principal coordinates $a(t, n)$ for the 90° wind on 15th row frame using GPOD and LSE techniques is discussed. The exact coordinates were calculated using SPOD method. Predictions involving the measured pressure time series at up to eight reference locations (r1 through r8) were carried out for all the 27 modes of the SPOD decomposition. GPOD algorithm-based (A.B.) and empirically selected (E.S.) reference taps were employed.

In the GPOD approach, the reconstructed (approximated) coordinates $\hat{a}(t, n)$ were computed by solving Eq. 2.4-1. In this analysis, the total number of the retrieved modes n (i.e. $a(1, t), a(2, t), ..., a(n, t)$) should not exceed the total number of the reference taps N (i.e. $:_{ref} = [r1 \quad r2 \quad ... \quad rN]$). As mentioned in Section 2.4, the reference tap layout may greatly affect the reconstruction accuracy. Therefore only

algorithm-based reference taps were employed herein in GPOD reconstruction. In LSE analysis, $\hat{a}(t,n)$ were determined from Eq. 2.5-6. Note that in this approach the number of retrieved modes is not restricted by the number of the reference taps. Both the algorithm-based (A.B.) and empirically-selected (E.S.) reference taps were used in the LSE method.

To compare the principal coordinate reconstruction results of GPOD and LSE analyses, the residual error associated with mode n, defined below, was used

$$\varepsilon(n) = \frac{\sqrt{\dfrac{1}{T}\displaystyle\sum_{t=1}^{T}(\hat{a}(t,n)-a(t,n))^2}}{\sigma(n)} \qquad\qquad 3.4\text{-}1$$

where the numerator is the time averaged residual and the denominator $\sigma(n)$ is the standard deviation of $a(t,n)$.

The residual errors associated with 1st, 3rd, 5th and 7th modes are displayed in Figure 21 as functions of the number of the reference taps (i.e. $r_{ref} = [r1], [r1 \quad r2], ..., [r1 \quad r2 \quad \cdots \quad r8]$) used in the reconstructions. It can be seen that the principal mode reconstructions improve as the number of the reference taps is increased. The GPOD is unable to retrieve the nth mode when the total reference tap number is lower than n. So, the GPOD residual errors of nth mode in Figure 21 are displayed only when this condition is satisfied. The standard deviations of the corresponding reconstructed principal coordinates presented in Figure 21 are shown in Figure 22. It is observed in Figure 22, that the reconstructed $\hat{a}(t,n)$ obtained using GPOD were larger in magnitude than the exact values of the principal coordinates $a(t,n)$. As the number of the employed reference taps was increased, this overestimation was reduced. For LSE method, Figure 21 shows that reconstructions are generally better than those obtained

using GPOD. Figure 22 shows that the reconstructed coordinates were in general underestimating the true coordinates $a(t,n)$ and that this underestimation was reduced when the number of the reference taps was increased.

In LSE, steeper drops in the residual error (Figure 21) and steeper rises of reconstructed principal coordinates' standard deviation (Figure 22) of nth mode occurred when n algorithm-based reference taps were used. For empirically selected taps, similar trends are observed for 1$^{\text{st}}$, 3$^{\text{rd}}$ and 7$^{\text{th}}$ modes. However the 5$^{\text{th}}$ mode was not significantly improved when first 5 taps were used. Improved convergence (steeper drop in the residual error) in reconstruction of $\hat{a}(t,n)$ is due to larger correlation between $C_p(t,rn)$ and $a(t,n)$. The high correlation positions coincide with positions with high eigenvector amplitudes. The GPOD algorithm automatically labeling n^{th} tap rn among high magnitude locations of nth eigenvector ensures that the first n reference taps are used to extrapolate pressures that capture first n modes. On the other hand, the reference taps empirically selected (e.g. by choosing energetic locations on the building surface) may not sufficiently capture the modal energy of the pressure.

The relative inaccuracy, overestimation and limited number of modes of GPOD reconstruction of principal coordinates will lead to inaccurate extrapolation of the pressure. The tap selection algorithm embedded in GPOD method is useful to identify the energetic locations in order. The relatively accurate results of LSE reconstruction lead to possible benefits of the use of a combination of GPOD tap selection and LSE extrapolation. Since the reference taps are labeled in energetic order, it is expected that that the decision regarding the sufficient number of taps to ensure accurate pressure

extrapolations can be made based on the assessment of the system complexity, e.g. as displayed by the cumulative energy E_i.

3.4.3 Extrapolation of Wind-Induced Pressure

In this section, pressure extrapolations using the algorithm-based (A. B.) (Figures 18 and 19) and empirically selected (E. S.) reference taps (Figure 20) are described. Locations on the 15th and 1st row frames are considered. The pressures at the target locations are extrapolated from measured pressures at the reference locations using LSE (Eq. 2.5-1) with 1, 3, 5 and 8 reference taps. The first n reference taps are selected as $:_\mathrm{ref} = [\mathrm{r1} \quad \mathrm{r2} \quad ... \quad \mathrm{r}n]$.

To assess the accuracy of the extrapolated pressure, means, standard deviations, peaks and residual errors of the extrapolated pressures are evaluated. The mean and standard deviation of measured pressures are shown in Figure 23 and 24 for the cases considered in the extrapolation analyses. Figure 25 shows the observed and estimated peaks. The pressure peak estimates were obtained using methodology described by Endo (2011). The residual error of the pressure extrapolation is defined as follows:

$$\varepsilon(x) = \frac{\sqrt{\dfrac{1}{T} \sum_{t=1}^{T} \left(\hat{C}_p(t,x) - C_p(t,x) \right)^2}}{\sigma(x)} \qquad \text{3.4-2}$$

where x denotes the tap location, T represents the total number snapshots recorded, σ denotes the standard deviation of exact pressure and $\hat{C}_p$ represents the extrapolated pressure. Since mean pressures were accurately predicted during extrapolations, the presented comparisons were restricted to the pressure standard deviations and peaks.

For a representative case of 90° wind and 15th row frame, the standard deviations, peaks and residual errors of the extrapolated and original (measured) pressures are displayed in Figures 26 through 28, respectively. The pressure standard deviations and peaks showed that the extrapolated pressures at locations between reference taps were generally underestimated. The residual errors at locations adjacent to the reference taps are smaller (pressures are better approximated) than locations far from the reference taps. When the lower number of the reference taps (e.g. 1 and 3 taps) were used, the extrapolations utilizing the algorithm-based and empirically selected layouts duplicated the major feature of energetic (significant) pressures. By increasing the reference tap number (e.g. 5 and 8 taps), secondary energetic features of the pressure were also captured. Thus, as expected, an increase in the number of the reference taps improves the accuracy of the pressure extrapolations.

Similar results for 1st row frame, the standard deviations and peaks of extrapolated pressures, for 90°, 45° and 0° wind directions, are shown in Figures 29 through 34, respectively.   It can be seen that when lower number of the reference taps were used (e.g. 1 and 3 taps), the primary energetic pressure features were captured by using algorithm-based layouts while they were not captured when empirically selected reference layouts were employed. These differences were more pronounced for 90° and 0° wind directions. When higher number of the reference taps were used (e.g. 5 and 8 taps), both the algorithm-based and empirically selected reference taps worked well for 45° and 0° wind directions. However, the evenly spaced reference taps (selected empirically) led to significant underestimation of the pressure in the primary energetic

region (tap $x = 7$ to 12) for 90° wind direction, where the algorithm-based taps were heavily packed.

As mentioned in Section 3.4.2, the number of the total algorithm-based reference taps needed can be related to the system complexity, as measured by the cumulative energy E_i. If this level is set to 90%, the required numbers of the reference taps, established based on prior SPOD analyses (see Section 3.3), are 8 for 90°-wind-15th-row case and for 0°-wind-1st-row case, 5 for 45°-wind-1st-row case, and 9 for 90°-wind-1st-row case. Examination of the standard deviations and peaks of the extrapolated pressures and comparisons with the corresponding values extracted from the original pressures, in Figures 26 through 34, confirms these assertions.

3.5 Non-stationary Analysis

3.5.1 Introduction to Non-stationary Events

The tools for tackling non-stationary problems introduced in Section 2.6 are applied in this section. Analysis of the pressures acquired at tap locations on the 1st row frame, for wind directions 0°, 45° and 90° was of main focus.

The 1st row frame non-stationary case was artificially created by combining three segments of the pressure time series obtained for three wind directions: (1) first 1/3 portion of the pressure time series obtained for wind direction of 0° (time series index $t =$ 1 through 9666); (2) second 1/3 portion of the pressure time series obtained for wind direction of 45° (time series index $t =$ 9667 through 19332); and (3) third 1/3 portion of the pressure time series obtained for the wind direction of 90° (time series index t=19333 through 29000).

For the 1st row frame non-stationary case, Figure 35 compares the means and standard deviations of the non-stationary and stationary cases. The mean value of non-stationary case is observed as passing between the values for the three stationary cases. However, the standard deviation for the non-stationary case is for the most part higher than for the stationary cases.

The wavelet de-noising and two-stage moving averaging techniques, as described in Section 2.6, were applied to filter out the time-varying means, the time-varying standards deviation and the normalized fluctuations. Then SPOD was applied to the three parts of the generated non-stationary time series. With the SPOD basis eigenvectors obtained, the modified GPOD algorithm described in Section 2.6.3 was applied to specify the reference tap placement. Finally, the pressure extrapolations were carried out using the proposed techniques summarized in Figures 4 and 5. Extrapolated results using non-stationary consideration (Figures 4 and 5) are compared with results obtained from stationary assumption. The means, standard deviations, peaks and residuals of extrapolated pressures were calculated and used to compare the difference between the results of the analyses based on the stationary assumption and non-stationary considerations of the pressure time series.

3.5.2 Time-varying Mean, Time-varying Standard Deviation and Normalized Fluctuation

In this section, the non-stationary pressure time series introduced in previous section are decomposed into its three non-stationary elements – time-varying mean $\mu_p(t)$, time-varying standard deviation $\sigma_p(t)$ and normalized fluctuation $z_p(t)$. To accomplish

these tasks, the wavelet de-noising and two-stage moving averaging techniques as described in Section 2.6.2 were applied. To filter out time varying mean, a set of de-noising parameters was first determined: (1) The decomposition-level ($j = 9$), which corresponds to the time window width $2^j = 2^9 = 512$; (2) Birge–Massart parameter $\alpha = 3$; and (3) Type of wavelet ('db4'). Note that decomposition level j is crucial in de-noising, as a wider window leads to smoother de-noising results, i.e. the time-varying mean. After preliminary trials, the level $j = 9$ was established to be optimal – sensitive enough to capture significant features associated with the stationary pressure time series at different approaching wind directions. After the time-varying mean was determined, two-stage moving averaging was applied to the zero mean non-stationary time series, $x_p(t)$ ($x_p = C_p(t) - \mu_p(t)$), to calculate the time-varying standard deviation $\sigma_p(t)$. Finally the normalized fluctuation $z_p(t)$ was obtained using Eq. 2.6-1.

The time-varying mean and standard deviation envelopes at tap $x = 21$ on 1st row frame are compared in Figure 36 with the stationary mean, stationary standard deviation envelopes and non-stationary pressure time series. In Figure 37, the time-varying quantities are compared with stationary quantities (for different potions of the time series) at different locations. Good agreement between the time-varying and stationary quantities can be observed.

SPOD was applied for the three non-stationary elements. Using the data obtained for snapshot time ($\tau = 4$) employed in stationary analyses, each non-stationary element was decomposed into 27 modes. The cumulative energy E_i is shown in Figure 38 and Table 1. It can be seen that $\sigma_p(t)$ fluctuates more than $\mu_p(t)$, and that $z_p(t)$ fluctuates

more than $\sigma_p(t)$. As depicted in Figure 38 and 37, the normalized fluctuation is the main element that captures the non-stationary aspect of the system's energy.

The first two SPOD eigenvectors of each non-stationary element are shown in Figure 39. Locations of high eigenvector magnitudes indicate the high degree of fluctuation of the time series in these areas. The low degree of fluctuation of time-varying mean at tap $x = 8$, when compared with time-varying mean at tap $x = 21$, is observed. This is in agreement with the time series exhibited in Figure 37. For time-varying standard deviation, the first modal shape implies a small fluctuation at tap $x = 7$ and relatively high fluctuation at tap $x = 21$, and the time series of these two locations are shown in Figure 37. Since the mean and standard deviation of a stationary pressure time series reflect the building geometry (or approaching wind angles), the modal shape of time-varying mean and time-varying standard deviation thus indicate the directional sensitivity of a location on building surface. The first two modal shapes of the normalized fluctuation are smooth - flat shapes. This topology is expected since these modes represent properties of normalized time series of the pressure.

3.5.3 Reference Tap Selection for Non-stationary Data

The reference taps were selected for the non-stationary pressure time series by using modified GPOD algorithm described in Section 2.6.3. The SPOD eigenvectors of each non-stationary element obtained in Section 3.5.2 were utilized to find the reference taps.

The first tap r1 is selected by considering the largest sum of modal variations of three non-stationary elements. In order to ensure contribution of each non-stationary

element, the eigenvectors of each non-stationary element (Φ^μ, Φ^σ, and Φ^z) were first normalized by the length of its first mode. For tap number x (x=1, 2, ..., 27) assumed as a candidate for the reference tap r1, the reference tap layout was updated : $\overset{(1)}{\text{ref}} = [x]$. Evaluate matrices $\left[M_x^{\mu(1)}\right], \left[M_x^{\sigma(1)}\right]$ and $\left[M_x^{z(1)}\right]$ by using similar way presented in Eq. 2.4-8. The modal variation of each non-stationary element and the summation along candidate locations x are shown in Figure 40. The optimized first non-stationary reference tap, of 1$^{\text{st}}$ row frame, is chosen to be $x = 21$, which corresponds to largest summation of modal variations. The result can be checked with the first eigenvectors of each element shown in Figure 39, in which tap $x = 21$ is located at a optimized location with high amplitudes of each first eigenvector.

For the selection of the second tap r2, a similar strategy to find a optimized location is to look at the smallest sum of condition numbers of each non-stationary element. The threshold mode numbers n_{th}^μ and n_{th}^σ for the time-varying mean and time-varying standard deviation, respectively, are first selected based on the related level of cumulative energy, say 90%. Based on Table 1, n_{th}^μ was set to 2 and n_{th}^σ was equal to 3. It was observed that current selection number ($n = 2$) did not exceed any threshold mode number ($n_{\text{th}}^\mu = 2, n_{\text{th}}^\sigma = 3$). So the matrices $\left[M_x^{\mu(2)}\right], \left[M_x^{\sigma(2)}\right]$ and $\left[M_x^{z(2)}\right]$ were of size (2×2) and calculated using Eqs. 2.6-3, 2.6-4 and 2.6-5 with a trial reference tap layout : $\overset{(2)}{\text{ref}} = [\text{r1} \ x]$. The condition numbers $\kappa\left(M_x^{\mu(2)}\right), \kappa\left(M_x^{\sigma(2)}\right), \kappa\left(M_x^{z(2)}\right)$ and the summation of the three, $\kappa\left(M_x^{(2)}\right)$, are shown in Figure 41, as function of candidate locations x. The reference location r2 was chosen to be $x = 4$, based on the minimization of $\kappa\left(M_x^{(2)}\right)$. Examination of the second eigenvectors in Figure 39 of each

non-stationary element revealed that r2 was located at a optimized location of high eigenvector amplitudes. Following the procedures described in Section 2.6.3, the remaining reference tap placing order (r3 to r27) was established. The positions of the first five identified taps, r1 through r5 , are indicated in Figure 42, for the 1st row frame and non-stationary case.

3.5.4   Comparison of Different Assumptions on Non-stationary Extrapolation

In this section, the non-stationary extrapolation results using the reference taps specified in the previous section (Figure 42) are discussed. The statistical parameters obtained by applying the proposed non-stationary consideration (Figures 4 and 5) and the stationary assumption were employed for extrapolations. Stationary assumption means the statistical parameters used for extrapolation were obtained by treating the non-stationary data as stationary and the extrapolation follows the procedure described in Section 2.5.1. Because the non-stationary data were obtained by composite stationary time series measured for three different wind directions, the statistical parameters obtained from non-stationary data were expected to be used for extrapolation if the incoming pressures belong to one of three stationary winds. Thus, the pressures at target locations $\hat{C}_p(t, x_{\text{target}})$ were extrapolated from reference pressures obtained by stationary winds of 0°, 45° and 90° directions. The comparisons of the non-stationary consideration and the stationary assumption are schematically shown in Figure 43.

The pressure means, standard deviations, peaks (discussed in Section 3.4.3) and residual errors of extrapolated pressures defined in Eq. 3.4-2 are shown in Figure 44, 45 and 46, for 90°, 45° and 0° wind directions, respectively. The mean pressures were

accurately predicted in the extrapolated pressures using non-stationary consideration. Mean pressures of 90° and 45° winds were also predicted well by applying the stationary assumption, but little difference was found in predicting the mean pressures of 0° wind direction. For standard deviations and peaks of extrapolated pressures, the stationary assumption led to closer predictions than non-stationary consideration at target locations for 90° and 0° wind directions. However this was not always true when looking at target tap $x = 8$ of 45° wind direction.

For the residual errors of three wind directions, the extrapolated pressures were generally more accurately predicted if the non-stationary consideration was applied. This observation was apparently showed at locations $x = 8$ through 13 of 0° wind direction. It is reasonable since there are three sets of linear statistical parameters (i.e. $[B]^\mu, [B_0]^\mu, [B]^\sigma, [B_0]^\sigma, [B]^z, [B_0]^z$) obtained in the non-stationary consideration, which are expected to extrapolate pressures at the target taps more accurately than one set of linear statistical parameters obtained in stationary assumption. Thus, the proposed method (summarized in Figure 4 and 5) appears be a viable tool for use in data extrapolations for non-stationary cases.

Chapter 4   Conclusions and Recommendations

In the research described in this thesis, analysis and reduction of stationary and non-stationary wind-induced pressures on a generic low-rise building was carried out. The main aspects and findings of the research efforts focused on the stationary pressure data are summarized as follows:

- Wind induced pressures were analyzed by modal decomposition tools (POD and SPOD) in order to identify the best correlated energetic pressure structures.

- Basis eigenvectors obtained using SPOD were used because its length reflects modal energy and its shape reflects spatial allocation of modal energy.

- The overall objective of the study was to establish an efficient method for reduction of the amount of data used to describe the wind pressures induced on external surfaces of low buildings, while preserving the data fidelity suitable for wind engineering analyses.

- The extrapolation tools (GPOD and LSE) were found to be more efficient than the modal reduction tools (POD and SPOD) in data reduction. This conclusion is in agreement with related findings reported in literature.

- When compared with LSE, GPOD was found to be less accurate. The number of the modal contents that can be reconstructed by using GPOD is also limited by the number of the reference taps.

- The algorithm-based reference tap selection embedded in GPOD was found to lead to more accurate extrapolation of the wind pressure data than the empirical selection.

- A hybrid approach comprising of use of GPOD algorithm-based reference tap selection and LSE extrapolation is suggested for development of reduced models of wind pressures induced on low-rise buildings.

- By increasing the number of the algorithm-based reference taps, it was possible to significantly improve the accuracy of the pressure extrapolation. In addition to the primary energetic features, also secondary features of the pressure pressures were captured.

- The number of the algorithm-based reference taps needed to ensure accurate reconstruction of the pressures was related to the spatio-temporal complexity of the pressures, which is exhibited by the cumulative energy revealed by modal decomposition.

The main outcomes of the investigations carried out for non-stationary cases are summarized as follows:

- Non-stationary time series of wind induced pressures were decomposed into three elements: the time-varying mean, the time-varying standard deviation and the normalized fluctuation.

- Use of hybrid GPOD-LSE extrapolation developed for the stationary cases was found to be suitable for analysis and model reduction for non-stationary time series of wind-induced pressures.

- The non-stationary extrapolations generated using the proposed method was compared with extrapolations obtained using stationary assumption employed for

non-stationary data. It was found that the proposed method led to more accurate extrapolations of the non-stationary pressures.

- The methodology for extrapolation of non-stationary wind pressures, as proposed in this thesis, appears to be a suitable tool for similar analyses of other non-stationary data.

The recommendations proposed for the follow-up research are summarized as follows:

- If the pressure time series are of small spatial dimension, the length of the basis eigenvectors obtained using POD can be rescaled to be proportional to modal energy (indicated by eigenvalues). Thus modal and spatial energy information indicated by eigenvectors is representative of full time series (rather than snapshots).

- The rescaled POD basis eigenvectors can be used in reference tap selection algorithm. More precisely located reference taps can be anticipated.

- The non-stationary pressure time series, which were artificially combined by different sections of stationary data, were used for the proposed non-stationary extrapolations. To validate the proposed method, more realistic non-stationary data (e.g. measured during field experiments) should be used.

Table 1: Cumulative energy of non-stationary elements

Cumulative energy / Non-stationary elements	90%	95%	99%
Varying Mean	N/A	2nd	3rd
Varying STD	3rd	5th	9th
Norm. Fluctuation	9th	13th	21th
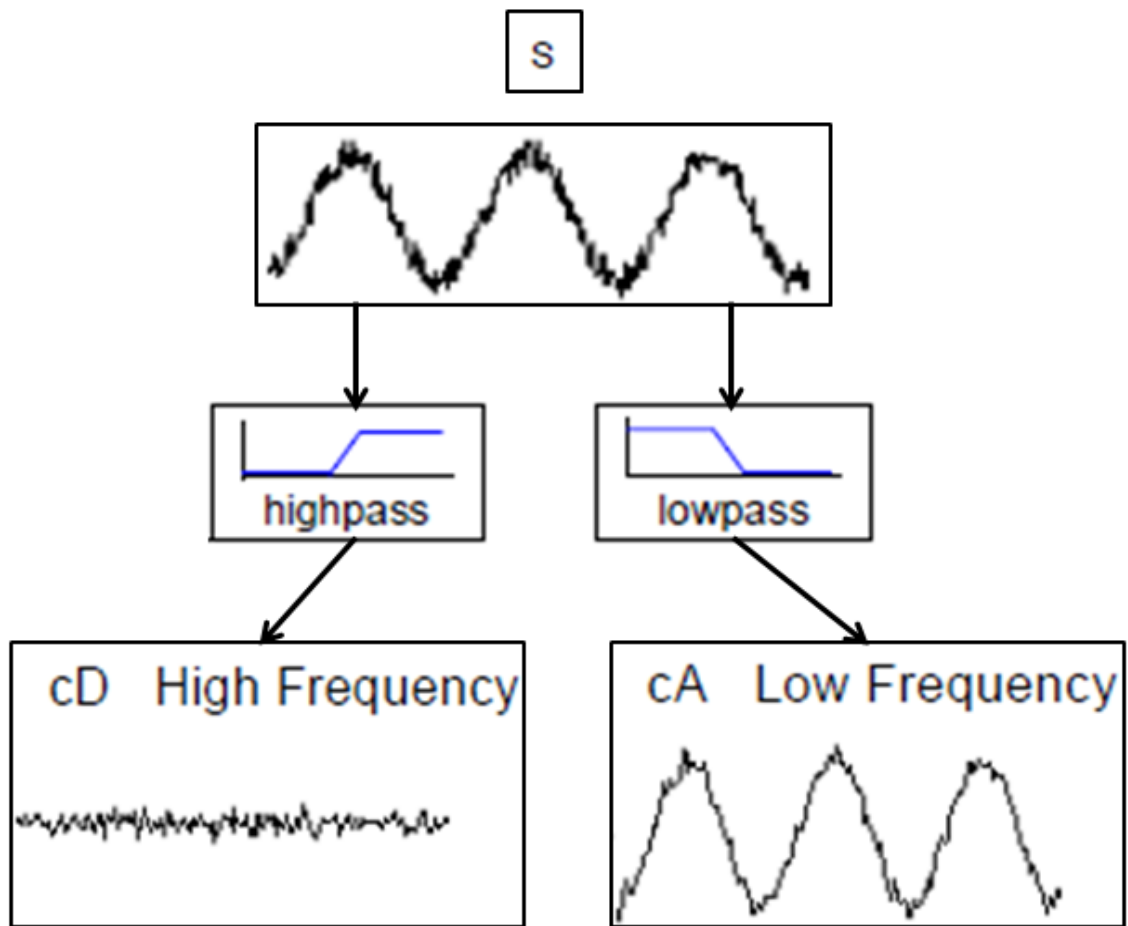
Figure 1: Single level wavelet decomposition (after [14])
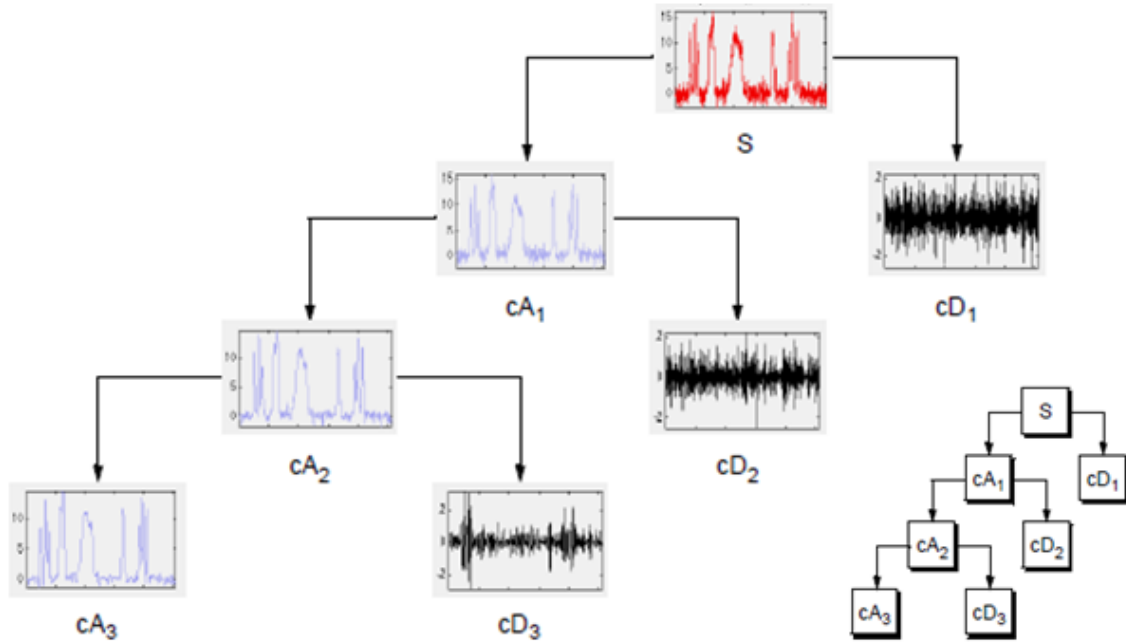
Figure 2: Multi-level wavelet decomposition (extracted from [14])
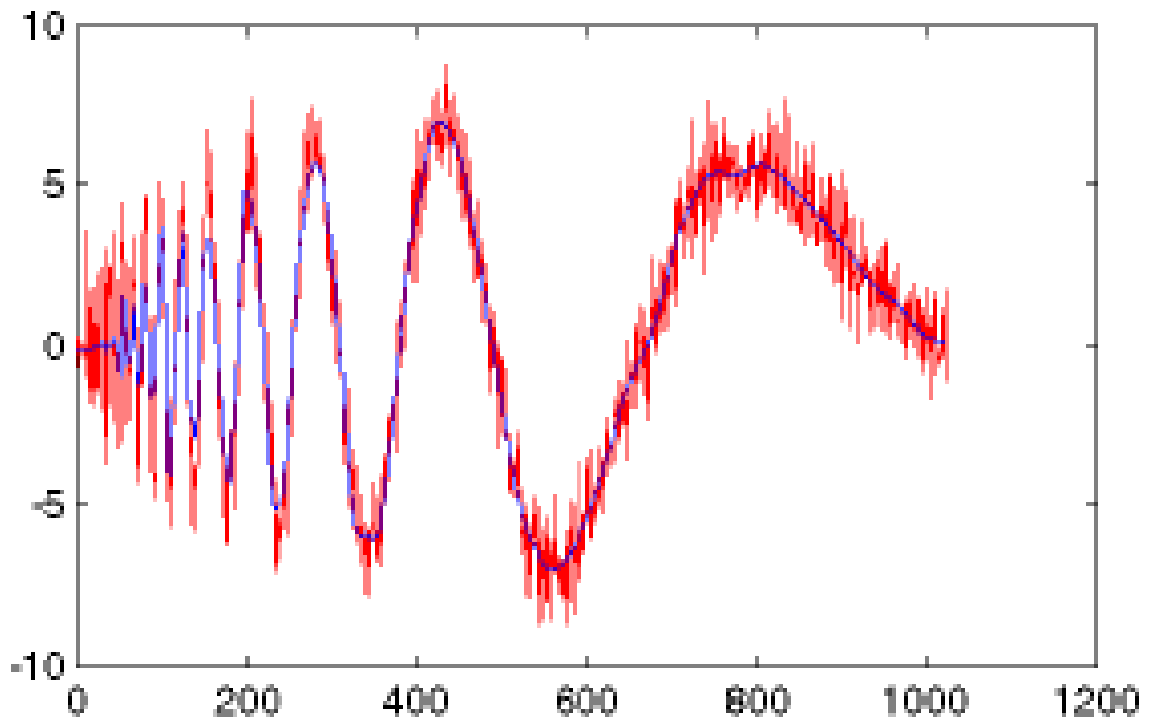
Figure 3: The original signal (red) and the de-noised signal (blue) (extracted from [14])
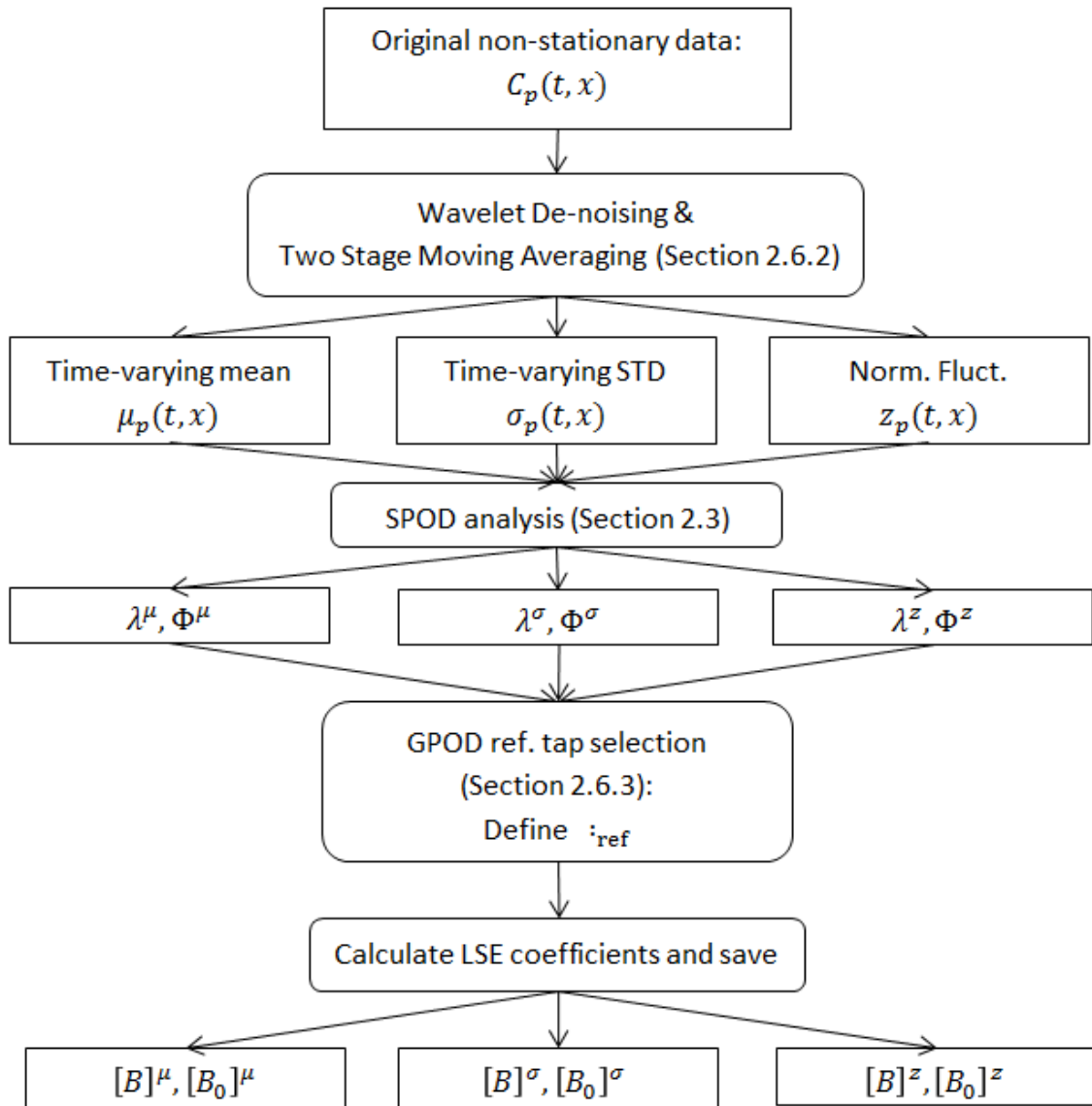
Figure 4: First step of proposed non-stationary extrapolation algorithm
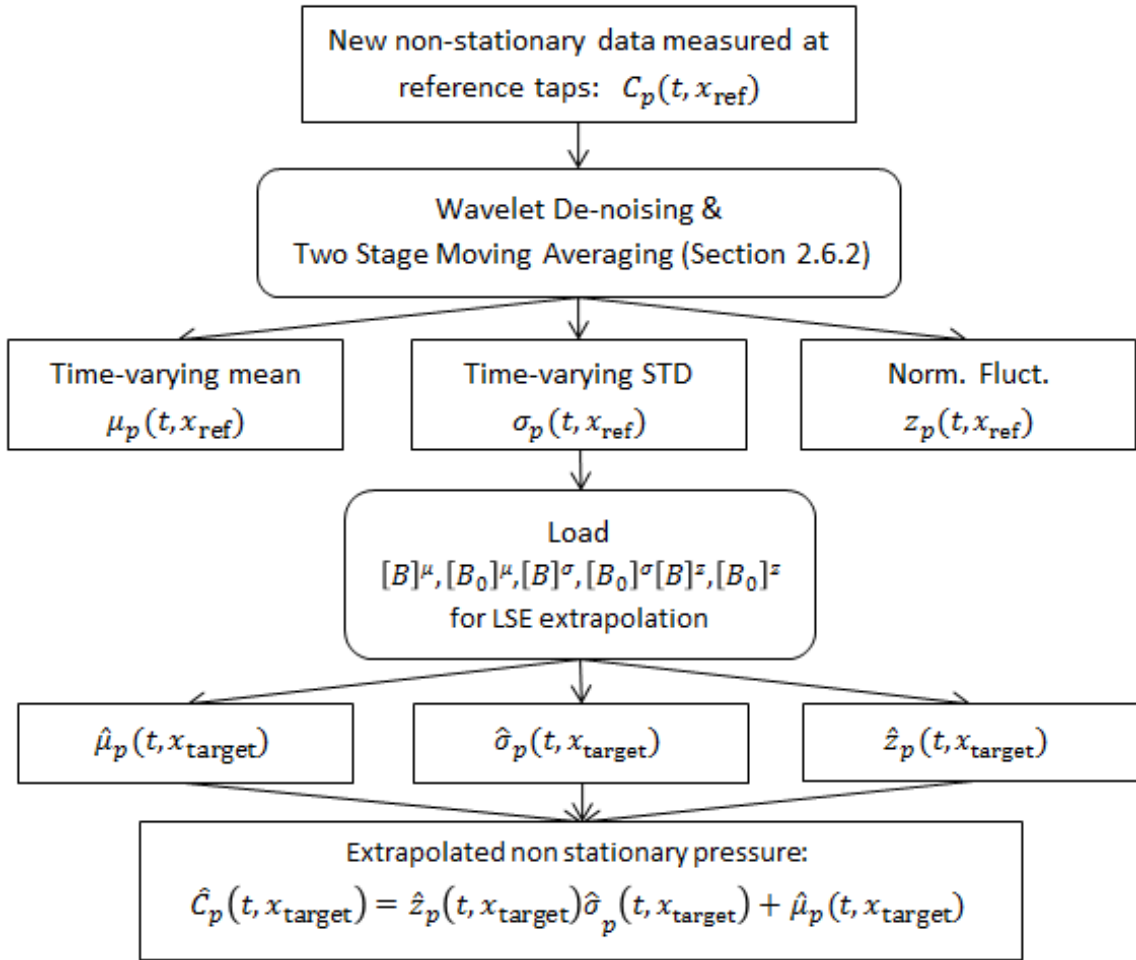
Figure 5: Second step of proposed non-stationary extrapolation algorithm
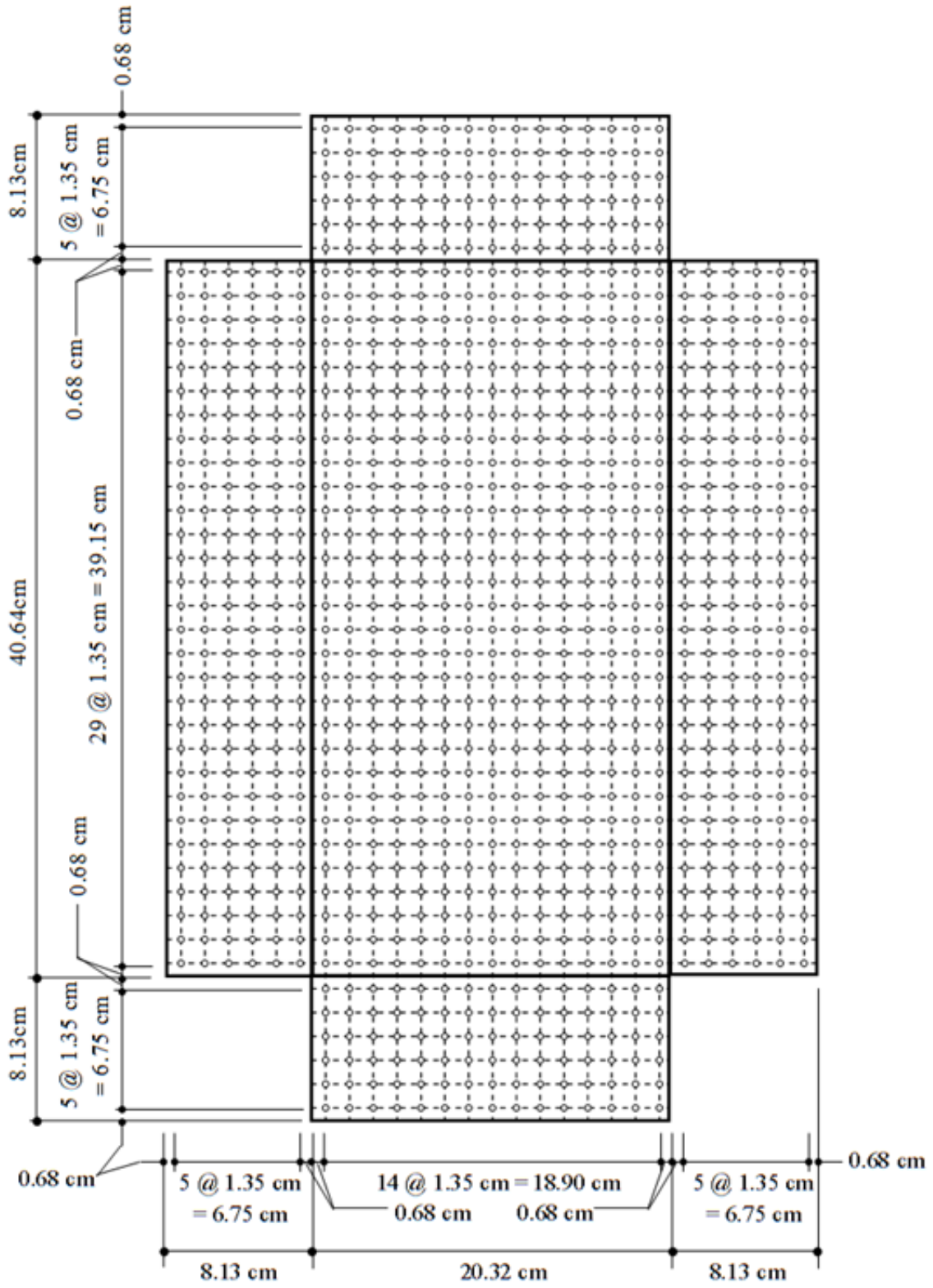
Figure 6: Geometry of the building model and tap locations
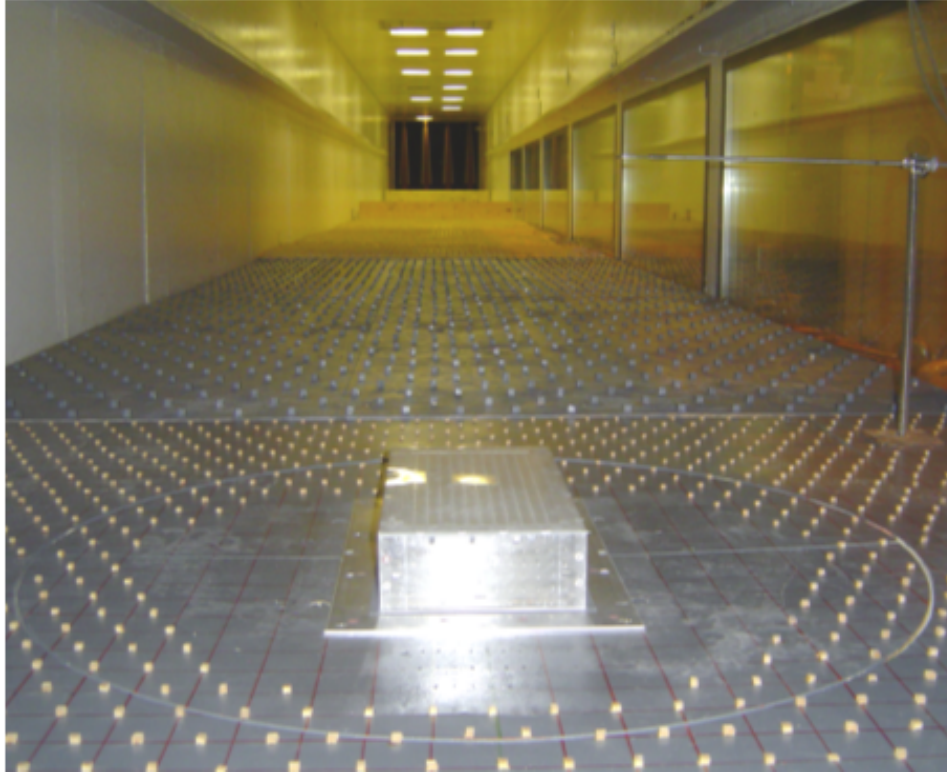
Figure 7: Model inside wind tunnel test section
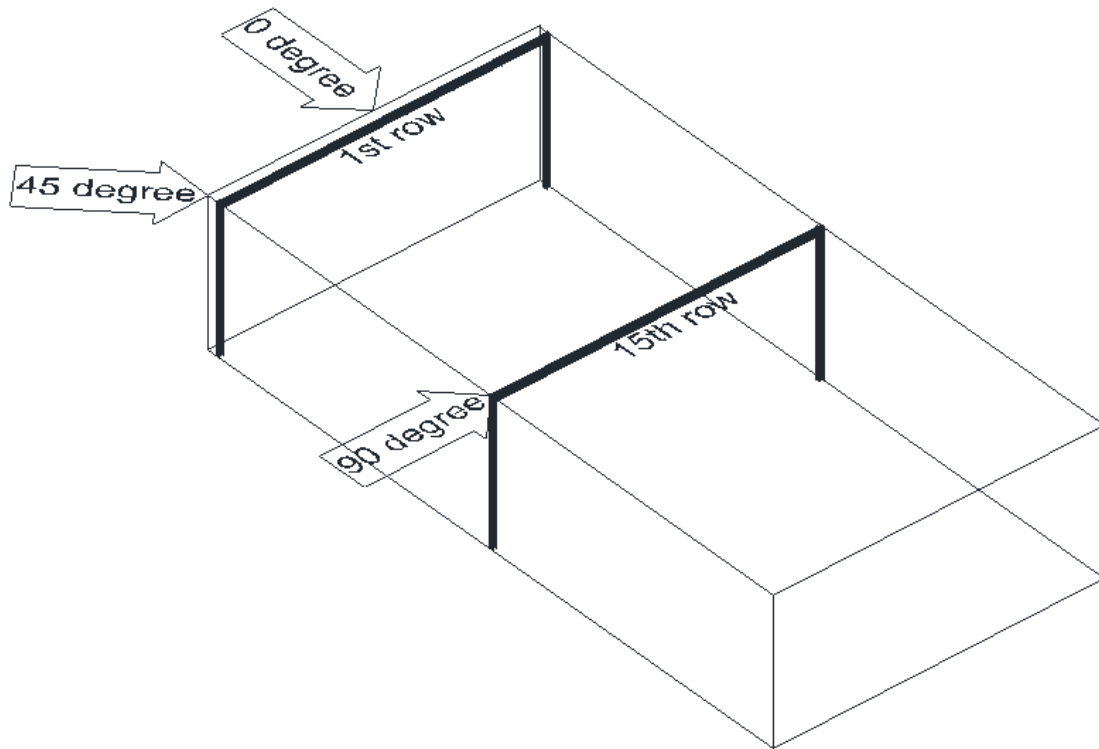
Figure 8: Wind direction definition and locations of analyzed structural frames
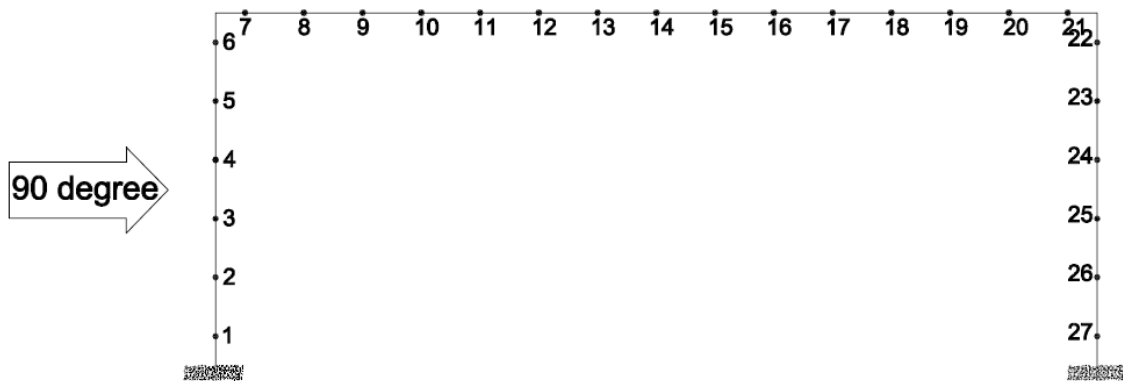
Figure 9: Numbering of pressure taps on structural frames
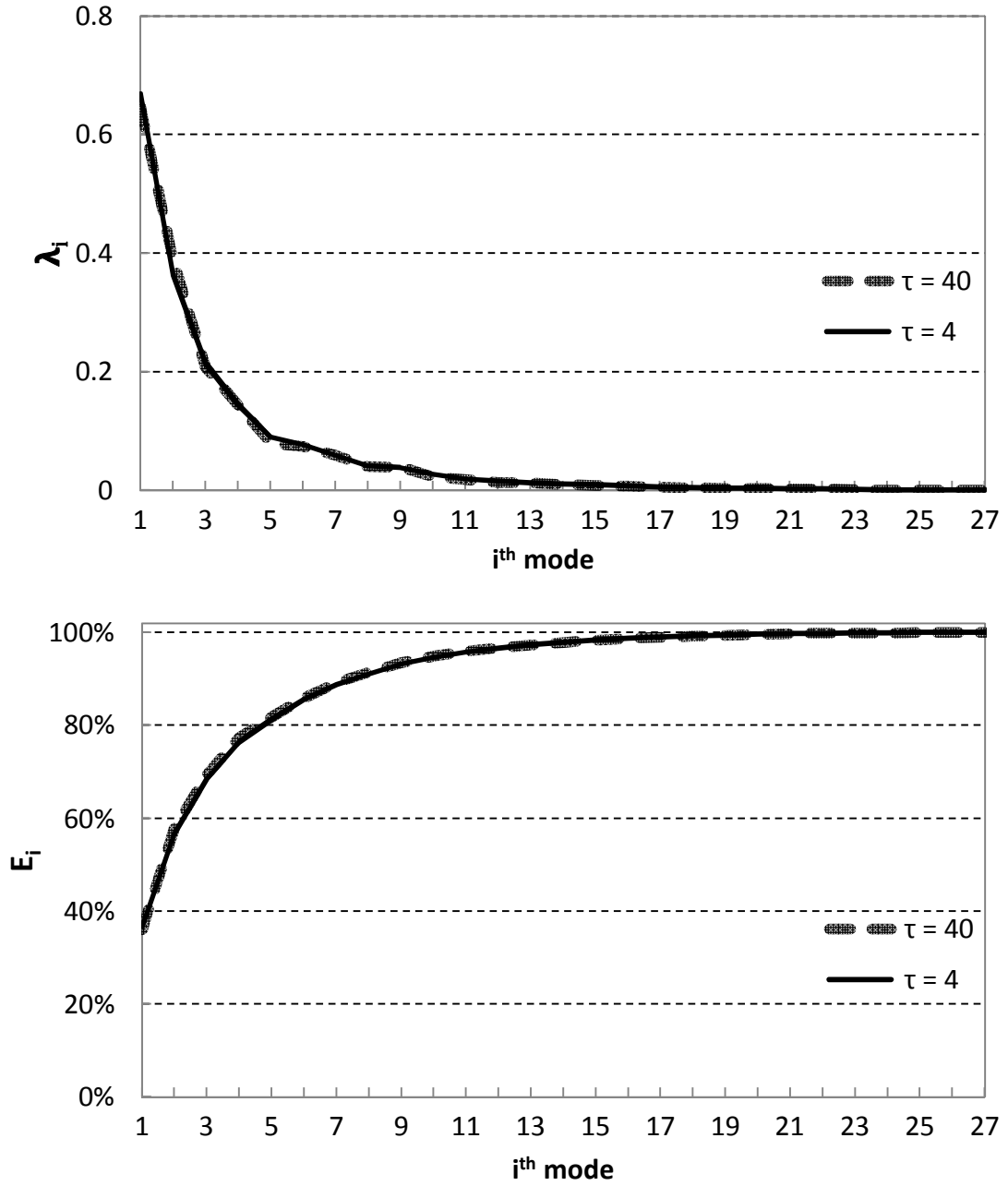
Figure 10: Eigenvalues and the relative cumulative energy of wind induced pressures, obtained for 90° wind on 15th row frame
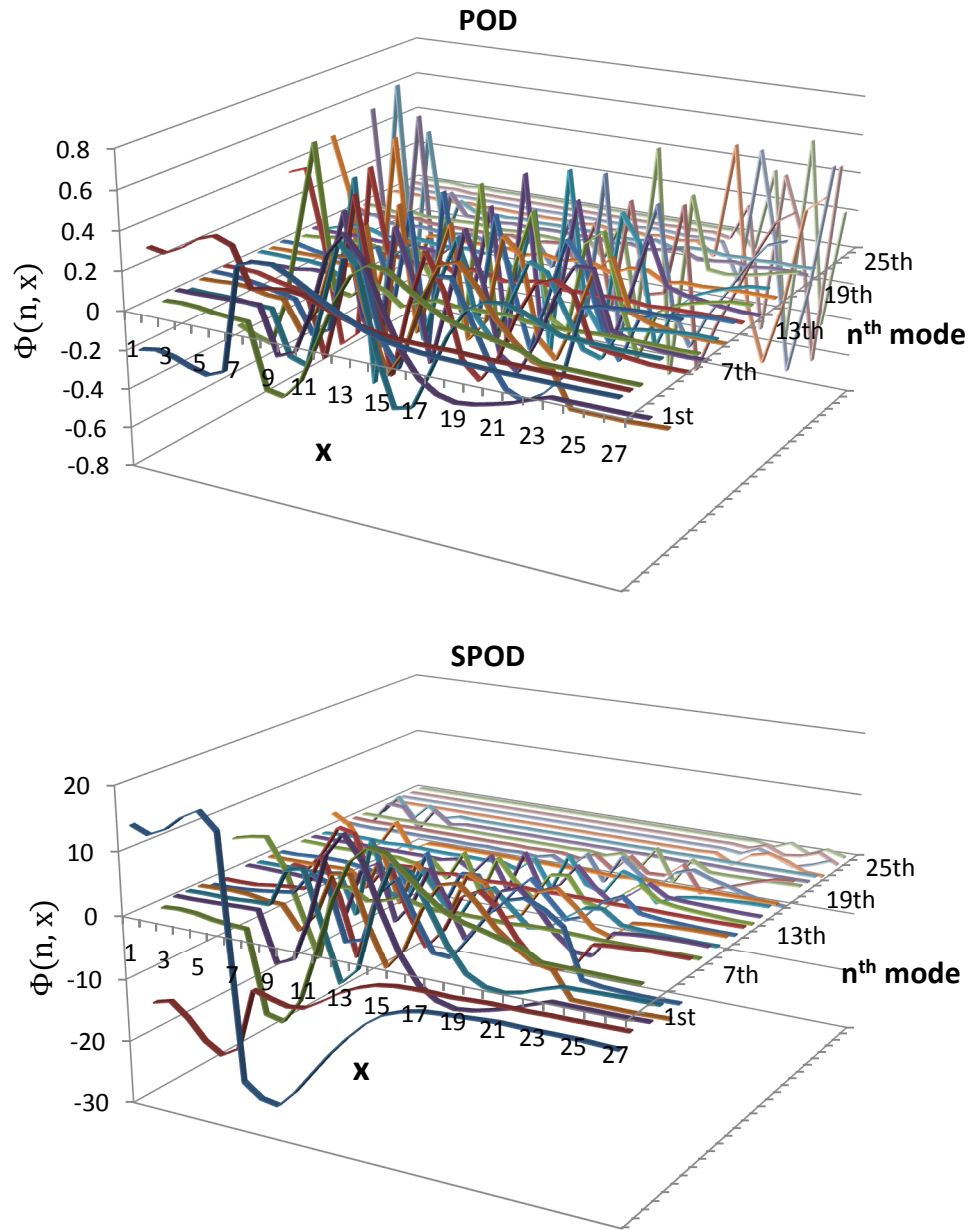
Figure 11: POD and SPOD basis eigenvectors, obtained from pressure snapshots ($\tau = 4$) of 90° wind, 15th row frame
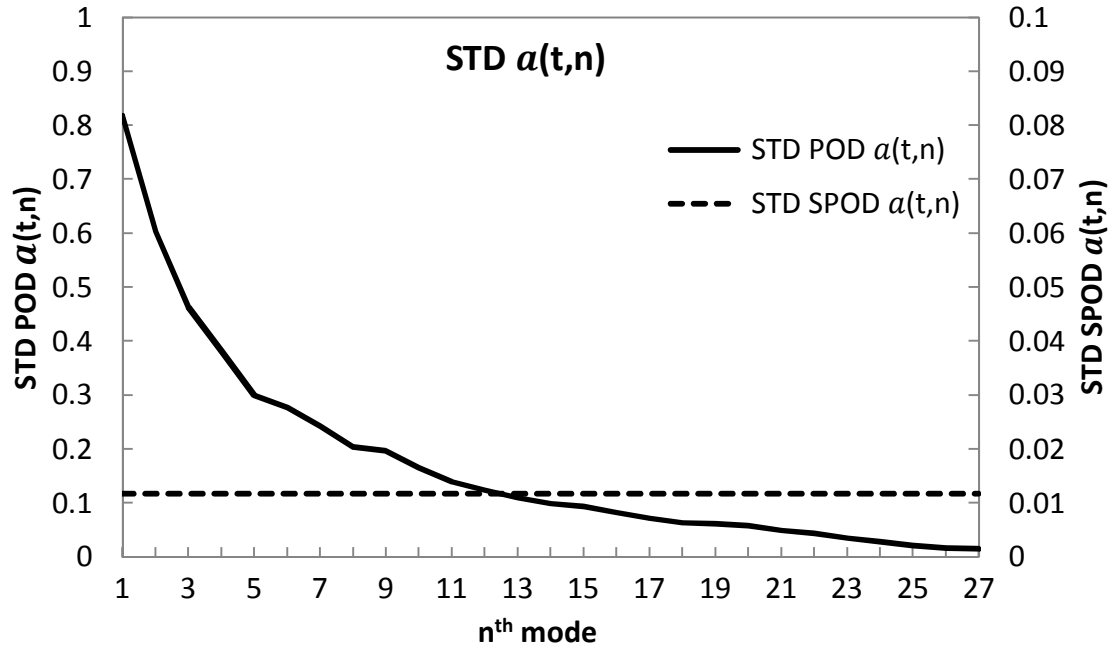
Figure 12: Standard deviation of POD and SPOD principal coordinates of $\tau = 4$ snapshots, 90° wind and 15th row frame
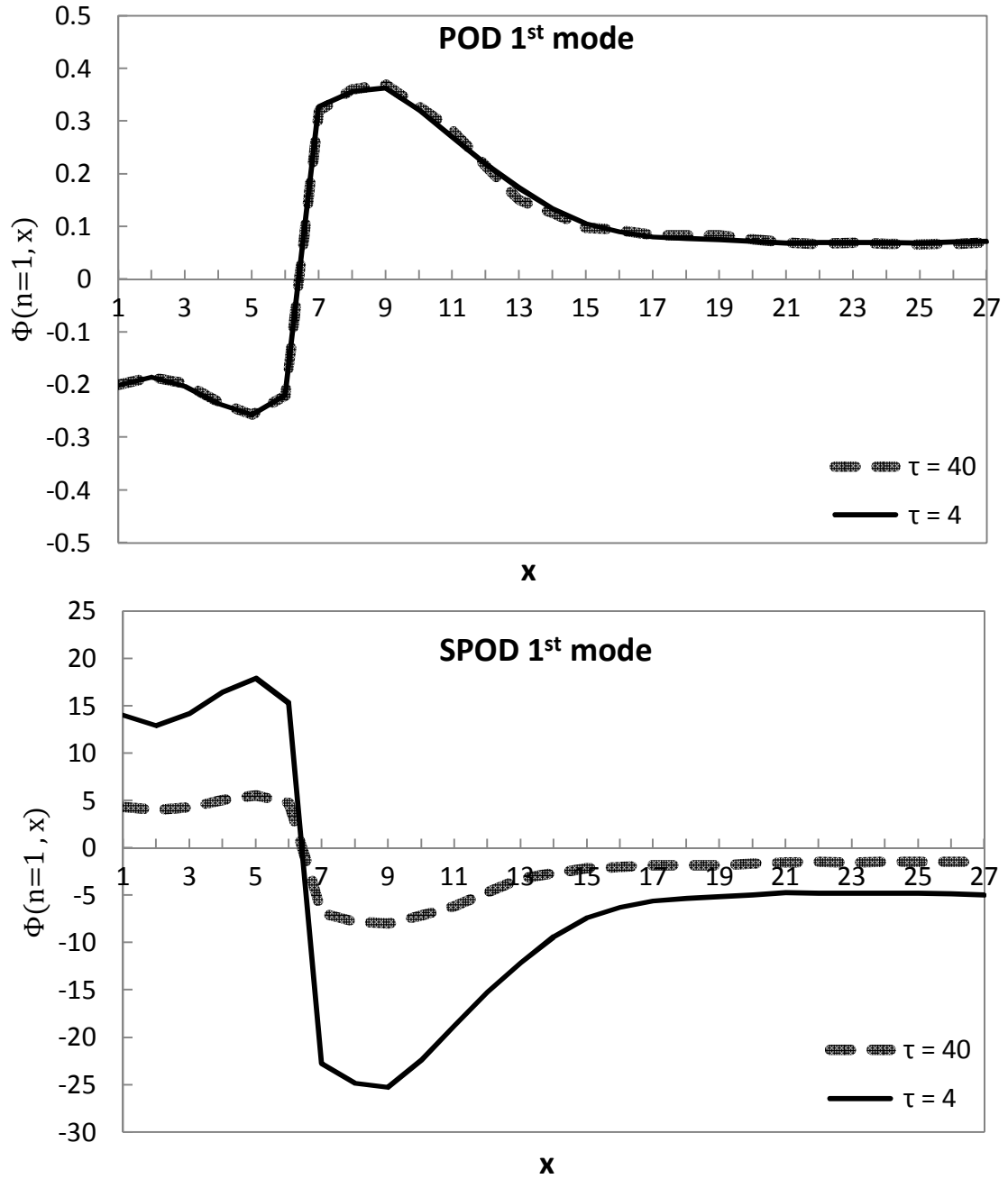
Figure 13: POD and SPOD 1st basis eigenvectors for 90° wind, 15th row frame
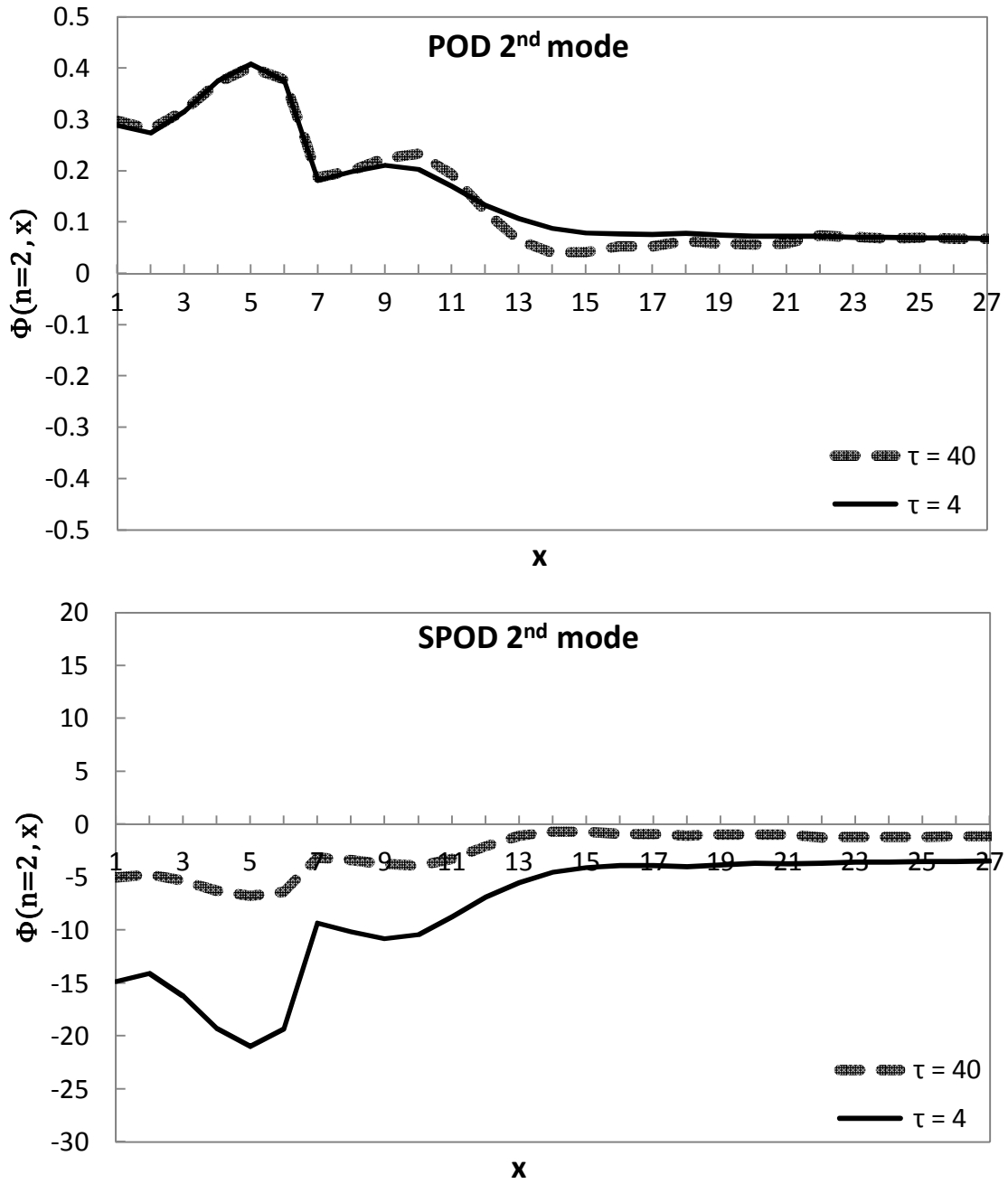
Figure 14: POD and SPOD 2nd basis eigenvectors for 90° wind, 15th row frame
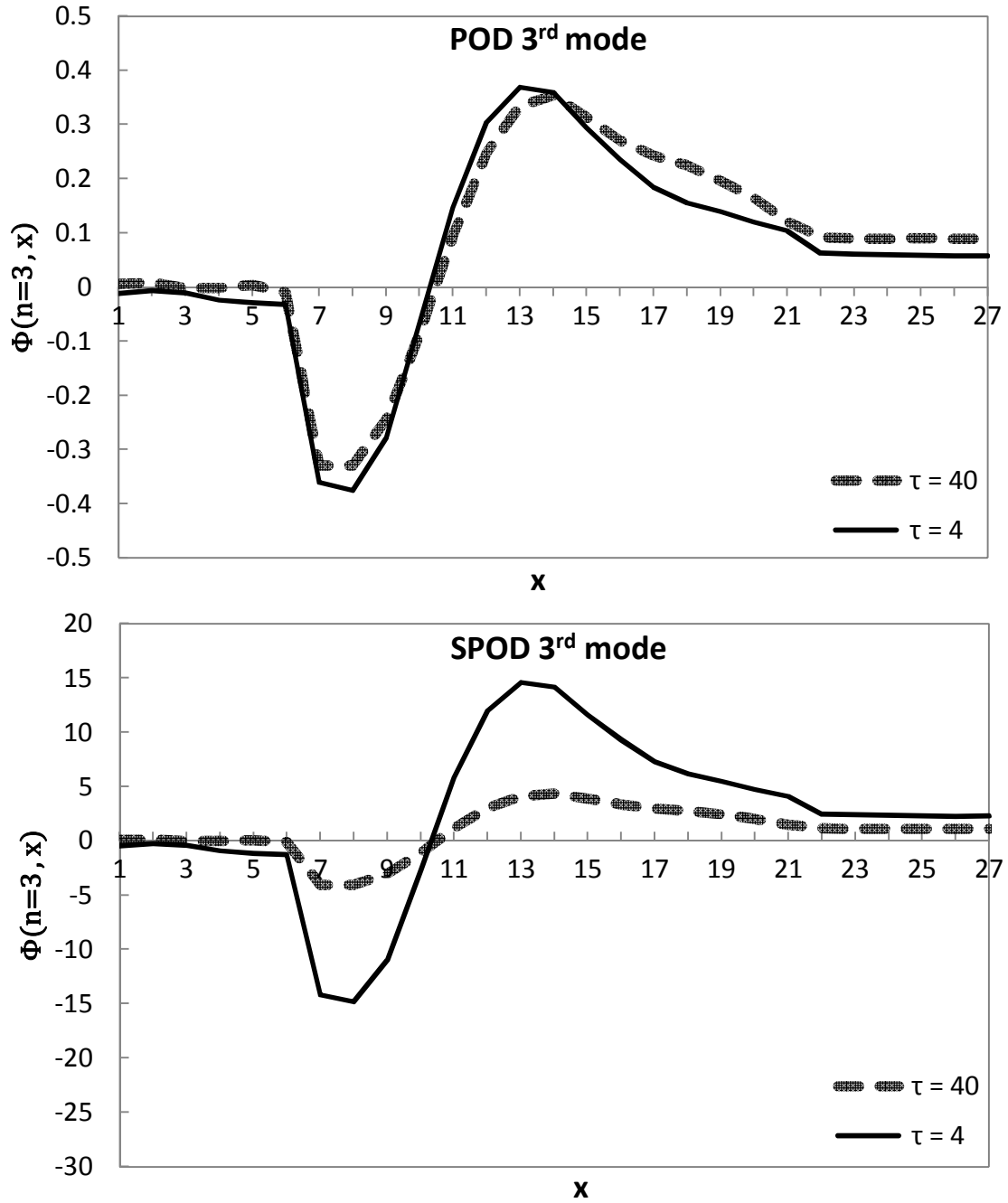
Figure 15: POD and SPOD 3rd basis eigenvectors for 90° wind, 15th row frame
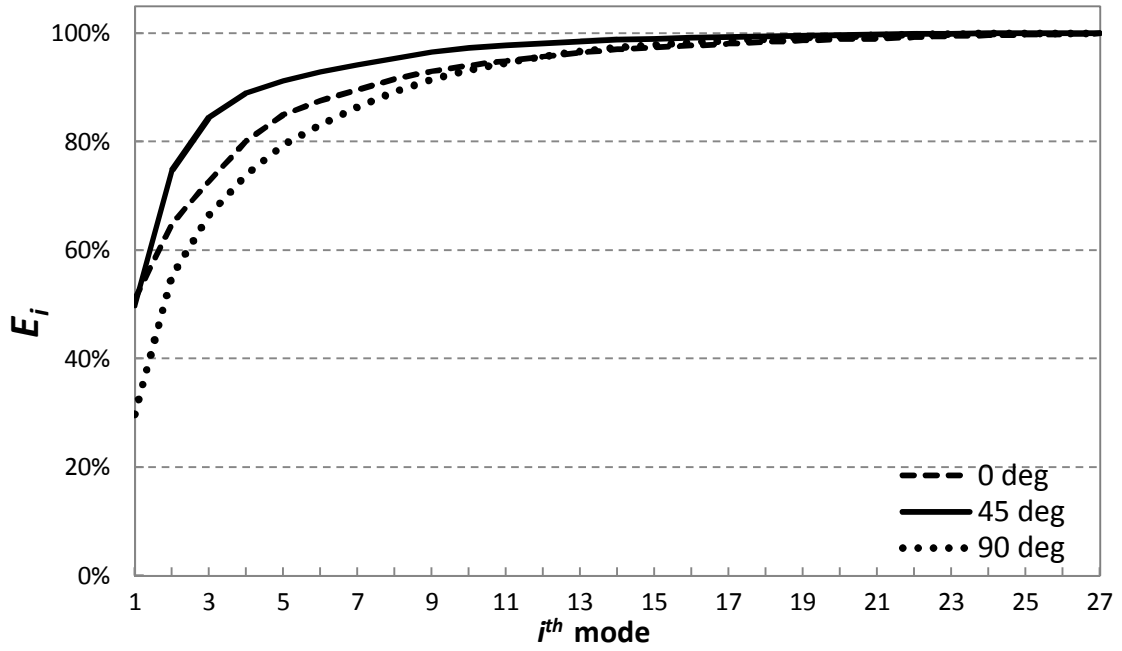
Figure 16: Effects of wind directions on relative cumulative energy of three wind directions, 1st row frame
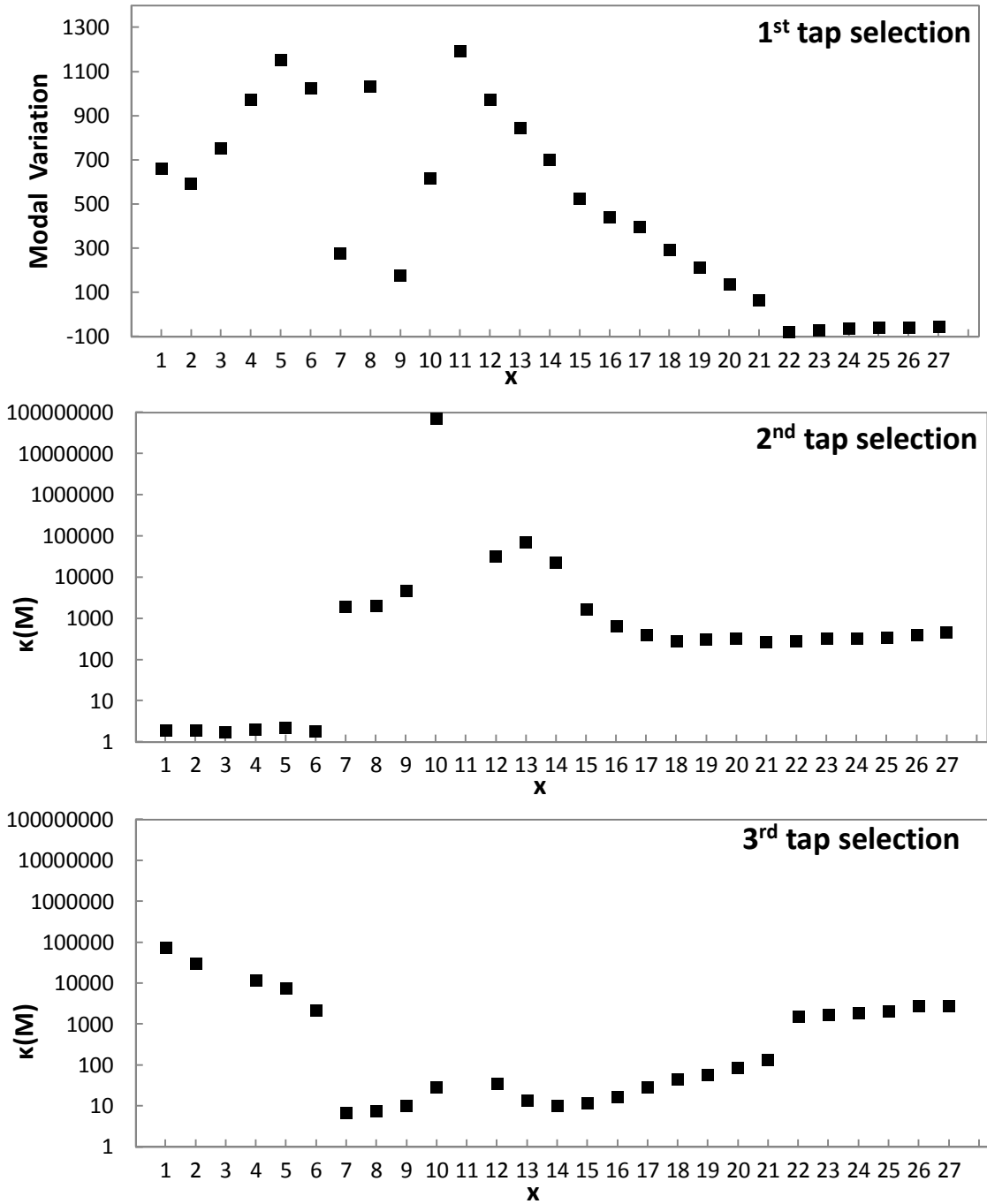
Figure 17: Modal variations used in 1st reference tap selection and condition numbers used in 2nd and 3rd reference tap selection, 90° wind, 15th row frame
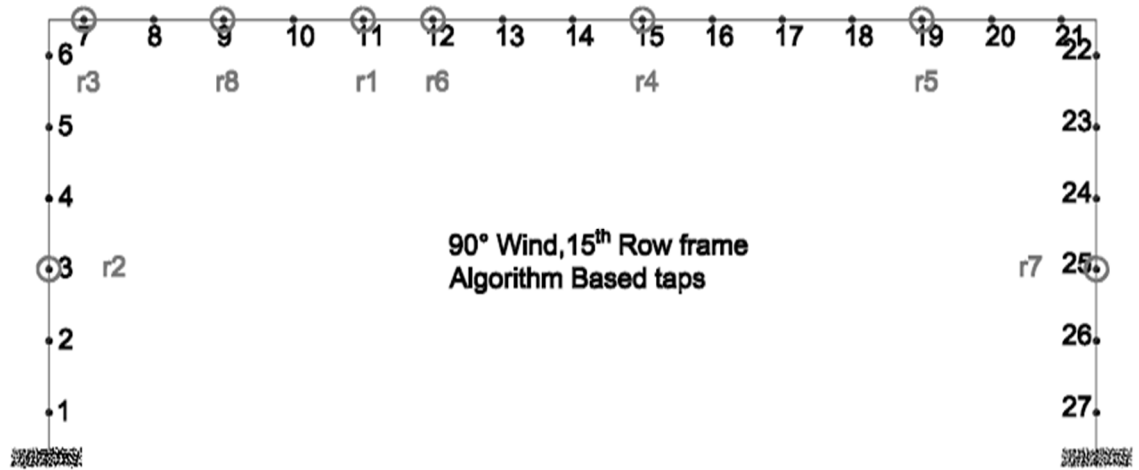
Figure 18: First 8 algorithm-selected reference taps, 90° wind, 15th row frame
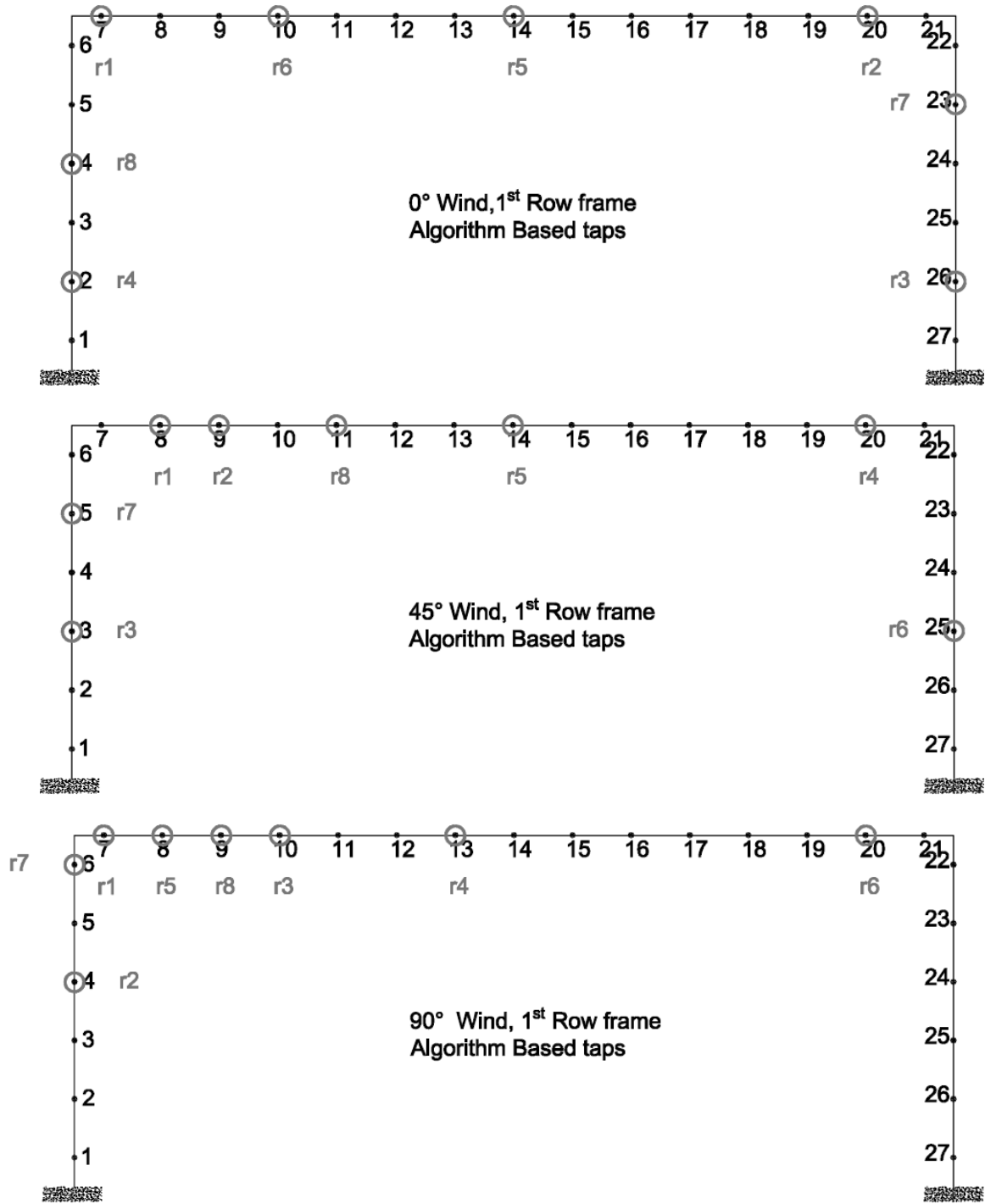
Figure 19: Effect of wind directions on first 8 algorithm-based reference taps, 1st row frame
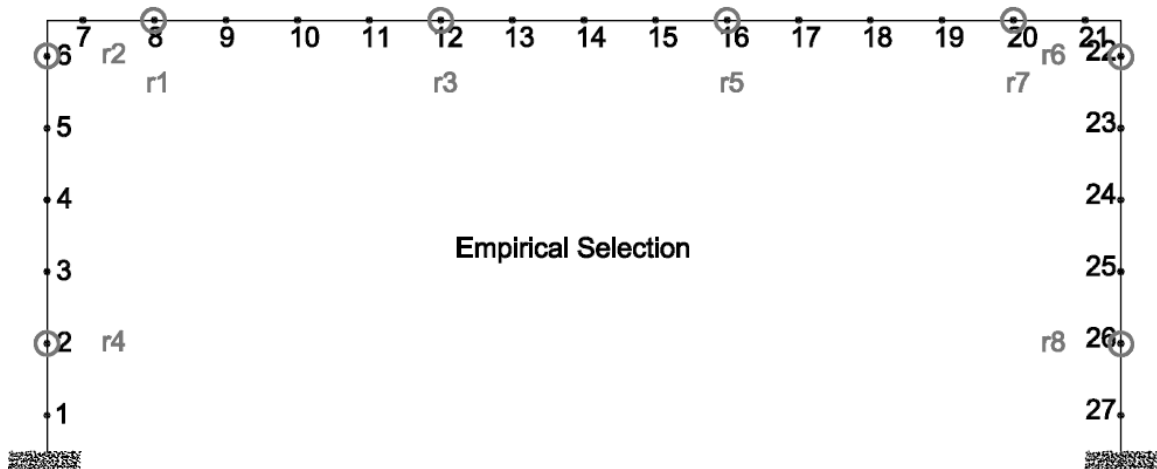
Figure 20: First 8 empirically selected reference taps for analyses of 1st and 15th row frames
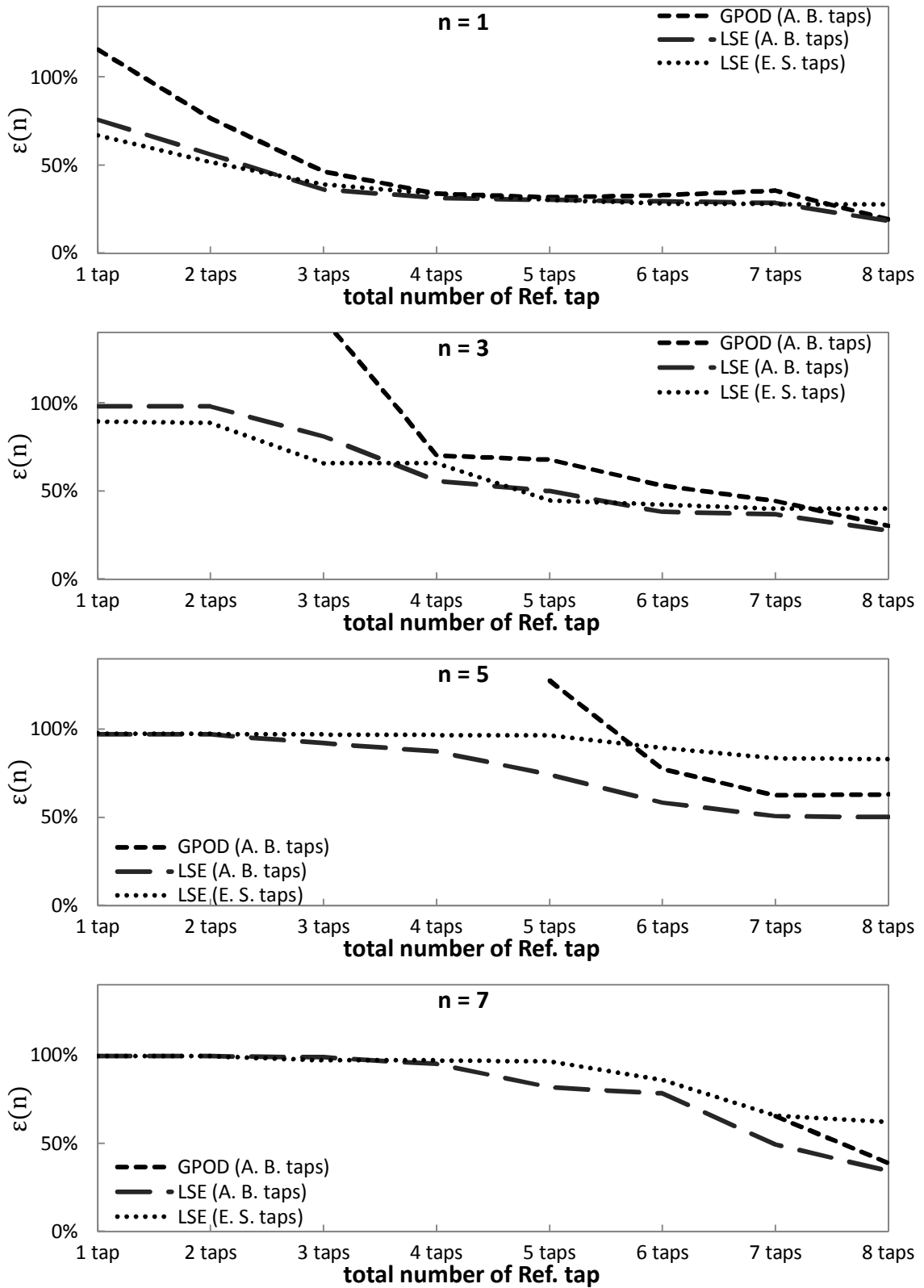
Figure 21: Effects of number of reference taps on modal residual errors, modes $n = 1, 3, 5$ and 7, 90° wind, 15th row frame

Figure 22: Effects of number of reference taps on standard deviation of reconstructed principal coordinates, modes $n = 1, 3, 5$ and 7, 90° wind, 15th row frame
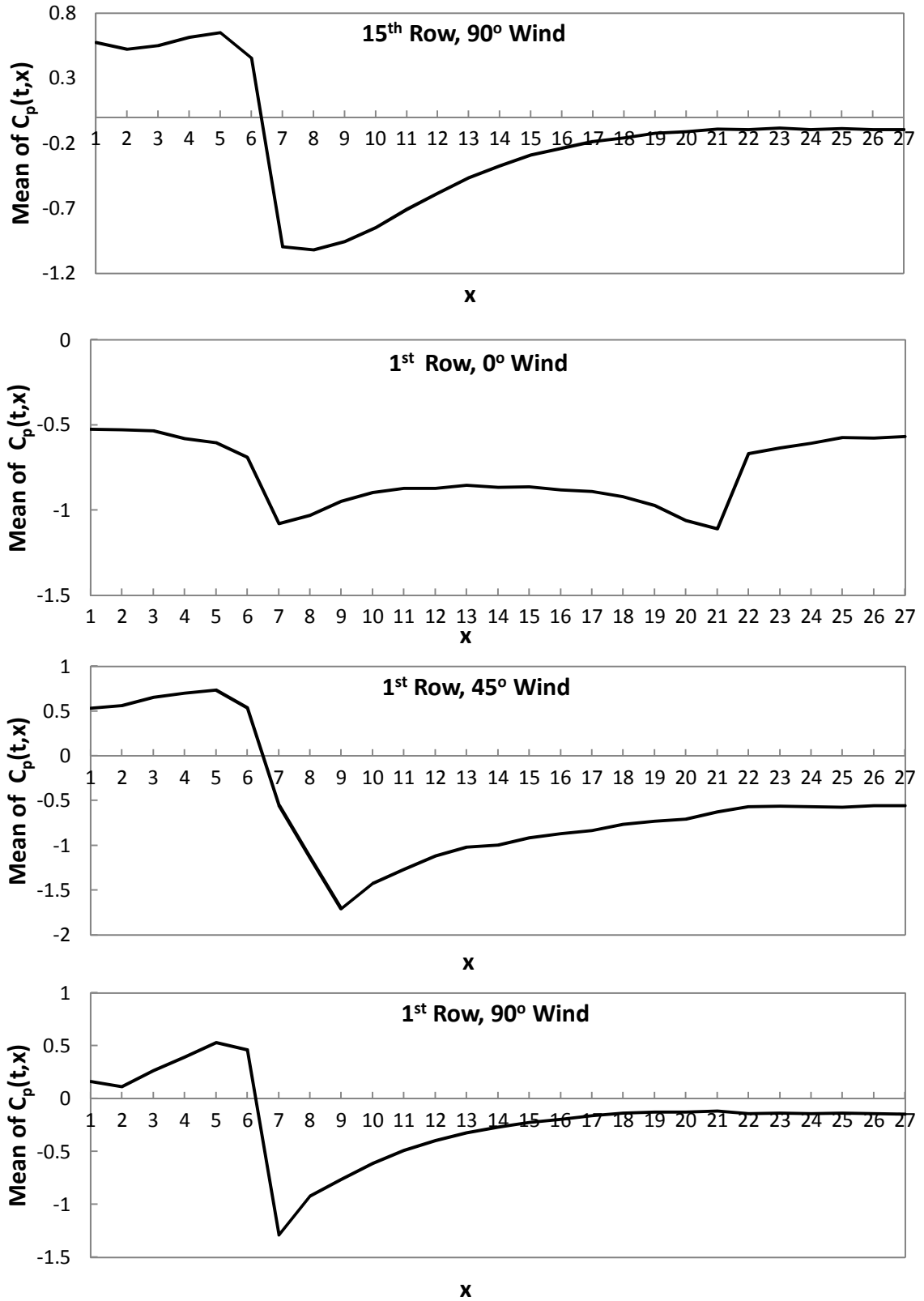
Figure 23: Means of wind-induced pressure
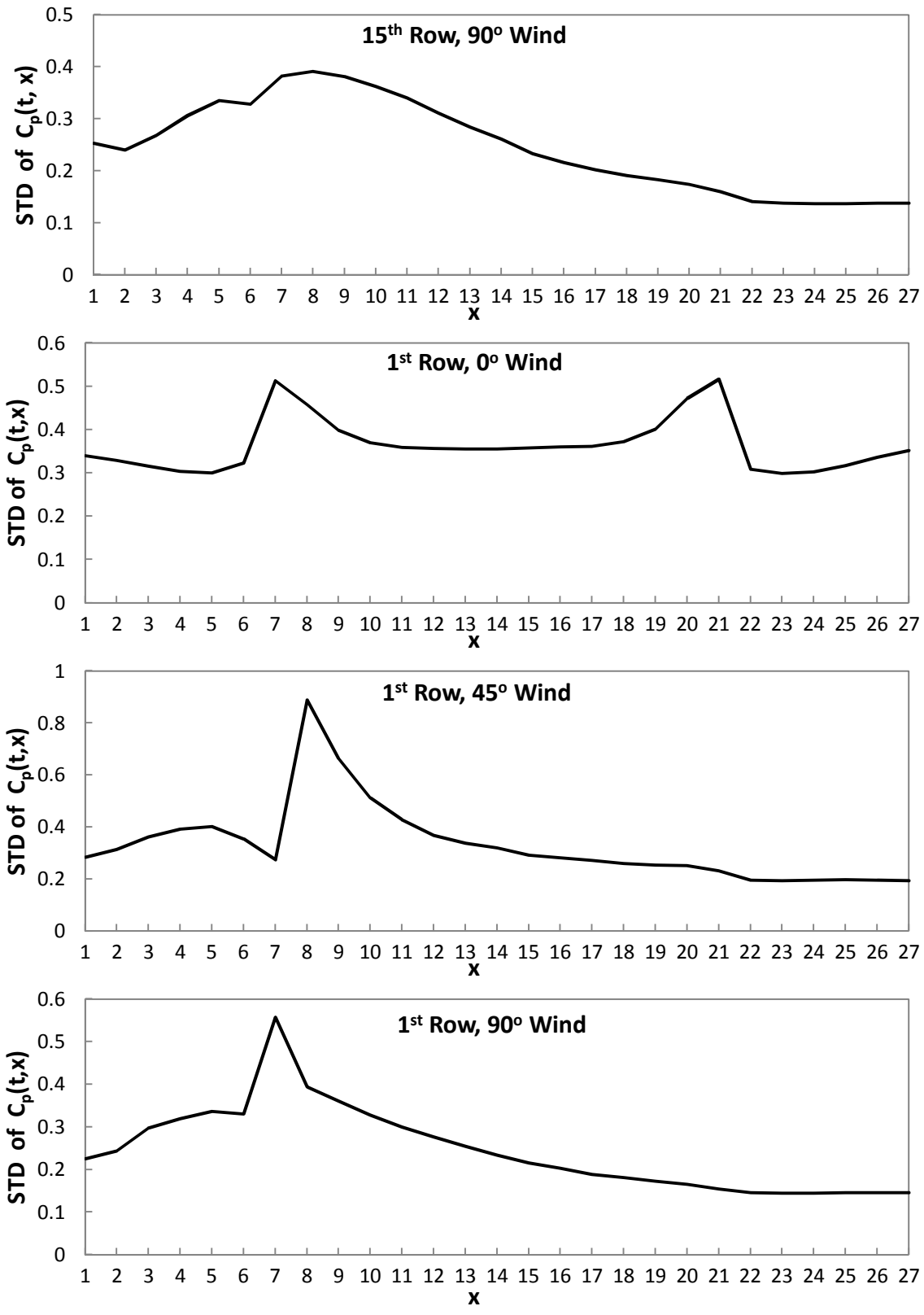
Figure 24: Standard deviations of wind-induced pressure
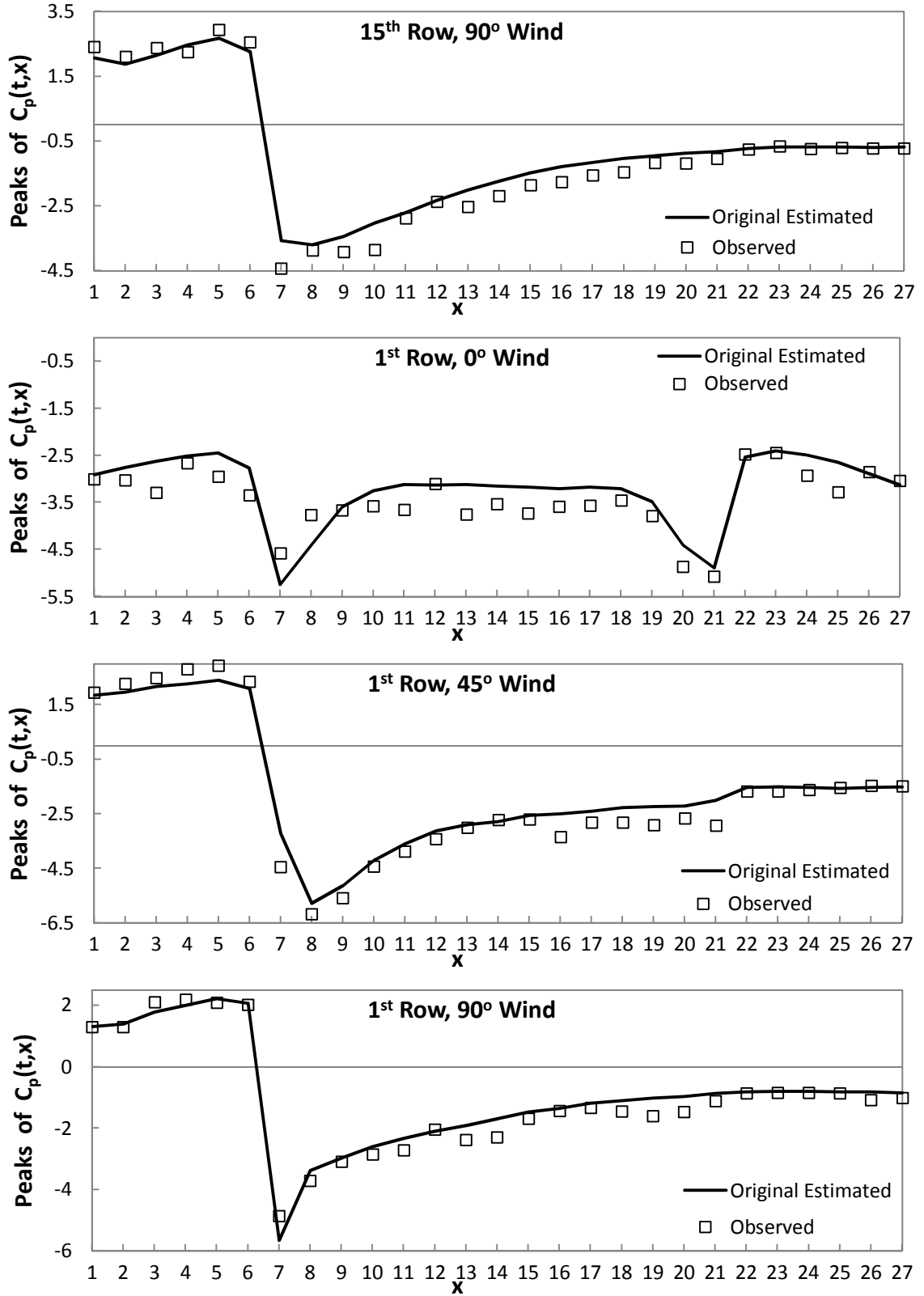
Figure 25: Observed pressure and estimated peaks of wind-induced pressure
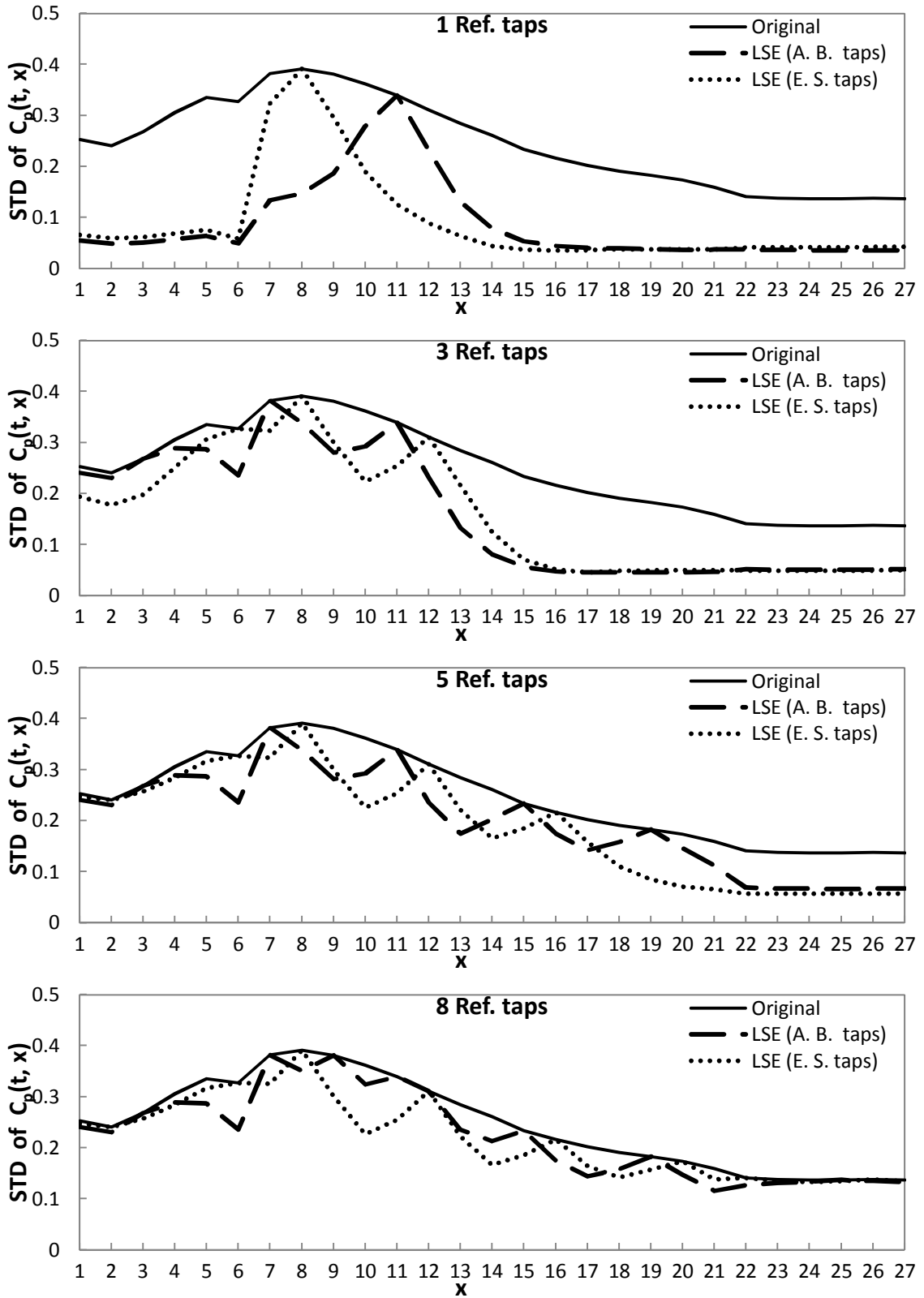
Figure 26: Effects of reference tap selection and number of taps on pressure standard deviation, of 90° wind, 15th row frame
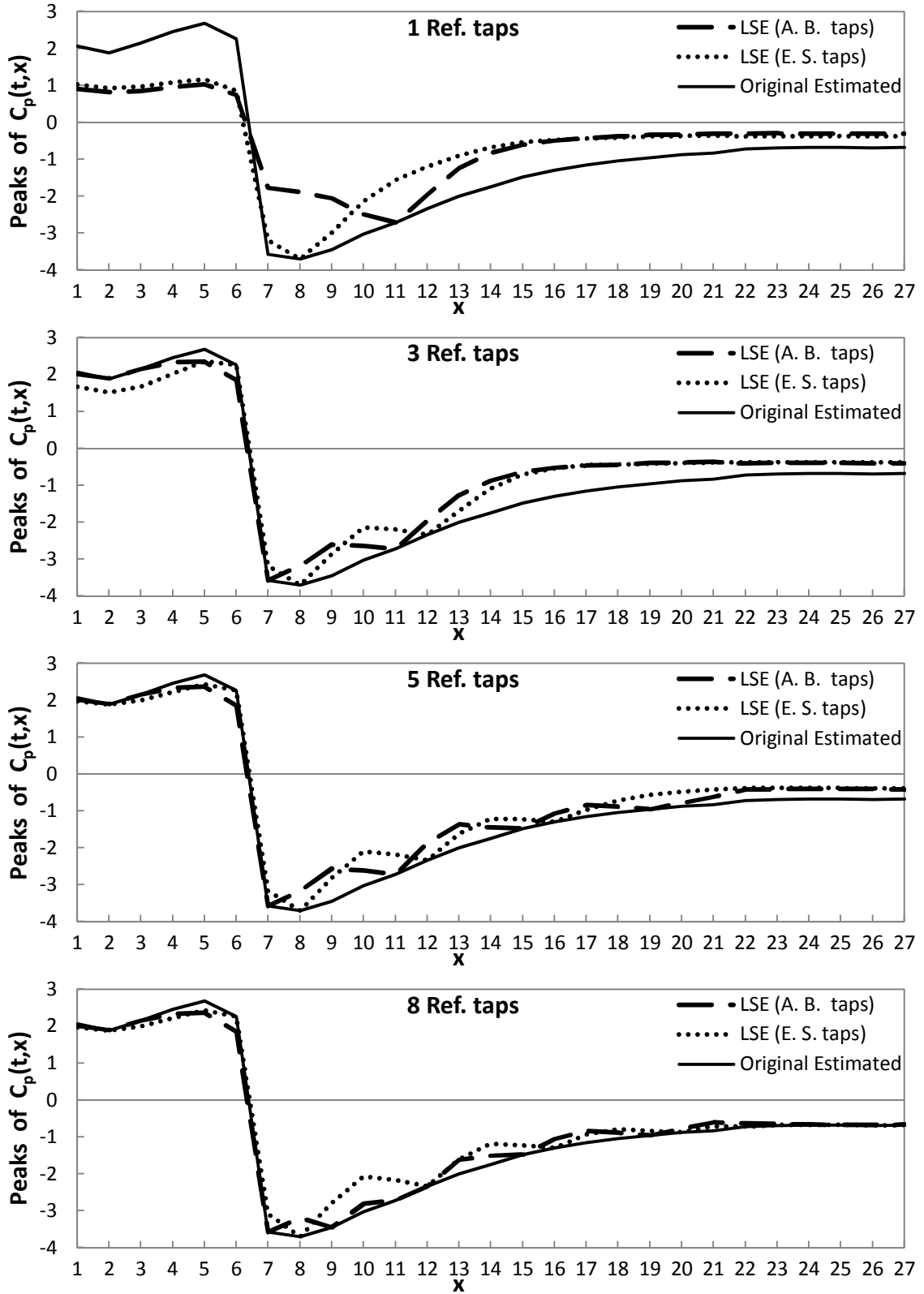
Figure 27: Effects of reference tap selection and number of taps on estimated pressure peaks, 90° wind, 15th row frame
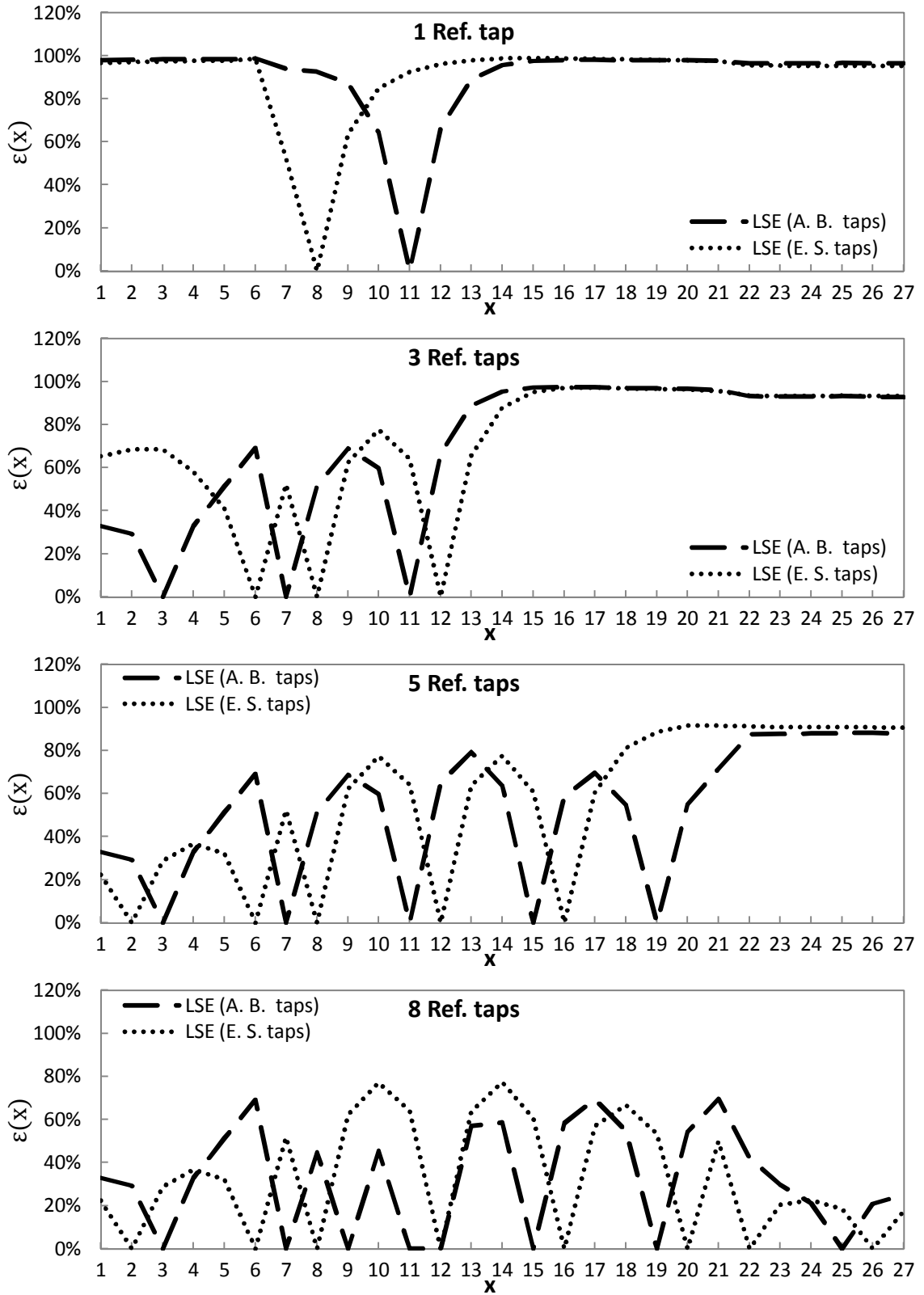
Figure 28: Effects of reference tap selection and number of taps on residual errors of extrapolated pressure, 90° wind, 15th row frame
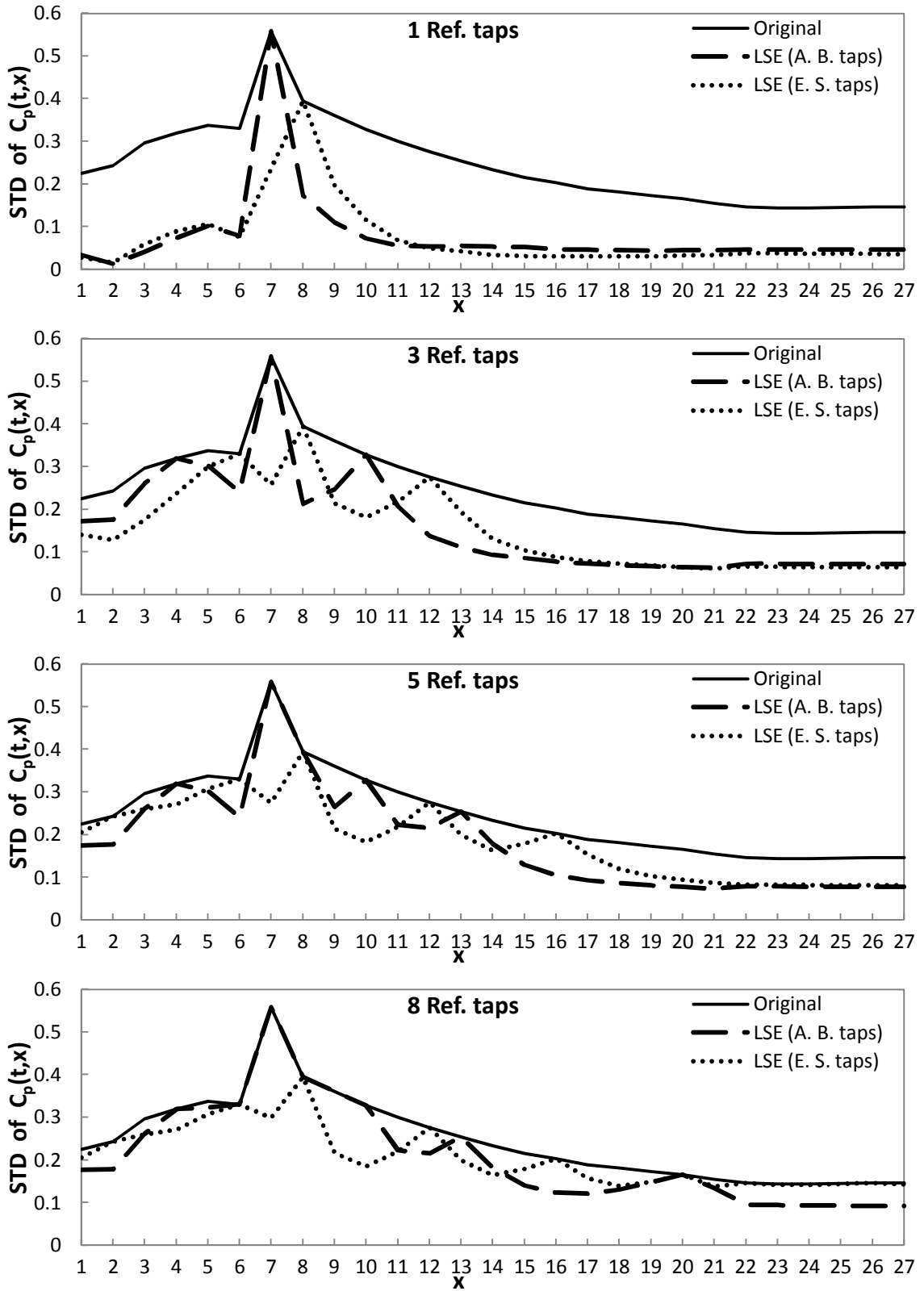
Figure 29: Effects of reference tap selection and number of taps on pressure standard deviation, 90° wind, 1st row frame
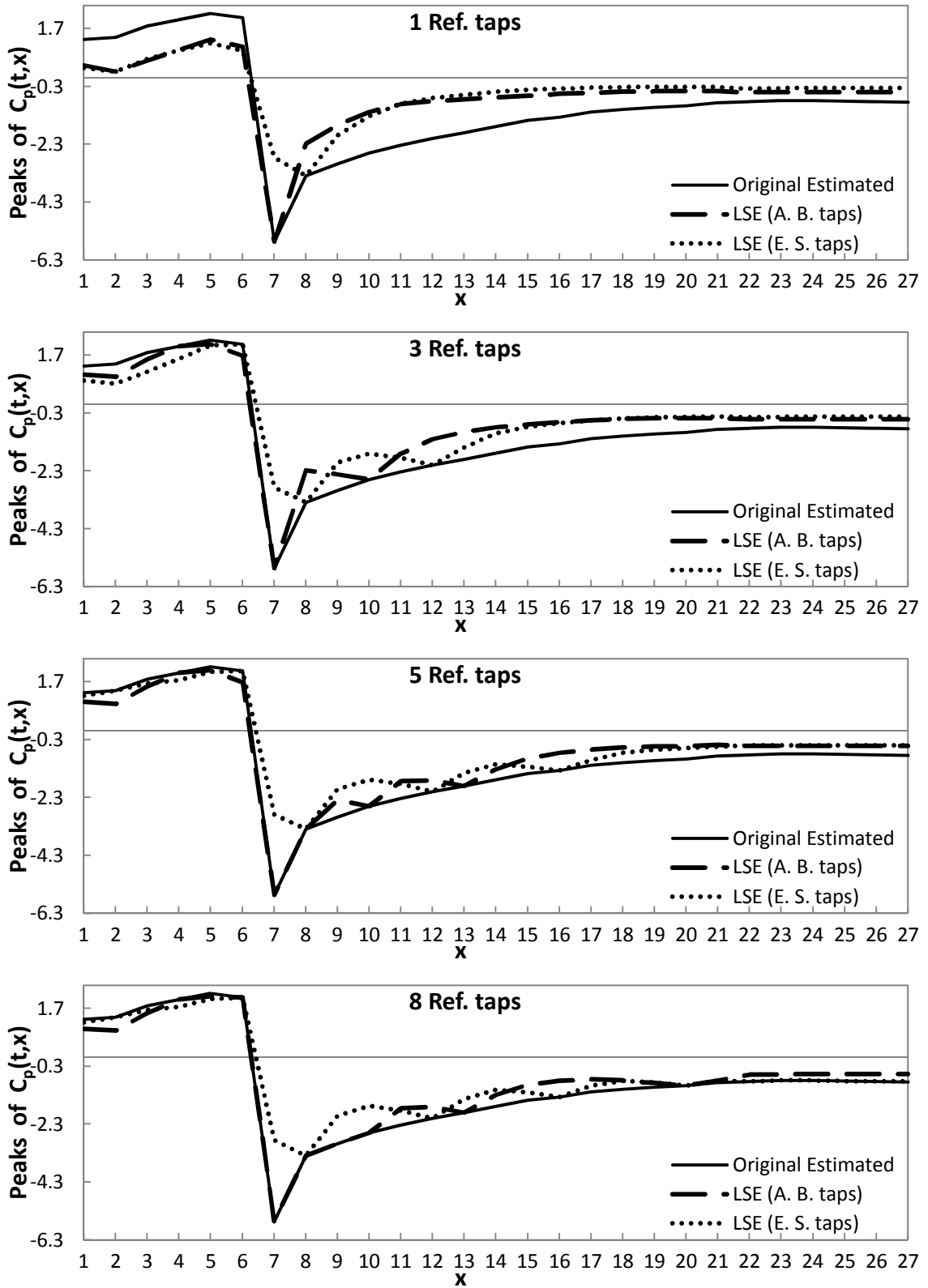
Figure 30: Effects of reference tap selection and number of taps on estimated pressure peaks, 90° wind, 1ˢᵗ row frame
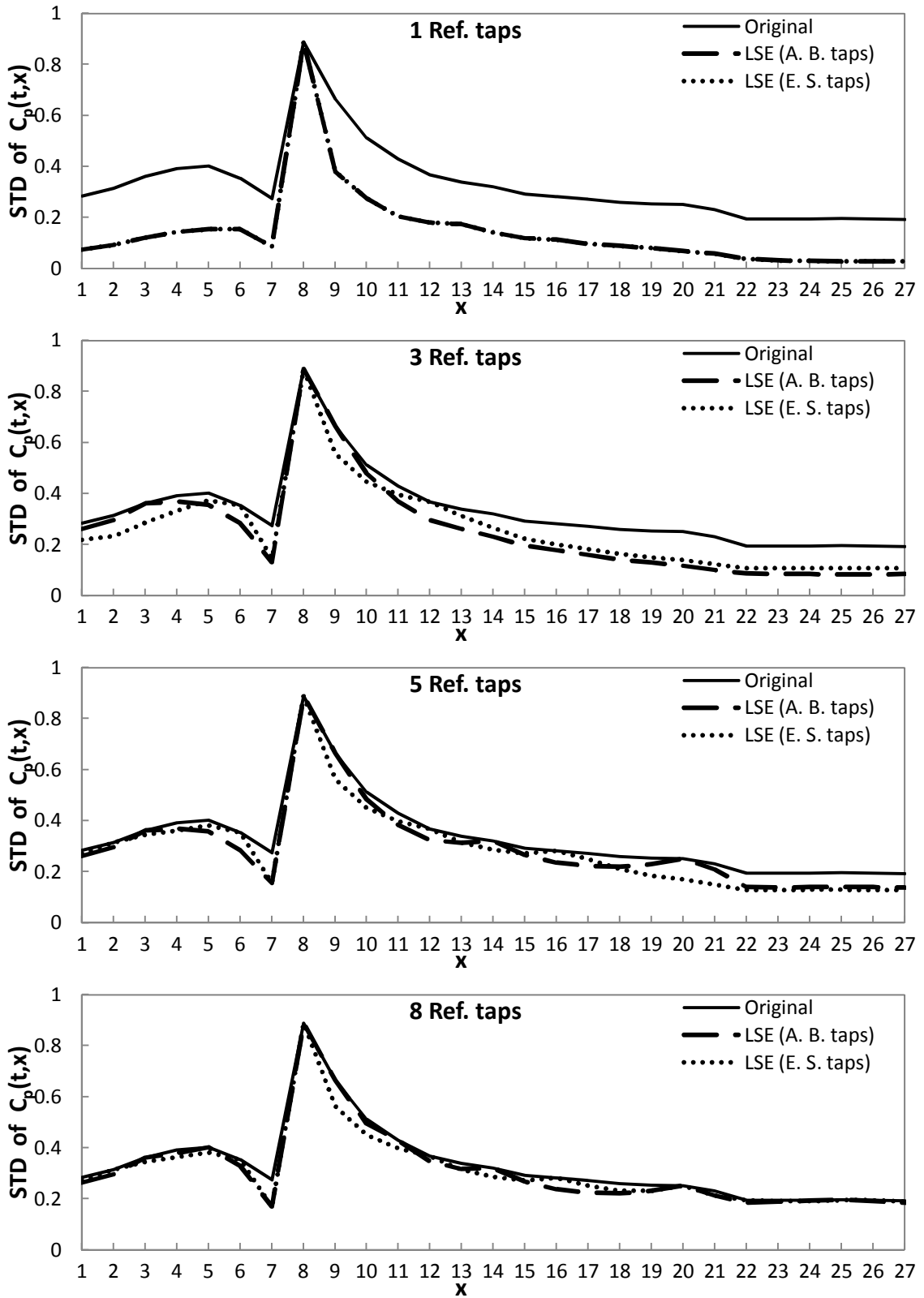
Figure 31: Effects of reference tap selection and number of taps on pressure standard deviation, 45° wind, 1st row frame
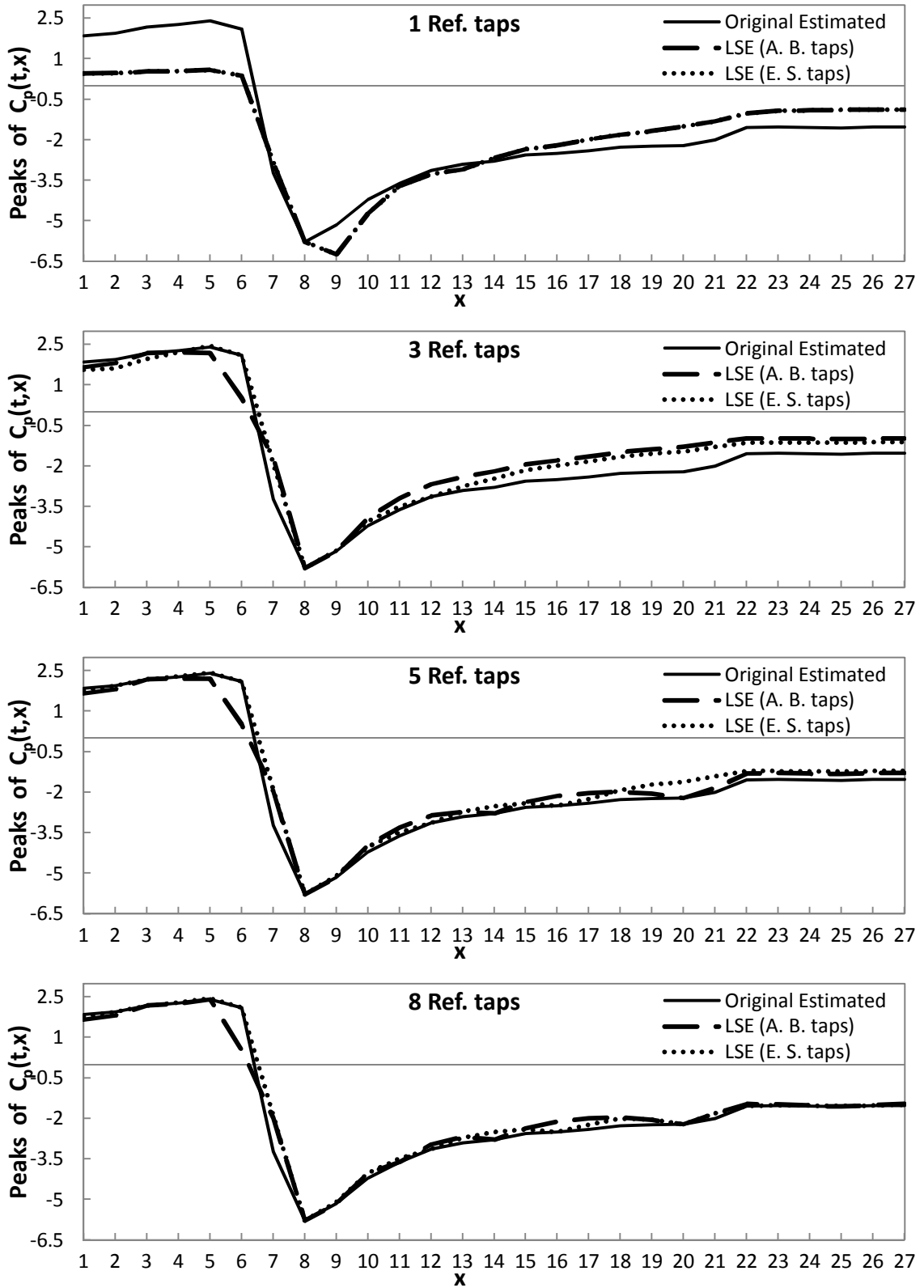
Figure 32: Effects of reference tap selection and number of taps on estimated pressure peaks, 45° wind, 1st row frame
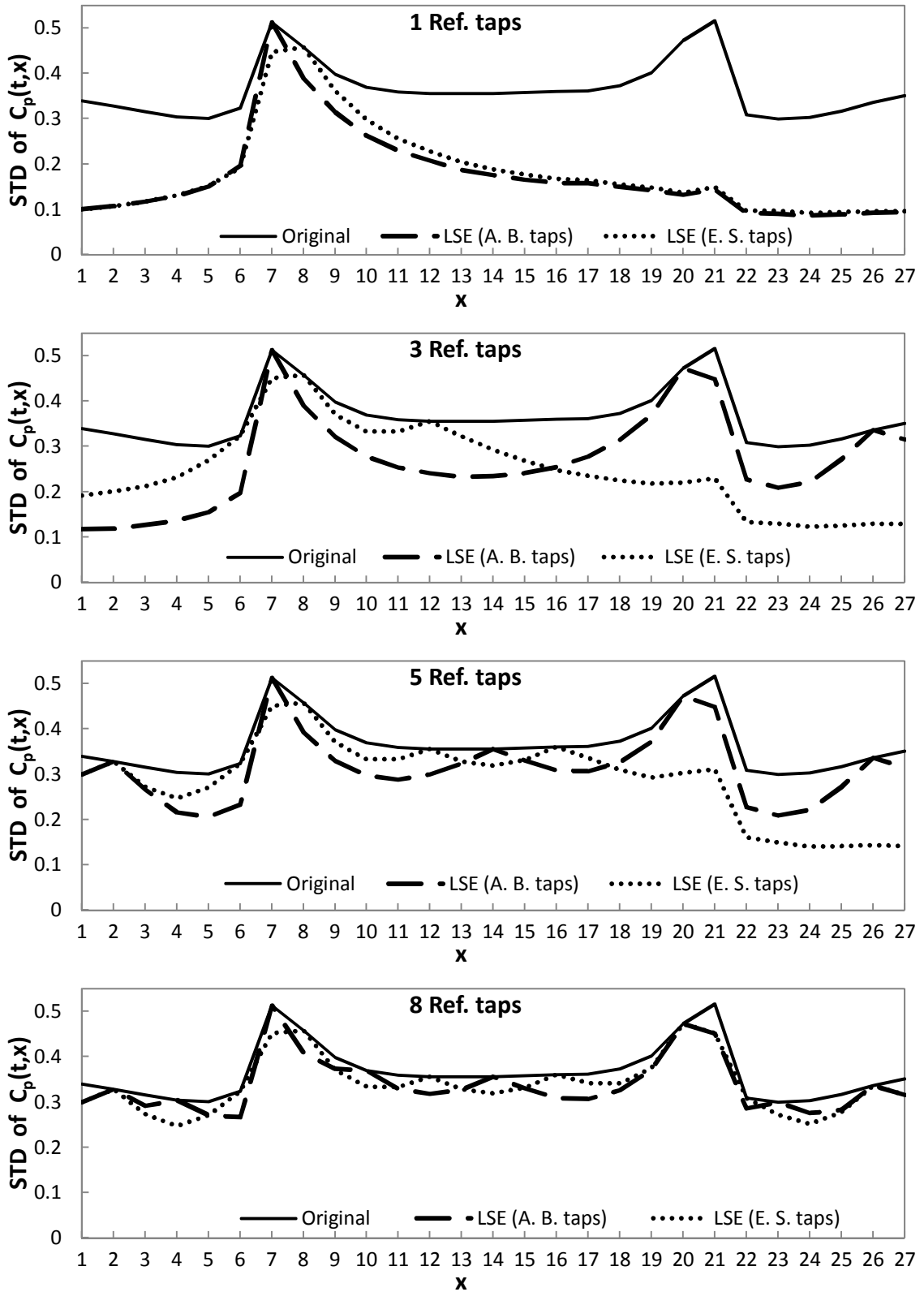
Figure 33: Effects of reference tap selection and number of taps on pressure standard deviation, $0°$ wind, 1st row frame
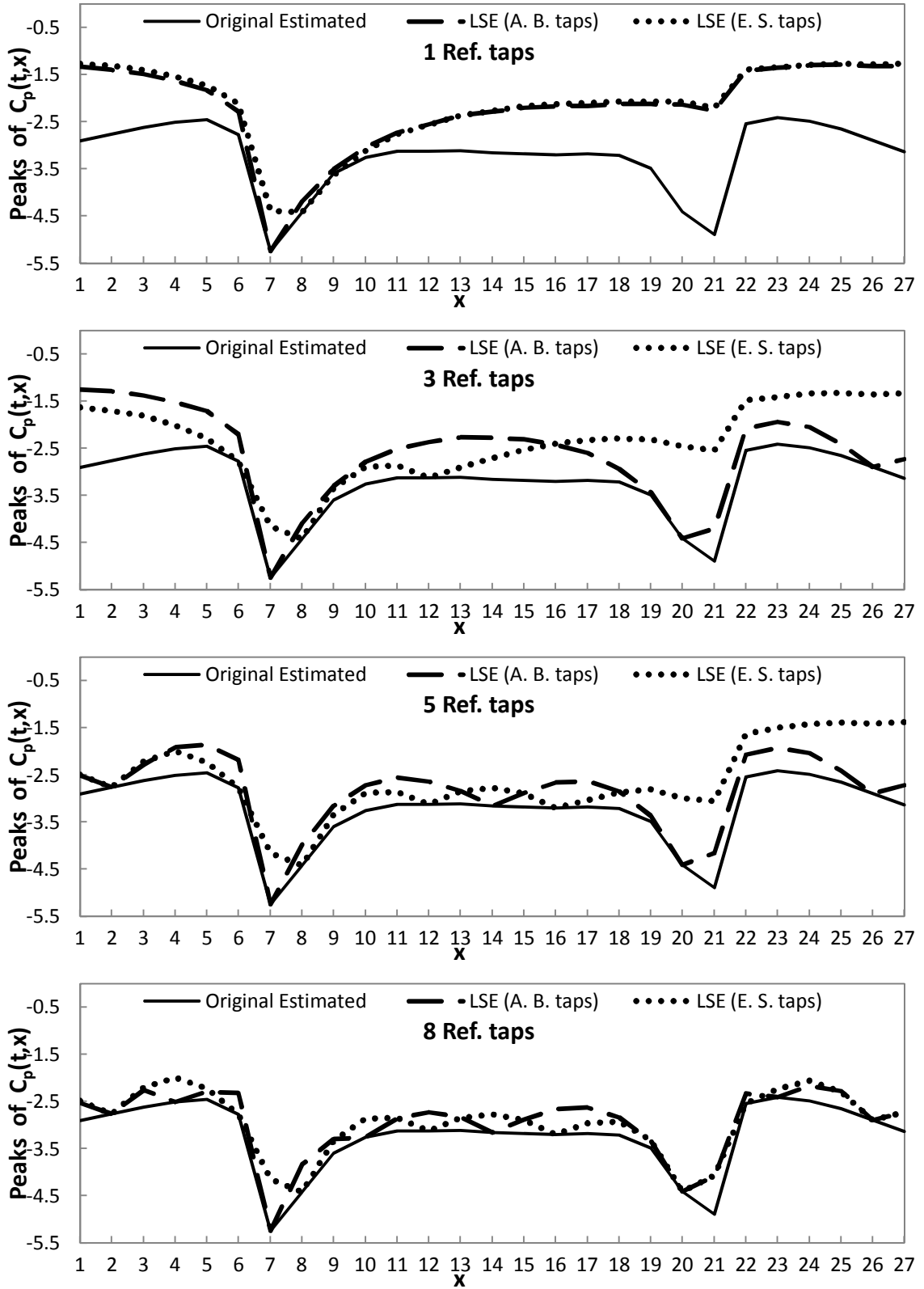
Figure 34: Effects of reference tap selection and number of taps on estimated pressure peaks, 0° wind, 1st row frame
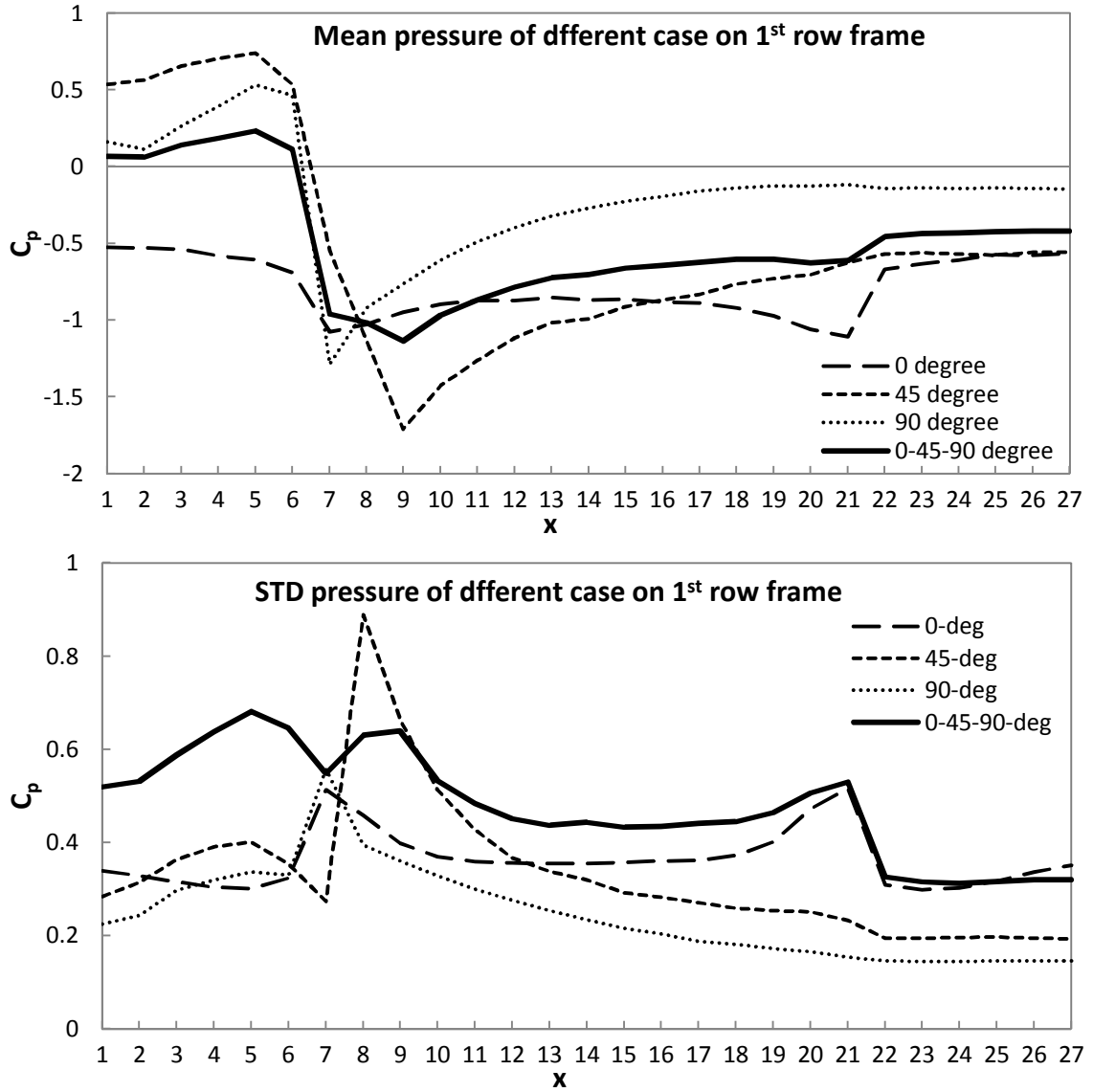
Figure 35: Mean and standard deviation of stationary (dashed lines) and non-stationary (solid line) cases
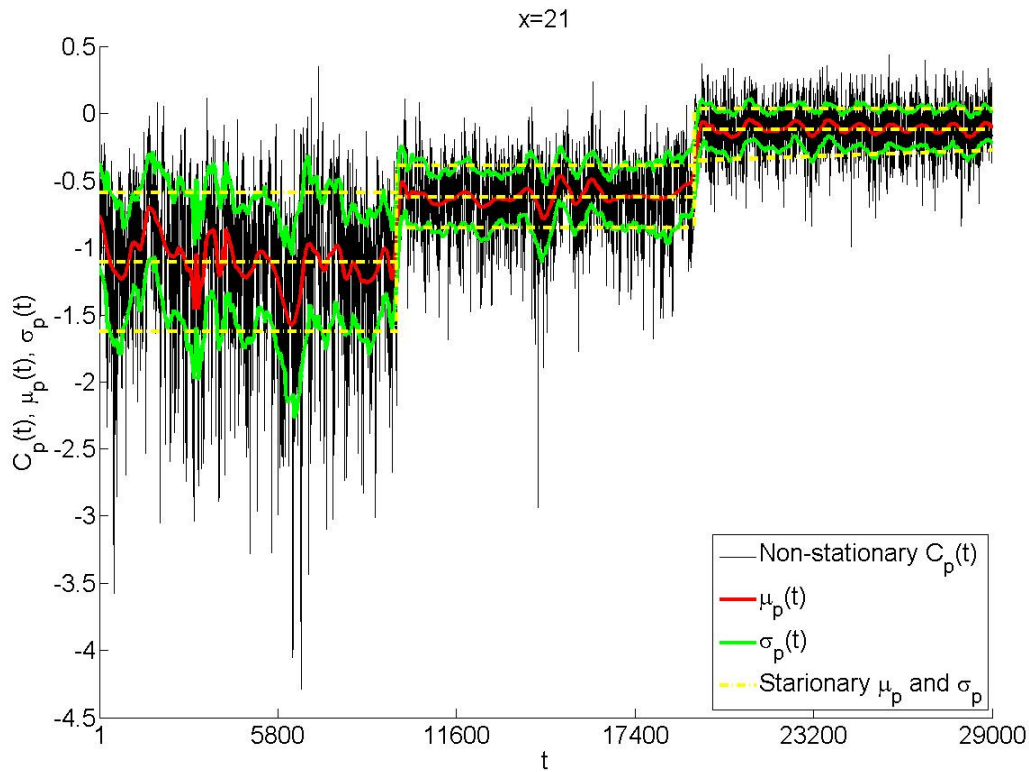
Figure 36: Time-varying mean and standard deviation envelopes, stationary mean and stationary standard deviation envelopes, and pressure time series of non-stationary (0°-45°-90°) wind, 1st row frame.
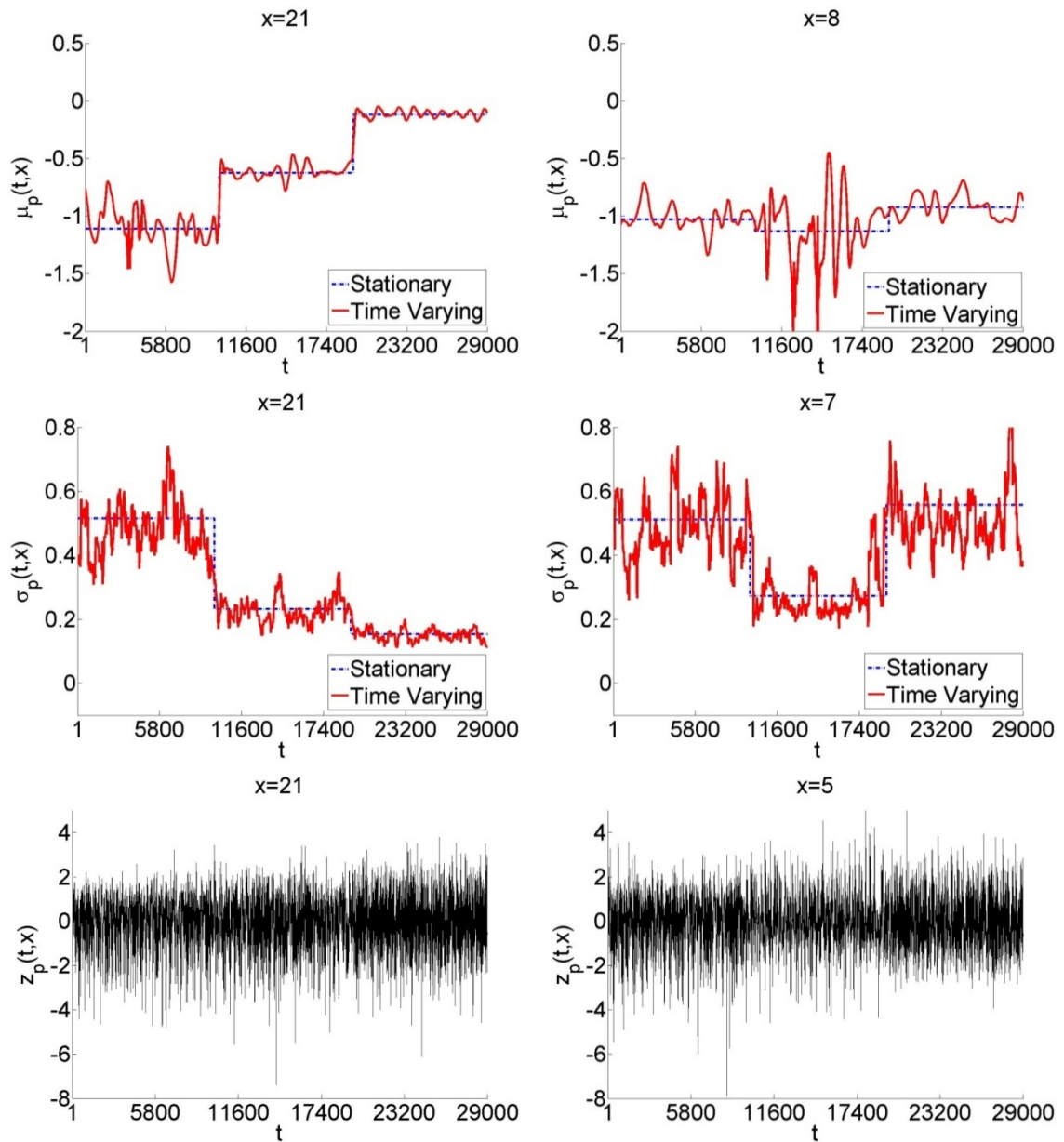
Figure 37: Time-varying mean at taps $x = 21$ and 8 (first row), time-varying standard deviation at taps $x = 21$ and 7 (second row), and normalized fluctuation at taps $x = 21$ and 5 (third row)
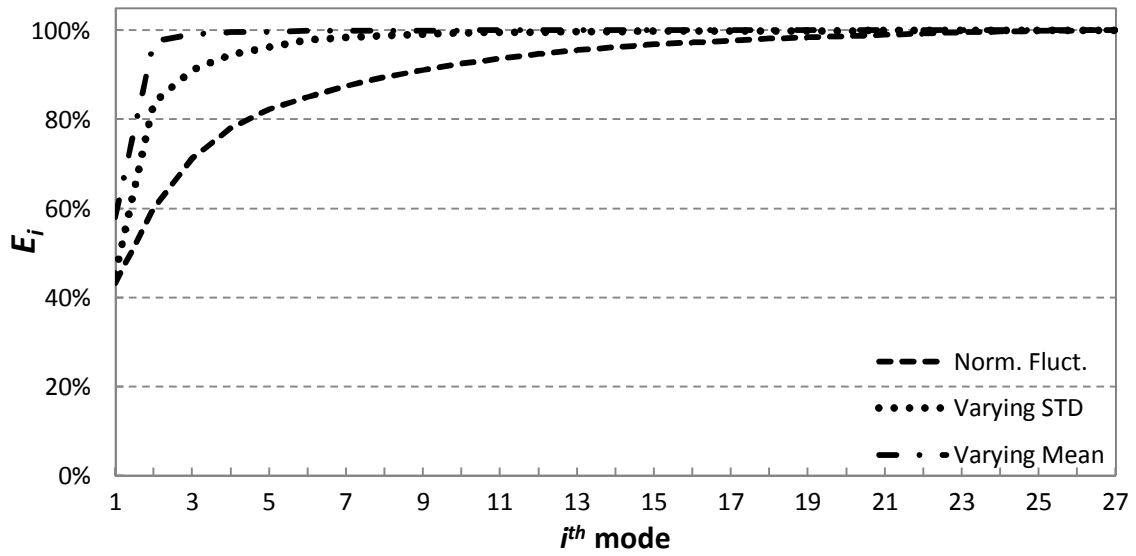
Figure 38: Cumulative energy of three non-stationary elements
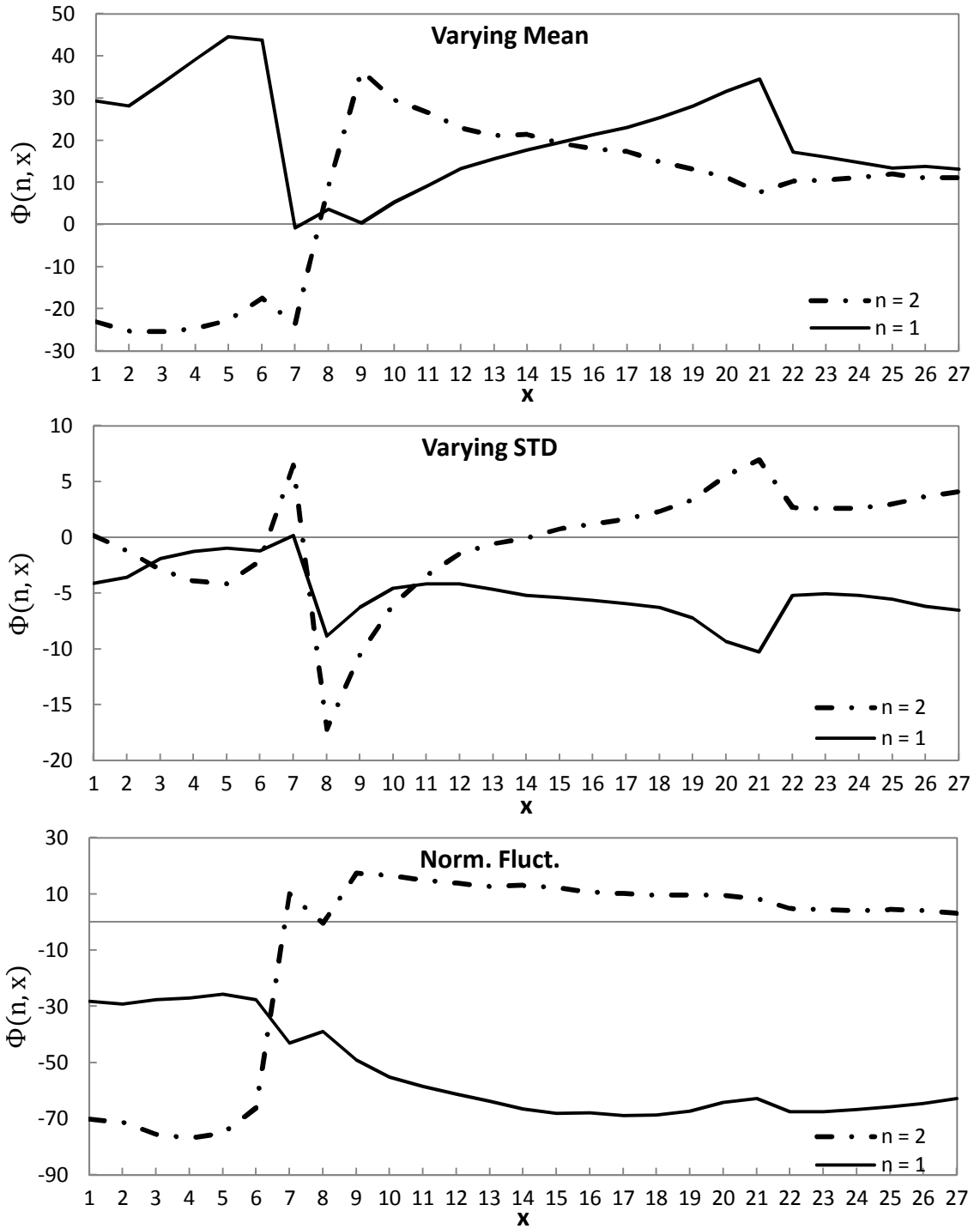
Figure 39: First two SPOD modal shapes of three non-stationary elements
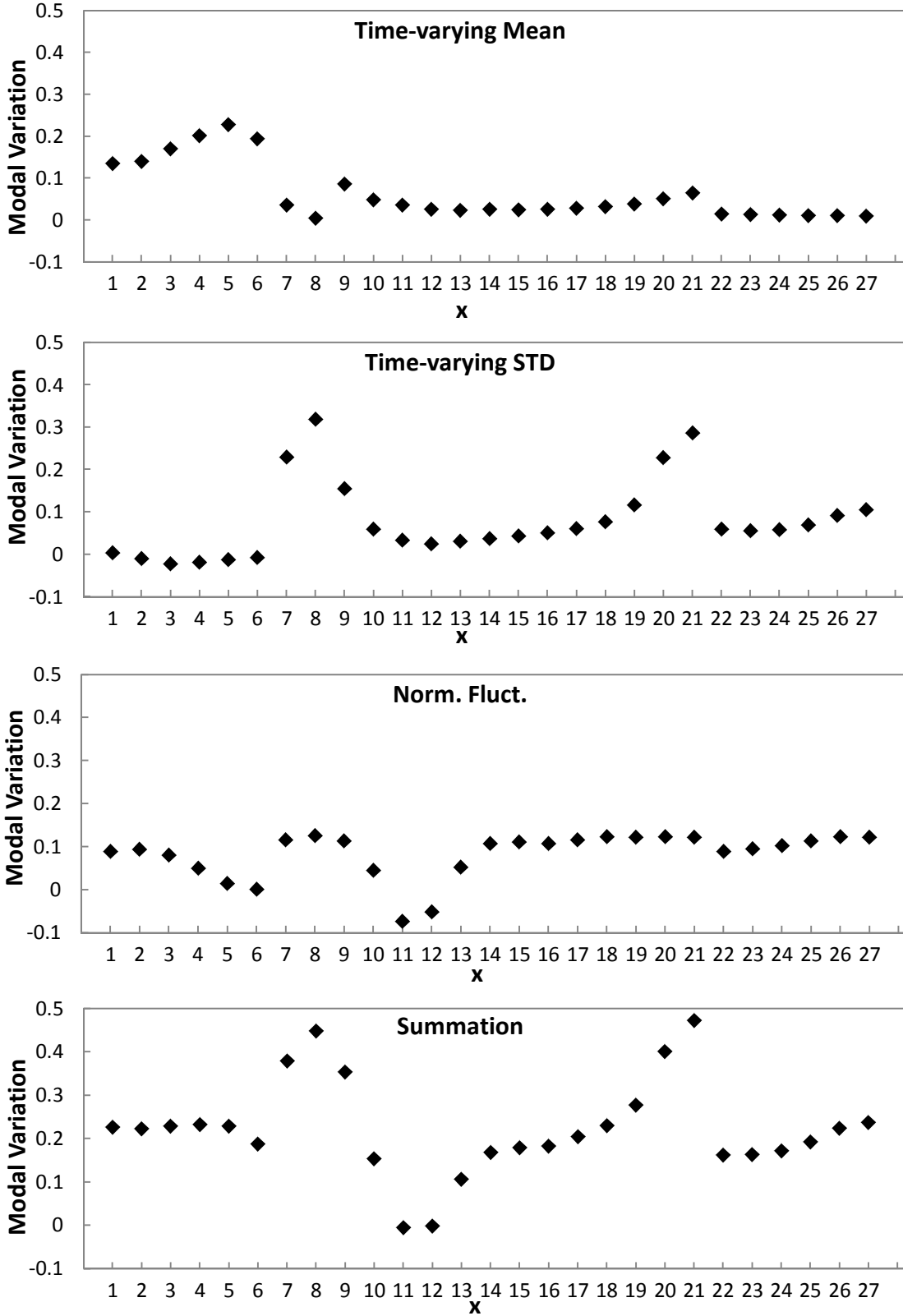
Figure 40: Modal variations of each non-stationary elements and the summation on candidate locations for 1st reference tap
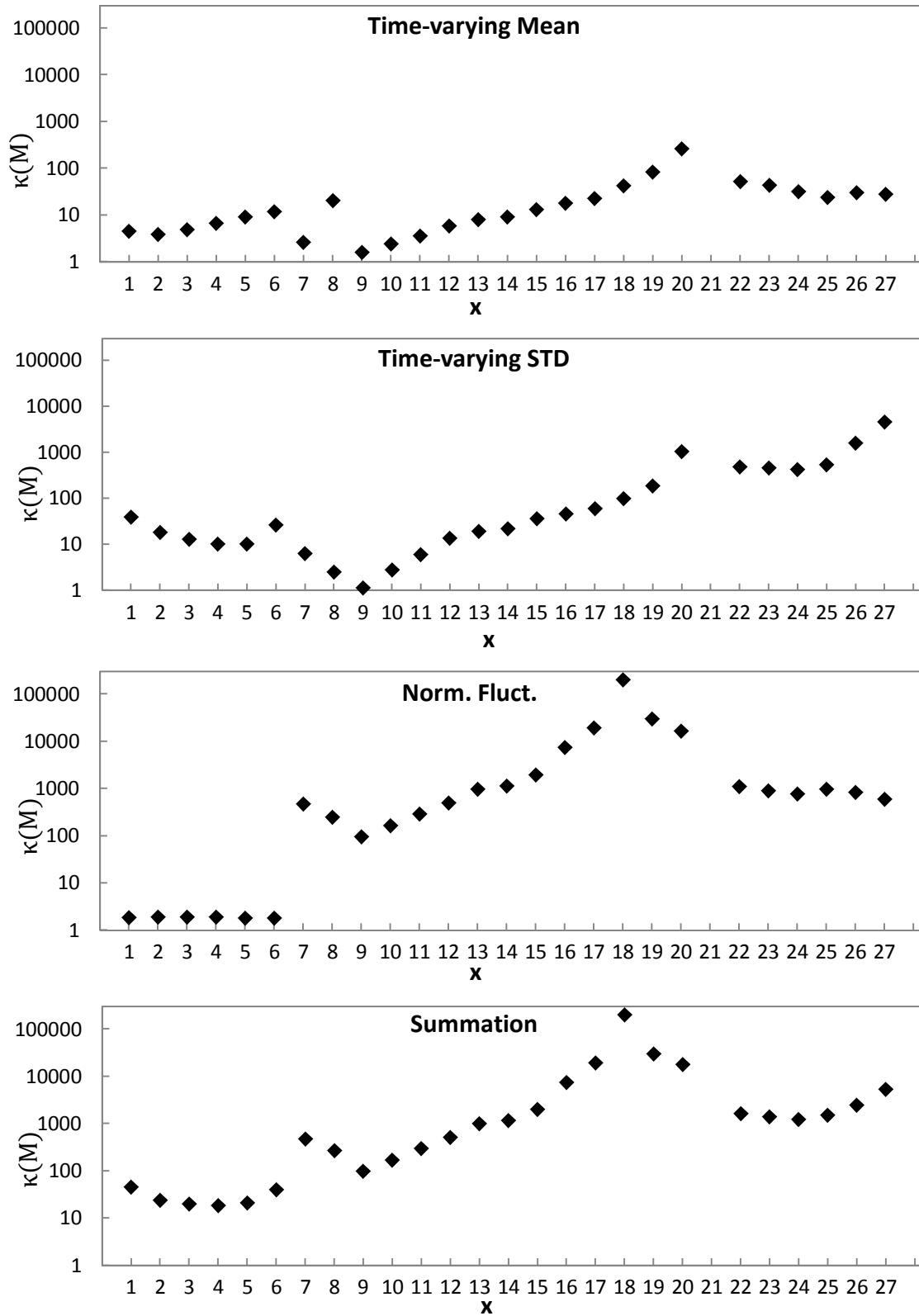
Figure 41: Condition number of each non-stationary element and the summation on candidate locations for 2nd reference tap
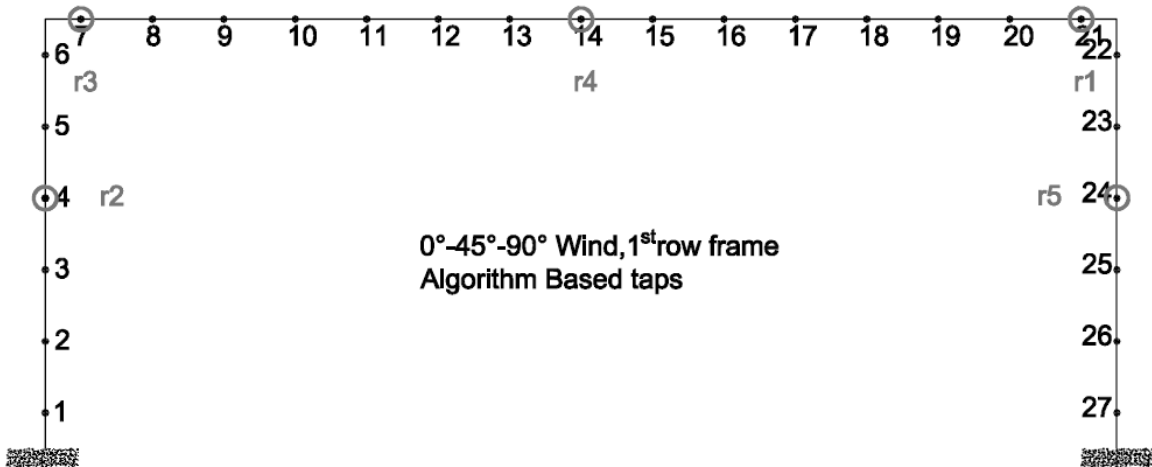
Figure 42: First 5 chosen reference taps on 1st row frame under non-stationary wind
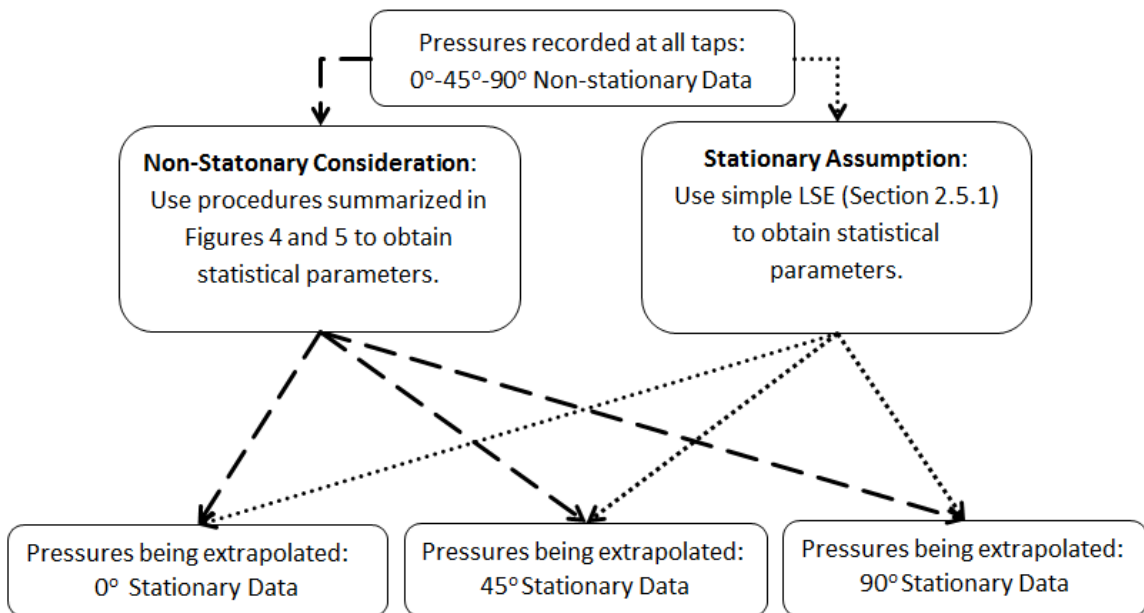
Figure 43: Non-stationary pressure extrapolations using different methods
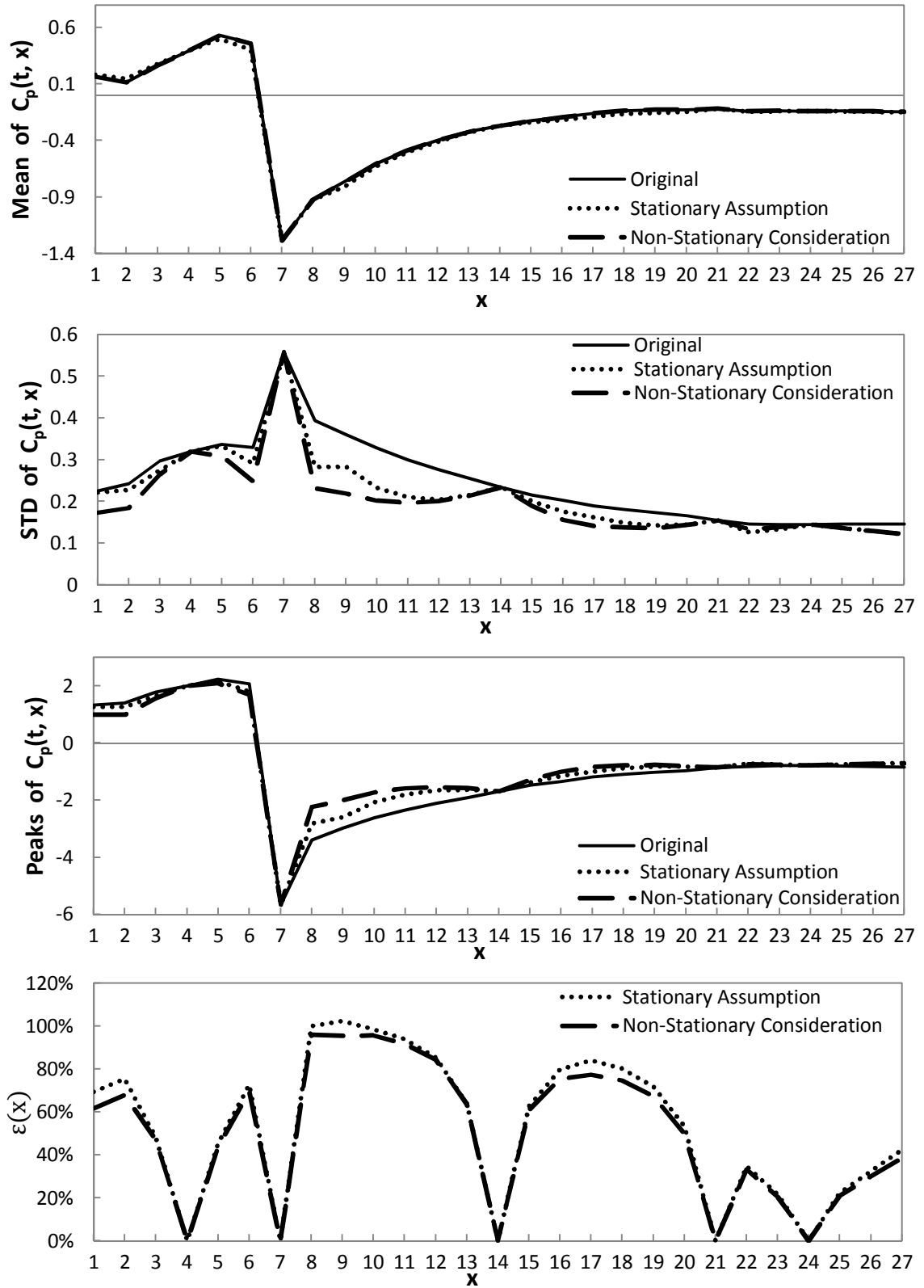
Figure 44: Effects of extrapolation methods on means, standard deviations, estimated peaks and residual errors, 90° wind, 1st row
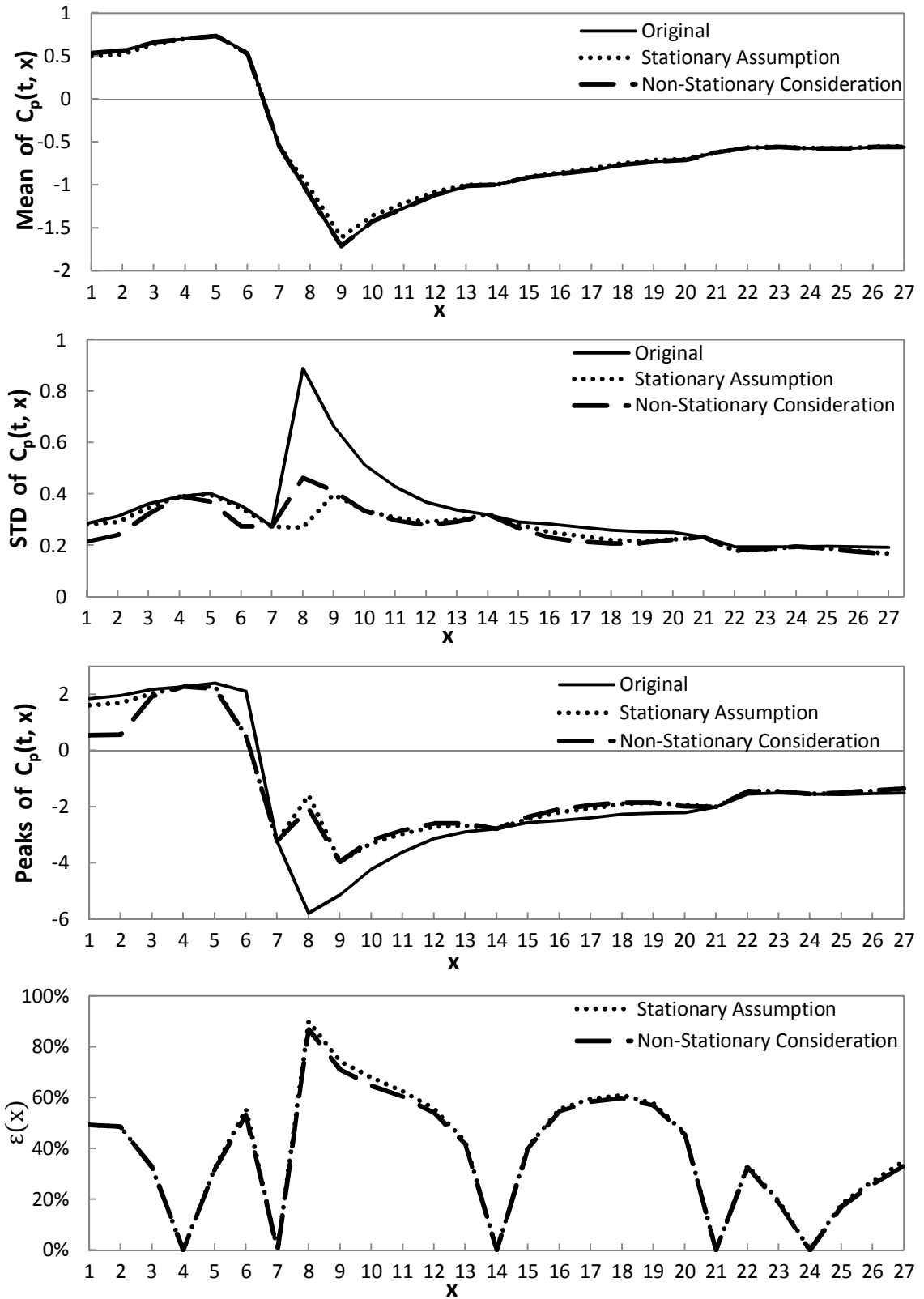
Figure 45: Effects of extrapolation methods on means, standard deviations, estimated peaks and residual errors, 45° wind, 1st row
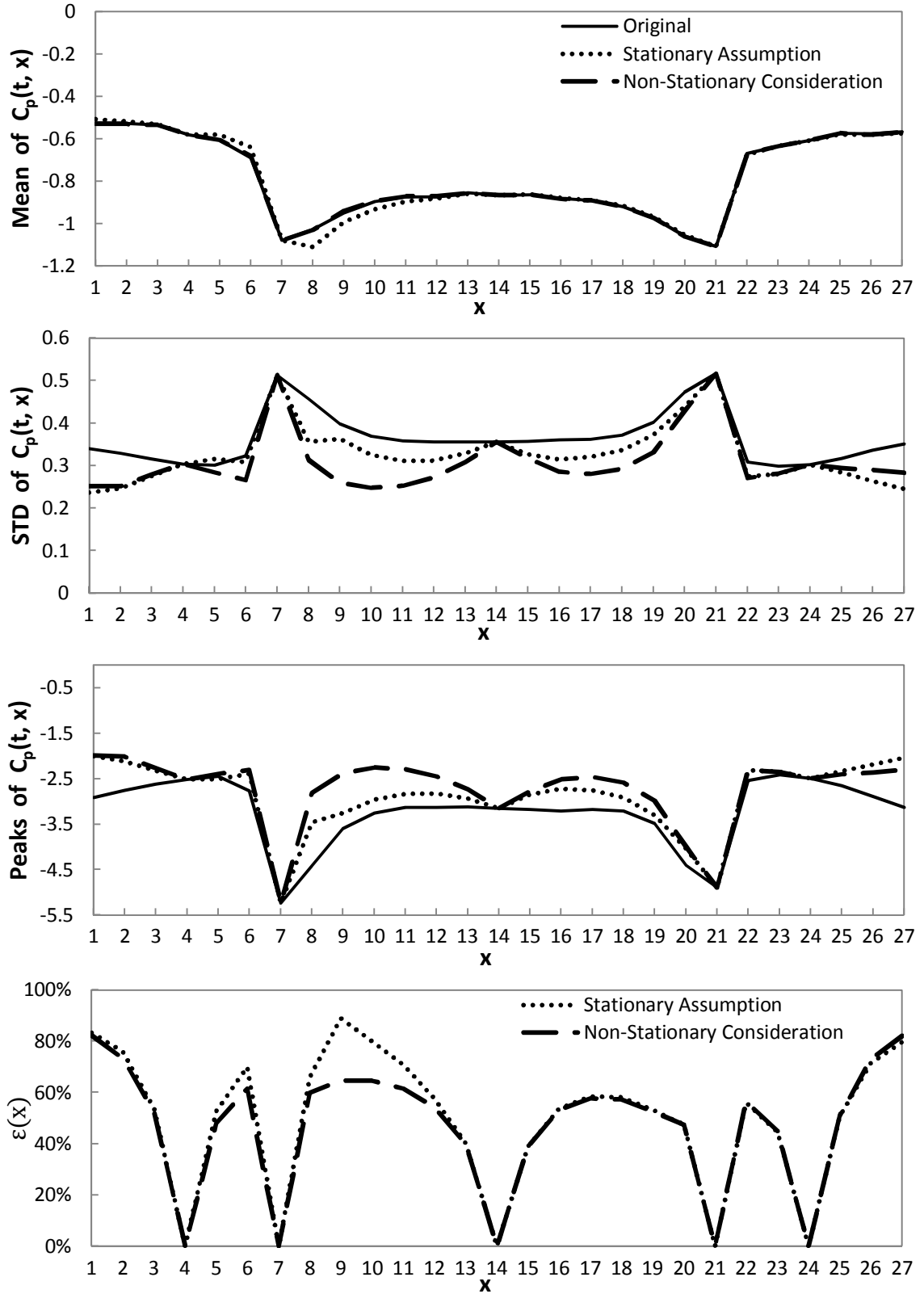
Figure 46: Effects of extrapolation methods on means, standard deviations, estimated peaks and residual errors, 0° wind, 1st row

References

Adrian, R.J. (1977), "On the role of conditional averages in turbulence theory", *Proceedings of the Fourth Biennial Symposium on Turbulence in Liquids*, *J. Zakin and G. Patterson (Eds.)*, 323-332.

Bienkiewicz, B., Ham, H.J. and Sun, Y. (1993), "Proper orthogonal decomposition of roof pressure", *Journal of Wind engineering and Industrial aerodynamics*, 50, 193-202.

Bui-Thanh, T., Damodaran, M. and Willcox, K. (2004), "Aerodynamic data reconstruction and inverse design using proper orthogonal decomposition", *American Institute of Aeronautics and Astronautics*, 42(8) , 1505-1516.

Caracoglia, L. and Jones, N. P. (2005), "Characterization of evolving (local) pressure field on low-rise building", *Proceedings*, *10th Americas Conference on Wind Engineering*, CD-ROM.

Chen, L. and Letchford C.W. (2005), "Proper orthogonal decomposition of two vertical profiles of full scale nonstationary downburst wind speeds", *Journal of Wind engineering and Industrial aerodynamics*, 93, 187-216.

Chen, Y., Kopp, G. A. and Surry, D. (2003), "The use of linear stochastic estimation for the reduction of data in the NIST aerodynamic database", *Wind and Structures*, 6 (2), 107-126.

Cohen, K., Siegel, S. and Mclaughlin (2006), T., "A heuristic approach to effective sensor placement for modeling of a cylinder wake", *Computers & Fluids*, 35, 103-120.

Donoho, D.L., Johnstone, I.M., Kerkyacharian, G. and Picard, D. (1995), "Wavelet shrinkage: asymtopia?", *Journal of the Royal Statistical Society: Series B*, 57 (2), 301-369.

Endo, M. (2011), "Wind tunnel modeling and analysis of wind effects on low rise buildings", Ph. D. Dissertation, Colorado State University.

Everson, R. and Sirovich L. (1995), "The Karhunen-Loeve procedure for gappy data", *Journal of the Optical Society of America*, 12(3), 1657-1664.

Holmes, J. D. (2001), Wind Loading of Structures, *Spon Press*.

Kreyszig, E. (1999), Advanced Engineering Mathematics, *John Wiley & Sons, 8th Edition*.

Lumley, J.L. (1967), "The structure of inhomogeneous turbulent flows", A.Y. Yaglom and V.I Tatarsky (Eds.), *Atmospheric Turbulence and Radio Wave Propagation*, Nauka, Moscow, 166-178.

Melchers, R. E. (1999), Structural Reliability Analysis and Prediction, *John Wiley & Sons, 2nd Edition*.

Misiti, M., Misiti, Y. and Oppenheim, G. and Poggi, J.-M (1996), Wavelet Toolbox for use with MATLAB, *The MathWorks Inc.*.

Nau, R.F., Oliver, R.M. and Pister, K.S. (1982), "Simulating and analyzing artificial nonstationary earthquake ground motions", *Bulletin of Seismological Society of American*, 72 (2), 615-636.

Newland, D.E. (2005), An Introduction to Random Vibrations, Spectral & Wavelet Analysis, 3rd edition, *Dover Publication*, 295-370.

Sirovich, L. (1987), "Turbulence and the dynamics of coherent Structures, Part 1: coherent structures.", *Quarterly of Applied Mathematics*, 45(3), 561–571.

Willcox, K. (2006), "Unsteady flow sensing and estimation via the gappy proper orthogonal decomposition", *Computers & Fluids*, 35, 208-226.

Appendices

A1. POD on Gappy Data (Section 2.4.1)

The pressure fluctuation at a reference location $C_p'(t, x_{\text{ref}})$ can be represented by the POD reconstruction function, using the POD spatial eigenvectors and principal coordinates:

$$C_p'(t, x_{\text{ref}}) = \sum_n a(t,n)\Phi(n, x_{\text{ref}}) \qquad\qquad 1$$

The domain of analysis is confined to time t and pressure coefficients at reference taps x_{ref}. The discrepancy between the original pressures and their approximation (1) is expressed as follows:

$$\varepsilon = (C_p'(t, x_{ref}) - \sum_{n=1}^{i} a(t,n)\Phi(n, x_{ref}))^2 \qquad\qquad 2$$

This error is minimized with respect to the principal coordinates by computing derivatives of (2) with respect to the principal coordinates and setting them to zeros:

$$\frac{\partial \varepsilon}{\partial a(j)} = -2(C_p'(x) - \sum_{n=1}^{i} a(n)\Phi(n,x))\Phi(j,x) = 0 \qquad\qquad 3$$

After rearrangement, (3) can be written as follows:

$$\sum_{n=1}^{i} a(n)\Phi(n,x)\Phi(j,x) = C_p'(x)\Phi(j,x) \qquad\qquad 4$$

If reference taps are limited to three locations, x_1, x_2 and x_3, and the first modal principal coordinate $a(j_1)$ is taken in (3), (4) can be expanded for location x_1:

$$\Phi(j_1,x_1)\Phi(n_1,x_1)a(n_1) + \Phi(j_1,x_1)\Phi(n_2,x_1)a(n_2) + \Phi(j_1,x_1)\Phi(n_3,x_1)a(n_3) = \Phi(j_1,x_1)C_p'(x_1)$$
$$5$$

When locations x_2 and x_3 are considered, the following two equations are obtained, for this case:

$$\Phi(j_1,x_2)\Phi(n_1,x_2)a(n_1)+\Phi(j_1,x_2)\Phi(n_2,x_2)a(n_2)+\Phi(j_1,x_2)\Phi(n_3,x_2)a(n_3)=\Phi(j_1,x_2)C_p'(x_2)$$

6

$$\Phi(j_1,x_3)\Phi(n_1,x_3)a(n_1)+\Phi(j_1,x_3)\Phi(n_2,x_3)a(n_2)+\Phi(j_1,x_3)\Phi(n_3,x_3)a(n_3)=\Phi(j_1,x_3)C_p'(x_3)$$

7

Summation of (7) through (9) leads to the following equation:

$$\{\Phi(j_1,x_1)\Phi(n_1,x_1)+\Phi(j_1,x_2)\Phi(n_1,x_2)+\Phi(j_1,x_3)\Phi(n_1,x_3)\}\,a(n_1)$$

$$+\{\Phi(j_1,x_1)\Phi(n_2,x_1)+\Phi(j_1,x_2)\Phi(n_2,x_2)+\Phi(j_1,x_3)\Phi(n_2,x_3)\}\,a(n_2)$$

$$+\{\Phi(j_1,x_1)\Phi(n_3,x_1)+\Phi(j_1,x_2)\Phi(n_3,x_2)+\Phi(j_1,x_3)\Phi(n_3,x_3)\}\,a(n_3)=$$

$$\Phi(j_1,x_1)C_p'(x_1)+\Phi(j_1,x_2)C_p'(x_2)+\Phi(j_1,x_3)C_p'(x_3)$$

8

It can be expressed in a compact form using matrix notation – the first equation of the matrix equation (9). When a similar operation is repeated for the remaining principal coordinates $a(j_2)$ and $a(j_3)$, two additional equations – the second and the third row of the matrix equation (9) are obtained:

$$\begin{bmatrix}\Phi(i_1,:_{ref})\Phi^T(j_1,:_{ref}) & \Phi(i_1,:_{ref})\Phi^T(j_2,:_{ref}) & \Phi(i_1,:_{ref})\Phi^T(j_3,:_{ref})\\ & \Phi(i_2,:_{ref})\Phi^T(j_2,:_{ref}) & \Phi(i_2,:_{ref})\Phi^T(j_3,:_{ref})\\ sym & & \Phi(i_3,:_{ref})\Phi^T(j_3,:_{ref})\end{bmatrix}\begin{bmatrix}a(j_1)\\a(j_2)\\a(j_3)\end{bmatrix}$$
$$=\begin{bmatrix}\Phi(j_1,:_{ref})C_p'^T(:_{ref})\\\Phi(j_2,:_{ref})C_p'^T(:_{ref})\\\Phi(j_3,:_{ref})C_p'^T(:_{ref})\end{bmatrix}$$

9

Equation (9) can be expressed as follows:

$$[M]\{\hat{a}\}=\{f\}$$

10

where the $(i,\ j)$ elements of matrix $[M]$ and vector $\{f\}$ are, respectively:

$$M(i,j) = \Phi(i,:_{ref})\Phi^T(j,:_{ref}) \tag{11}$$

$$f(i) = \Phi(i,:_{ref})C'^T_p(t,:_{ref}) \tag{12}$$

$$\hat{a}(i) = \hat{a}(t,i) = \text{the } i^{th} \text{ mode reconstructed (POD) principal coordinate} \tag{13}$$

$\Phi^T(i,:_{ref})$ and $C'^T_p(t,:_{ref})$ respectively denote the transpose of ith mode eigenvectors and pressure (at instant t), at all reference taps. It should be noted that $[M]$ is a function only of space and $\{f\}$ is a function of both space and time.

A2. MATLAB Script for Wavelet De-noising (Section 2.6.2)

```
function XD = MEAN_BMS(X, wvnam, J)

% X is the input signal with T data points.

% XD is the time-varying mean.

% wvnam is wavelet name, e.g. 'db4'.

% J is the decomposition level.

% alpha is the parameter for the Birge–Massart strategy.

alpha = 3.0;

T =length(X);

XD=zeros(size(X));

[C, L] = wavedec(X, J, wvnam); % decompose.

[thr, nkeep] = wdcbm(C, L, alpha); % the Birge–Massart strategy for thresholds.

[XD, cxc, lxc, perf0, perfl2] = wdencmp('lvd', C, L, wvnam, J, thr, 's'); % threshold and
reconstruction.
```